Universitetet
i Stavanger

FACULTY OF SCIENCE AND TECHNOLOGY

MASTER'S THESIS

Study program/specialization: Petroleum Engineering/Drilling Engineering	Spring 2017 Open access
Author: Nikka Puspitarini	(signature of author)
Faculty Supervisor: Mesfin Belayneh	
Title of master's thesis: **Uniform Corrosion and Its Effect on Tubing Simulation Study**	
Credits: 30	
Keywords: Corrosion Wear FEM Gas lift Tubing Burst Collapse Von-Mises	Number of pages: 145 + appendices: 23 Stavanger, July 13, 2017

Abstract

The API Barlow and the Tri-axial equations cannot be applied to predict burst pressure in the case of pitting corrosion. The main reason for this is that these models are derived from continuum mechanics, but fracture mechanics is more relevant to pitting corrosion damage. However, up to this level of research, the author was unable to find any analytical documented model used to predict de-rating loading in pitting damage.

The simulation results show that the API models can only be applied in the case of uniform corrosion. In pitting corrosion, a FEM-based model presents a more trustworthy prediction of burst and collapse. Based on the findings of this research, the author believes that FEM modeling is very reliable for any types of damage.

Acknowledgements

I would like to express my heartfelt gratitude and appreciation to my Professor, Mesfin Belayneh for his kind support, help, and excellent academic guidance during the writing of this thesis. He not only steered me in the right direction but also showed me how and encouraged me to survive through the ups and down of life. I could not have imagined having a better mentor for my master's thesis.

I would like to convey my gratefulness to my parents and my little brother for always giving me their endless love and support during this difficult time. My sincere thanks especially to my Father, who gave me the freedom to pursue a master's degree in Norway, leave my comfort zone, and take a risk.

I would like to thank my precious inner circle, Mbekur, Tafia, Audhy, and Destri, for their kindness and friendship, for all the worst times and the very best days we have been through together. Thanks cannot be enough for what you did for me.

I thank my fellow classmates at the University of Stavanger for all the discussion and support and for all the fun we have had in the last two years.

Last but not least, I thank God for giving me such a wonderful chance to study in Norway and experience different cultures, for filling my life with happiness and sadness, and for making me more than who I am.

Table of Contents

List of Figures

List of Tables

Nomenclature

a = Inside radius

b = Outside radius

D = Diameter

E = Young's modulus

Ef = Inhibitor efficiency

fCO_2 = Fugacity of CO2

ID, D_i = Inner Diameter

L = Length

OD, D_o = Outer diameter

Pa, Pi, P = Internal pressure

Pb, Po = External pressure

Pb = Bubble point

pH = Potential of hydrogen

Pi = Initial pressure

Pr = Reservoir pressure

Re = Reynolds number

Ri = corrosion rate of metal with inhibitor

Ro = corrosion rate of metal without inhibitor

r_i, r_a = Inside radius

r_o, r_b = Outside radius

S = Wall shear stress

T = Temperature

t = Nominal wall thickness

U = *Velocity*

x = *Dimensionless parameter*

y = *Dimensionless parameter*

z = *Dimensionless parameter*

β = *Geometry factor*

ρ = *Density*

μ = *Viscosity*

ϑ = *Poisson's ratio*

T = *Torque*

σ_a = *Axial stress*

$\sigma_{b,}\,\sigma_{DL}$ = *Bending stress*

σ_h = *Hoop stress*

σ_{max} = *Maximum stress*

σ_{min} = *Minimum stress*

σ_r = *Radial stress*

$\sigma_r(\Delta T)$ = *Radial stress caused by changed in temperature*

σ_{VME} = *Von-Mises equivalent stress*

σ_y = *Material yield strength*

σ_z = *Total axial stress*

$\sigma_\theta(\Delta T)$ = *Hoop stress caused by changed in temperature*

Abbreviations

API = American Petroleum Institute

DF = Design Factor

DLD = De Waard, Lotz, and Dugstad

DLM = De Waard, Lotz, and Milliams

DLS = Dog Leg Severity

DOF = Degrees of Freedom

EOR = Enhanced Oil Recovery

ESP = Electrical Submersible Pumps

FEM = Finite Element Method

FVF = Formation Volume Factor

GL = Gas Lift

GLD = Gas Lift Design

GOR = Gas Oil Ratio

HCl = Hydrochloric Acid

HF = Hydrofluoric Acid

IPR = Inflow Performance Relationship

IPM = Integrated Production Modeling

MD = Measured Depth

NACE = National Association of Corrosion Engineers

PDE = Partial Differential Equations

PVT = Pressure Fluid Temperature

SCC = Stress Corrosion Cracking

SF = Safety Factor

SRP = Sucker Rod Pumps

TVD = True Vertical Depth

VLP = Vertical Lift Performance

ZRA = Zero Resistance Ammetry

Chapter 1 Introduction

Tubing damage due to corrosion can lead to material deterioration and tubing failures. When tubing is exposed to production and operational loadings, the applied loads must stay within the Von-Mises safe window. This thesis studies the effect of corrosion attack on tubing strength in several cases of different loadings by using tubing design software and the Finite Element Method (FEM) to simulate the stress of the tubing in various loading conditions.

1.1 Background and Research Motivation

In order to reduce the uncontrolled release of formation fluid during the lifetime of a well, NORSOK D-010 describes well integrity solutions based on technical, operational, and organizational issues [1]. The NORSOK standard categorizes well integrity barrier elements as primary and secondary. Tubing (injection/production) is considered to be a primary barrier since it is exposed to high-pressure working fluids during the life cycle of the well. A failure of a well barrier element reduces well integrity, and repair of a failed well barrier increases the cost related to operational and non-productive time. In the worst-case scenario, the well must be abandoned if the repair is not successful.

According to NORSOK D-010's design criteria, tubing/casing shall be of a high quality in order to withstand corrosive environments (H_2S, CO_2, etc.) and shall be designed to carry the realistic load during the lifetime of the well [1]. In addition, the standards also mention that the loads shall be corrected for additional loads and effects such as casing wear, bending, temperature effects, corrosion and plastic formations, and reservoir compaction, as well as several operational loading situations during completion, workover, and kill operation.

Corrosion causes many problems in the oil and gas industry since its effect leads to the failure of materials. Production enhancement activities such as acid and seawater injection cause tubing corrosion due to electrochemical reactions. Corrosion will attack every component of the well and lead to material deterioration. Production tubing is one of the well components that are frequently subjected to corrosion attack. Since its main function is to act as the conduit by which fluids are

transported from the reservoir through surface facilities, it will be exposed to any aqueous phase produced along with the hydrocarbons and some impurities components such as H_2S and CO_2.

The main consequence of this is that it increases operating and maintenance costs substantially. According to a nationwide report in the USA, as shown in Figure 1, corrosion cost in five industrial sectors is predicted to be a total of US$276 billion per year [2]. In the oil and gas production and manufacturing industry, corrosion problems cost US$1.4 billion per year (see Figure 2). In terms of activities, chemical treatment to prevent corrosion accounts for more than 70% of the overall oil production cost.

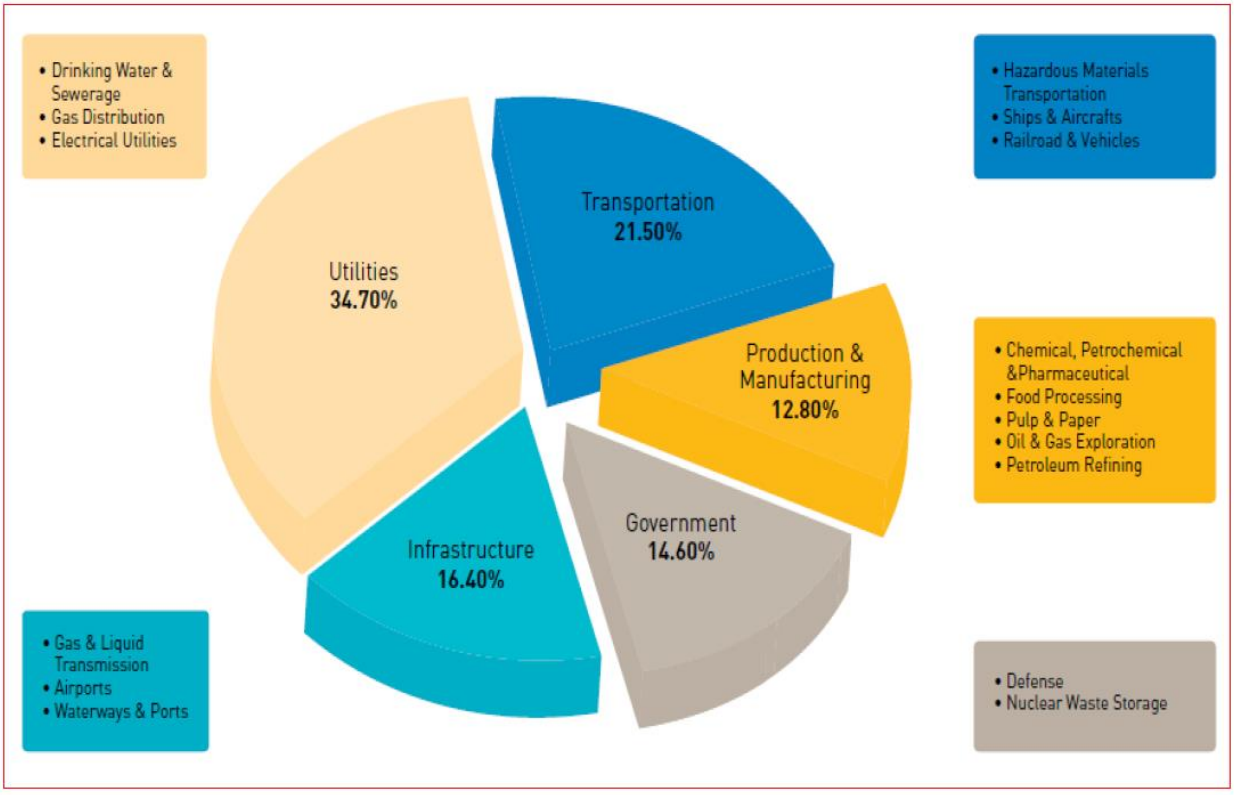

Figure 1: The percentage of total costs due to corrosion in several industries in the USA [2]

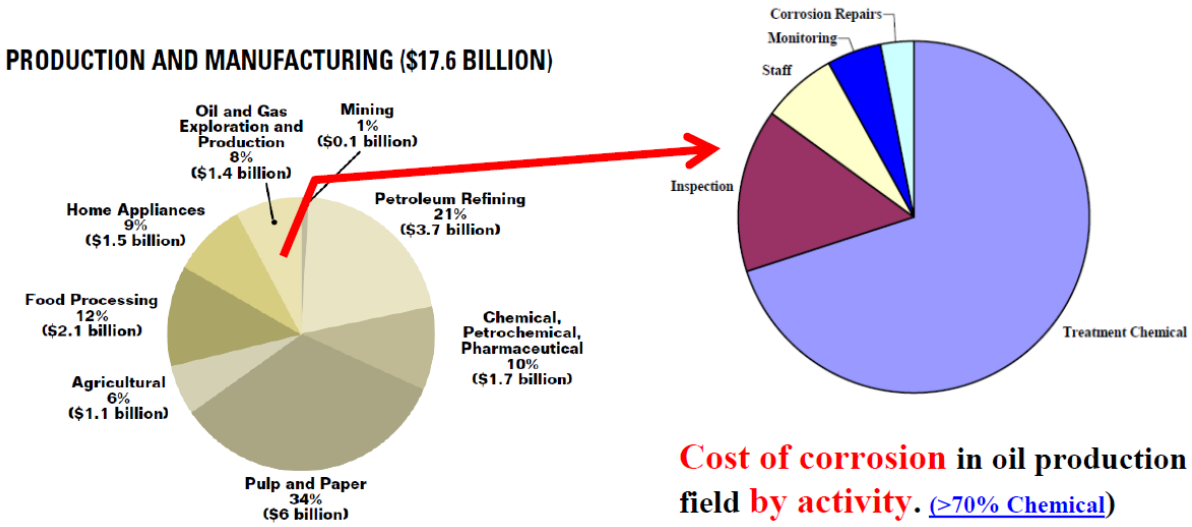

Figure 2: Corrosion cost breakdown in various industrial sectors [3]

In 2006, Vignes and Aadnøy [4] investigated 406 wells at 12 Norwegian offshore facilities operated by 7 companies. They found that 18% (75 wells) had well integrity issues. Figure 3 shows that the most common well integrity problem is due to tubing failure (39%), meaning that the probability of tubing leakage during the life cycle of the well is quite high. Vignes and Aadnøy recommended that the industry exercise an increased focus on tubing design in order to reduce operating cost due to tubing replacement or maintenance. Hence, early detection of tubing leakage before failure and a proper tubing design is important to reduce the risk of damage.

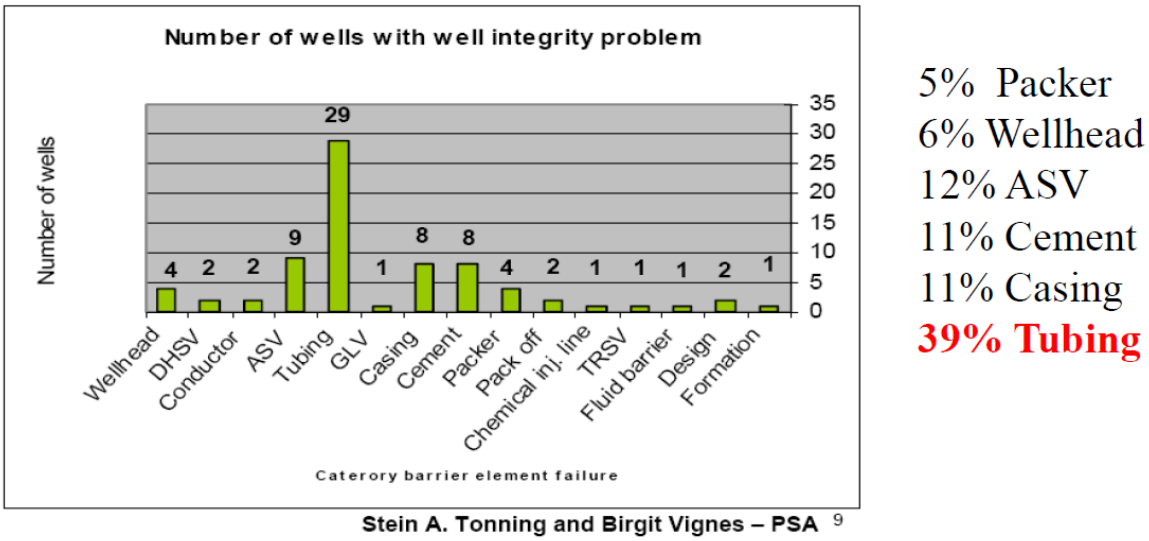

Figure 3: Number of wells with integrity failure, issues, or uncertainty and category of barrier-element failure [4]

The caliper tool data from ConocoPhillips Norway [5] in Figure 4 shows the profile of damage for every joint of tubing in a well. At the depth where the well is at maximum dogleg severity, the tubing damage is the most severe. As shown, the tube wall at the bend section was reduced by 47%. This reduces the load carry capacity of the tubing. The damage itself could be due to several problems such as corrosion attack, mechanical loadings, and well intervention tools that reduce the integrity of the material. This ConocoPhillips case will be used as data in the Finite Element Method (FEM) study where the loadings applied to both inner and outer pipe are taken from the pressure at the depth where the dogleg severity is at maximum.

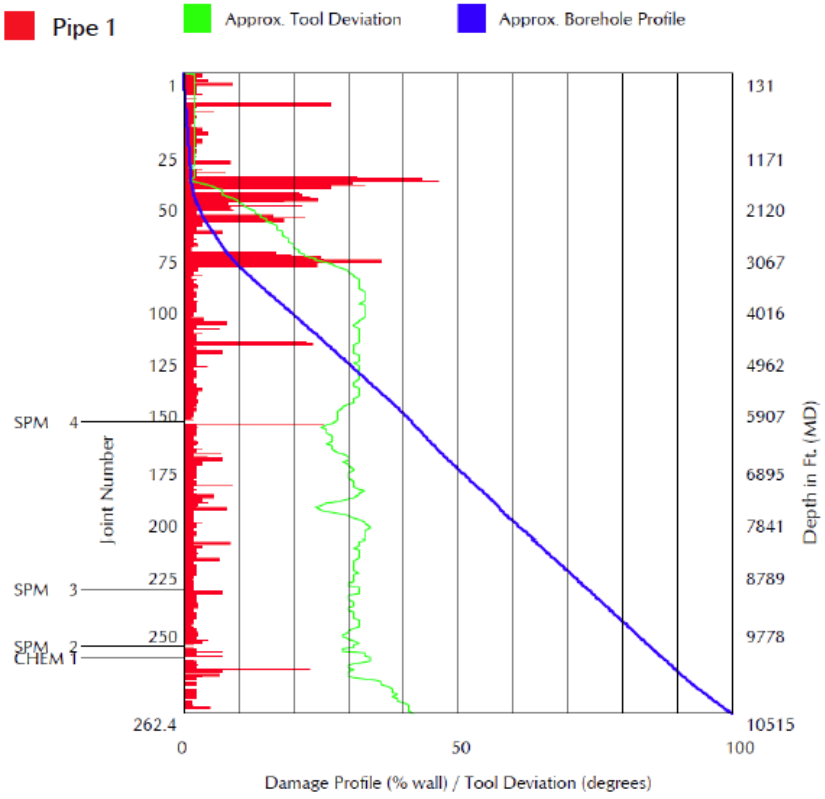

Figure 4: The recorded damage from caliper tools in the deviated hole section [6]

1.2 Problem Statement

During the life of the production period, tubing experiences several dynamic and static loadings such as axial, pressure, or thermal loadings or combinations of these loadings. When corrosion occurs, it initiates premature stress-induced cracking in the tubing. There are many types of corrosion that might occur in the tubing surface. The uniform type of corrosion is the most easily predicted. Uniform reduction of tube size each year weakens the mechanical strength and hence reduces the load carrying capacity of the tube. Experience shows that the service life of the tubing becomes shorter if a suitable tubing maintenance program that includes corrosion prevention is not applied.

The main issues to be addressed in this thesis are:

- What are the CO_2 effects on corrosion rate and how do the empirical models of CO_2 corrosion prediction and its main drivers compare?
- How do the production and well service loadings affect the Von-Mises envelope?
- What is the most sensitive loading that affects Von-Mises stress?
- How does de-rated tubing affect the gas lift design?
- How does uniform corrosion affect the burst and collapse strength of the production tubing?
- How does the analytical model differ from the numerical model in de-rated tubing due to corrosion?
- How does uniform corrosion differ from pitting corrosion in terms of tubing strength in the FEM study?

1.3 Objectives

The primary objectives of this thesis are to study the effect of uniform corrosion on tubing strength (burst and collapse) and to investigate the main parameters for CO_2 corrosion rate. In addition, the secondary objective is to implement tubing integrity simulation workflow for production tubing design when it is expected to be exposed to a corrosive environment.

The main activities are as follows:

- Review the theory of tubing stress, failure criteria, load cases, and FEM.
- Conduct a review of the literature on various corrosion causes and prevention/control methods and review of CO_2 corrosion prediction model.
- Perform simulation studies on CO_2 corrosion rate prediction using NORSOK M-506 and other reviewed models.
- Perform production tubing design simulation for different wear depth using WELLCAT software and develop gas lift design using PROSPER software as one of the loading scenarios in tubing simulation.
- Develop FEM-based numerical modeling of different tubing wear depth and simulation study of various loading scenarios using Abaqus CAE software and compare the result with the theoretical and API models.

- Develop FEM-based burst and collapse models as a function of wear depth.

1.4 Research Methods

This thesis research studies the effect of uniform corrosion on tubing strength mainly by simulating tubing using a Finite Element Method (FEM) numerical model and comparing it with analytical and API models. These models will predict the tubing strength such as burst and collapse rating when the damage occurs due to uniform corrosion attack. One corrosion case due to CO_2 will be discussed in further detail, and a tubing model will also be developed using tubing design software to simulate Von-Mises stress when several productions and well service loadings are applied. Pitting corrosion simulation will also be discussed shortly to compare the stress distribution with the uniform corrosion case. By simulating this condition, the strength of the tubing will be predicted to define the maximum pressure it can withstand after being damaged. Figure 5 shows the research methods applied in this thesis.

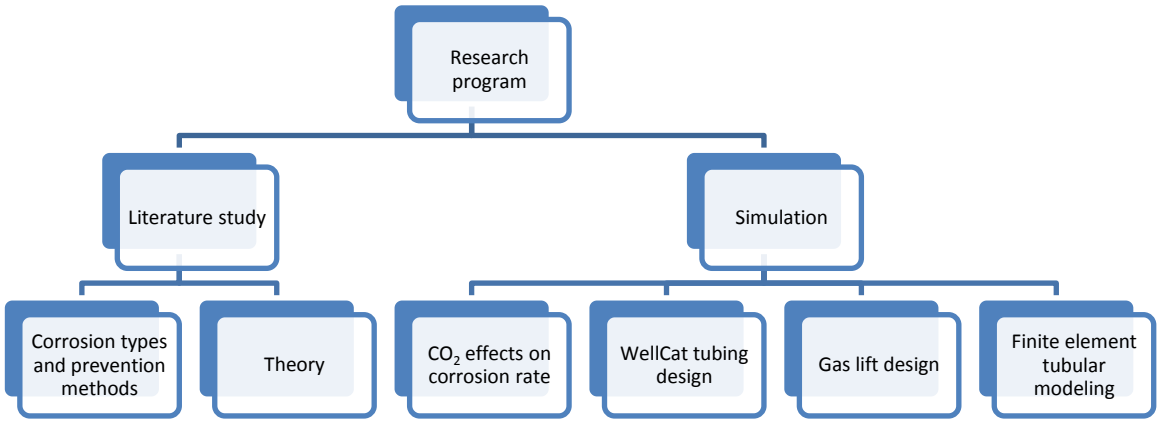

Figure 5: Research methods

Chapter 2 Theory

This section presents the theory of tube stress and failure criteria used in this thesis [7]. The basic concepts of the Finite Element Method will also be summarized.

2.1 Tubing Stress

In the life cycle of a well, the tubing will be subjected to many production and well service loadings. It is important to estimate the tubing strength in order to have safe operations without causing tubing failures since well integrity surveys indicate frequent integrity problems (about 39% failure) in the tubing. The aim of a tubing stress and failure analysis study is to determine the tubing strength in the cases of:

1. Burst
2. Collapse
3. Tensile/axial failure
4. Compression/buckling failure

2.1.1 Types of Cylinders

Stress in the tubing can be determined based on the type of cylinder. These are categorized as:

1. Thin-walled cylinder, where t < $\frac{1}{10} \times r$
2. Thick-walled cylinder, where t > $\frac{1}{10} \times r$

where

t = thickness of the cylinder wall

r = inner radius of the cylinder

2.1.2 Thin-Walled Cylinder

When a cylinder is loaded internally with a pressure (P) as shown in Figure 6, three kinds of stresses will be developed: axial stress, hoop or tangential stress, and radial stress.

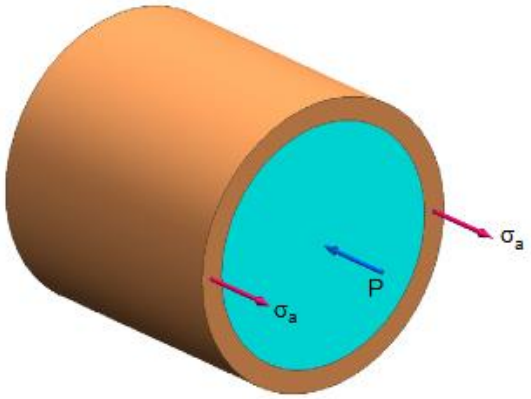

Figure 6: Axial stress in thin-walled cylinder [8]

Axial Stress (σ_a)

Axial stress must be considered in terms of two conditions related in a thin-walled cylinder: closed ends and open ends. For closed ends, the applied pressure and axial stress in the wall will reach equilibrium in similar ways. The equilibrium forces are given by [7]:

$$P\pi r^2 = \sigma_a \mu D t \tag{2.1}$$

$$\sigma_a = \frac{Pr}{2t} \tag{2.2}$$

For open ends:

$$\sigma_a = 0 \tag{2.3}$$

Radial Stress (σ_r)

The radial stress for thin-walled cylinders varies from - P at the inner surface to 0 at the outer surface.

At the inner surface:

$$\sigma_r = -P \tag{2.4}$$

At the outer surface:

$$\sigma_r = 0 \tag{2.5}$$

Hoop Stress (σ_θ)

When the cylinder is sectioned, it has the length of L and diameter of D as seen in Figure 7. After internal forces (P) are applied, the system will reach equilibrium. The hoop stress is given by [7]:

$$PLD = 2\sigma_\theta Lt \tag{2.6}$$

$$\sigma_\theta = \frac{Pr}{t} \tag{2.7}$$

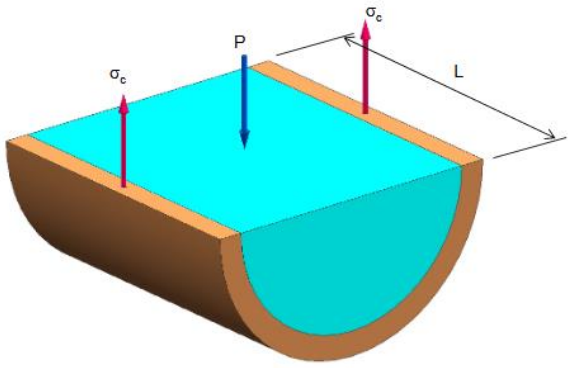

Figure 7: Hoop stress in thin-walled cylinder [8]

2.1.3 Thick-Walled Cylinder

When a thick-walled cylinder having an inner radius = a and an outer radius = b is subjected to internal pressure Pi and external pressure Po, stresses are generated across the thickness of the

cylinder in the axial, tangential, and radial directions as shown in Figure 8. The solution of the stresses was solved by Lame and consists of four parts:

1. Equilibrium equation
2. Compatibility relations
3. Hooke's law
4. Boundary condition

The derivation of the solution is not covered in this section; only the results are presented.

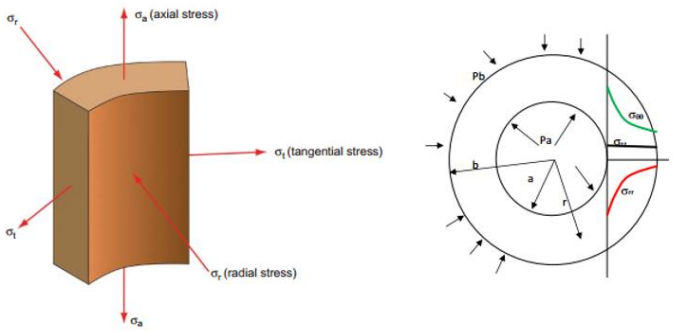

Figure 8: Stresses in thick-walled cylinder [9]

Axial Stress (σ_a)

For open ends:

$$\sigma_a = 0 \tag{2.8}$$

For closed ends:

$$\sigma_a = \frac{a^2 P_a - b^2 P_b}{b^2 - a^2} \tag{2.9}$$

For both ends closed:

$$\sigma_a = 2\vartheta \frac{a^2 P_a - b^2 P_b}{b^2 - a^2} \tag{2.10}$$

where ϑ is Poisson's ratio

Hoop Stress (σ_θ)

$$\sigma_\theta = \frac{a^2 P_a - b^2 P_b}{b^2 - a^2} + \frac{a^2 b^2}{(b^2 - a^2) r^2}(P_a - P_b) + \sigma_\theta(\Delta T) \tag{2.11}$$

Radial Stress (δ_r)

$$\sigma_r = \frac{a^2 P_a - b^2 P_b}{b^2 - a^2} + \frac{a^2 b^2}{(b^2 - a^2) r^2}(P_a - P_b) + \sigma_r(\Delta T) \tag{2.12}$$

where

$\sigma_r(\Delta T)$ and $\sigma_\theta(\Delta T)$ are radial and hoop stresses caused by change in temperature

2.2 Failure Criteria and Design Limit

2.2.1 Failure Criteria

Failure criteria for yielding can be categorized into [7]:

1. Tresca failure criteria (Maximum shear theory)

   This failure criterion only considers maximum and minimum principal stresses and neglects intermediate principal stress. Tresca failure represents a critical value of the maximum shear stress in the isotropic material with the yield stress (σ_y):

   $$\sigma_y = \sigma_{max} - \sigma_{min} \tag{2.13}$$

2. Von-Mises failure criteria (Maximum distortion theory)

   Von-Mises represents a critical value of distortion energy stored in the isotropic material and also takes into account intermediate principal stress. In this case, yield stress is based on the combination of three principal stresses (σ_a, σ_r, σ_θ) and the shear stress caused by torque (τ) and is given by:

$$\sigma_{VME} = \sqrt{\frac{1}{2}\{(\sigma_\theta - \sigma_r)^2 + (\sigma_r - \sigma_a)^2 + (\sigma_a - \sigma_\theta)^2\} + 3\tau^2} \tag{2.14}$$

3. Maximum principal stress theory

   This criterion only considers the maximum principal stress:

$$\sigma_y = \sigma_{max} \tag{2.15}$$

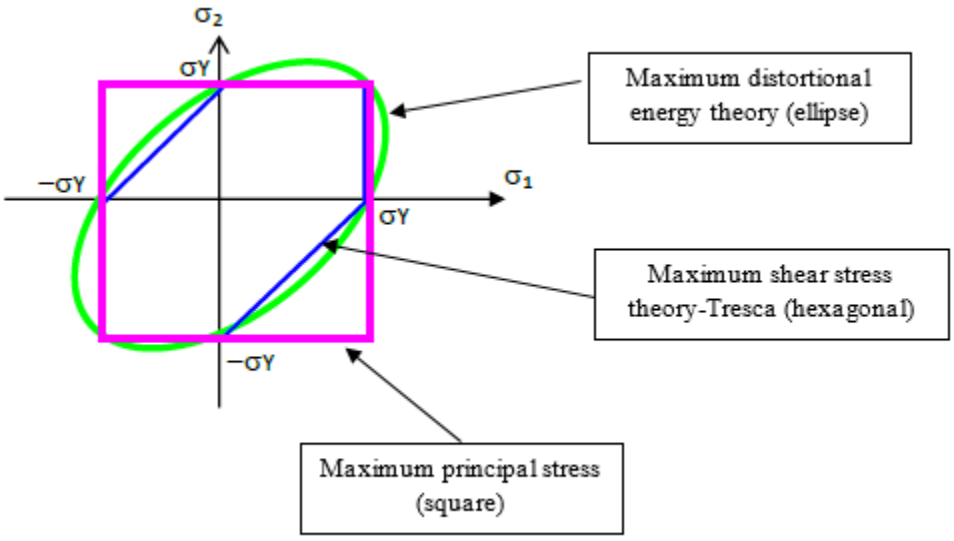

Figure 9: Comparison of three failures criteria [7]

2.2.2 Design Limits

The application of design factor (DF) in tubing design becomes important since it addresses the uncertainties in the manufacturing process that influence the strength of the tubing. In the real world, tubing is often subjected to various loadings such as Tri-axial loads consisting of burst, collapse, and axial failure modes (tension and compression). The Tri-axial design factor is defined as the minimum ratio between yield strength and Von-Mises stress as given by [9]:

$$DF = \frac{\sigma_y}{\sigma_{VME}} \tag{2.16}$$

The Von-Mises limit line represents the condition where tubing begins to yield as shown by the red line in Figure 10. The plotted service loads shown by the blue line illustrate the combined stress over the entire tubing.

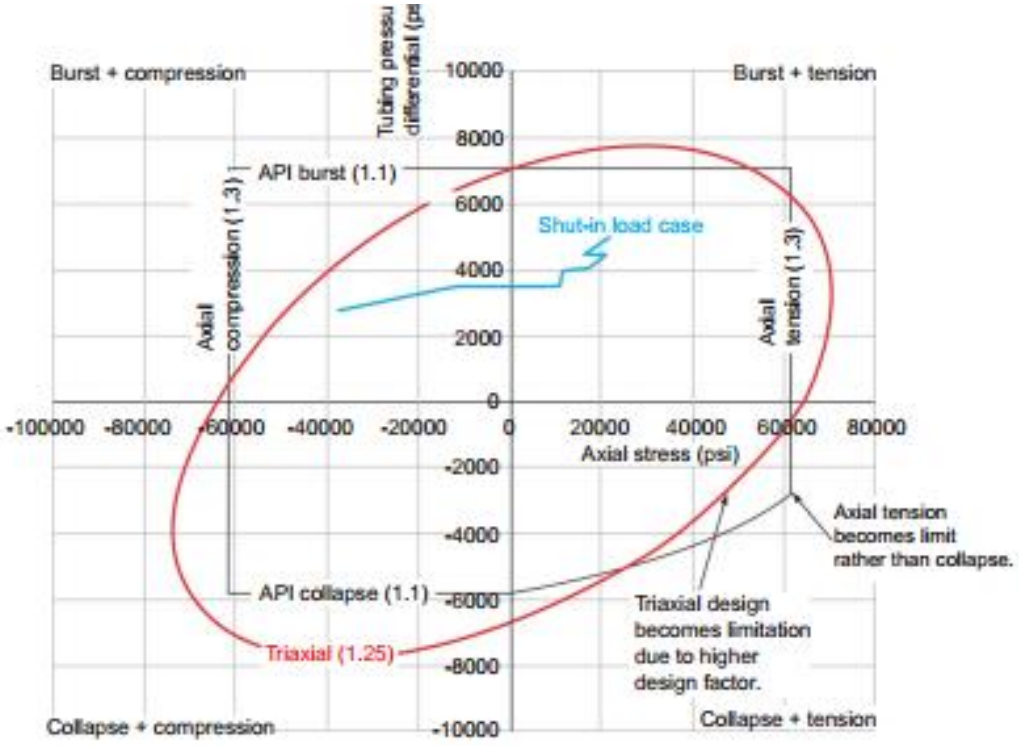

Figure 10: Design limit plot with design factors - L80 material [9]

The safety factor (SF) is given by [9]:

$$SF = \frac{1}{[x^2 - xy + x^2]^{0.5}} = \frac{\sigma_y}{\sigma_{VME}} \tag{2.17}$$

where

$$x = \frac{P_i + \sigma_a}{\sigma_y} \tag{2.18}$$

$$y = \frac{(P_i + P_o)}{\sigma_y} \tag{2.19}$$

2.3 Burst Theory and Equations

Aadnoy [10] stated that "burst is a tensile failure, resulting in rupture along the axis of the pipe" as shown in Figure 11. In the life cycle of a well, the tubing will be exposed to some burst pressure loadings such as pumping operations, production operations, well service, and so on.

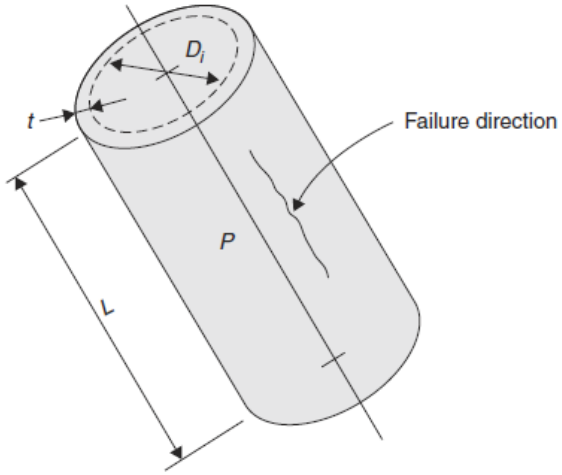

Figure 11: Burst failure [10]

When the thin-walled and closed-ends vessel in Figure 11 is subjected to internal pressure (P), the axial and hoop stresses will be developed as shown in Figure 12.

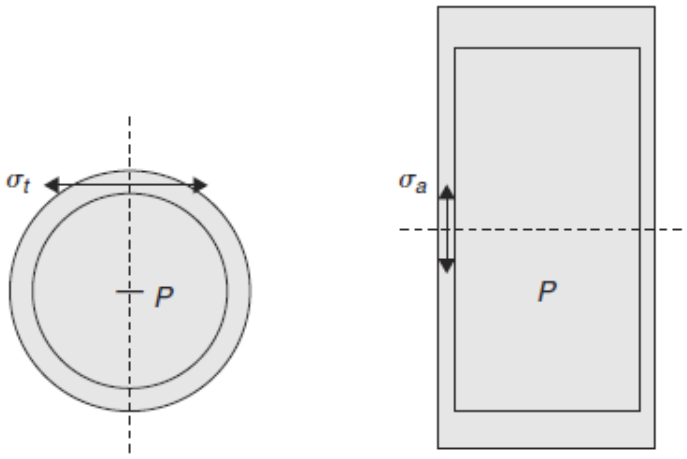

Figure 12: Stresses developed in thin-walled cylinder pressured from the inside [10]

Since the burst is a condition in which the hoop stress exceeds the tensile strength, the simple definition of burst formula is [9]:

$$P_{burst} = 2\sigma_{tensile}(\frac{t}{D_i}) \tag{2.20}$$

Or, if we use the outer diameter:

$$P_{burst} = 2\sigma_{tensile}(\frac{t}{D_o}) \tag{2.21}$$

2.3.1 Barlow Burst Pressure

Based on the API Bulletin 5C3 (1994) [11], the burst rating can be determined using Barlow formula, as stated in equation 2.22 with the safety factor included:

$$P_b = Tolerance \times \frac{2\sigma_y t}{D} \tag{2.22}$$

where

σ_y is the minimum yield strength (psi)

t is the tubing nominal thickness (inch)

D is the pipe outer diameter (inch)

Tolerance is the wall thickness tolerance correction (fraction), which is set at 0.875 allowable wear and tear.

2.3.2 Burst Pressure Based on Tri-axial Design Equation

The solution for internal pressure (Pi) is given by [10]:

$$P_i = \frac{\beta\sigma_a - 2\sigma_a + 2\beta^2 P_o - \beta P_o \pm \sqrt{-3\beta^2{\sigma_a}^2 - 6\beta^2\sigma_a P_o - 3\beta^2{P_o}^2 + 4(\beta^2 - \beta + 1){\sigma_y}^2}}{2(\beta^2 - \beta + 1)} \quad (2.23)$$

where

$$\beta = \frac{2{d_o}^2}{{d_o}^2 - {d_i}^2} \quad or \quad \beta \approx \frac{{d_o}^2}{2t\,(d_o - t)} \quad (2.24)$$

2.4 Collapse Theory and Equations

Collapse is a failure mode when the external pressure acting on the tubing exceeds the internal pressure. It is a geometric failure rather than a materials failure. Aadnoy [10] stated that collapse is a stability problem. Even a slight imperfection in loadings or circularity will lead to deformation, shape change, and eventual instability.

2.4.1 Collapse Pressure Based on API 5C3 Equation

Based on API Bulletin 5C3 (1994), the determination of collapse strength depends on the ratio of D/t (slenderness ratio) and is categorized into four types [11]:

1. Yield strength collapse pressure
2. Plastic collapse
3. Transition collapse
4. Elastic collapse

The four collapse limits for L-80 grade tubing are illustrated in Figure 13.

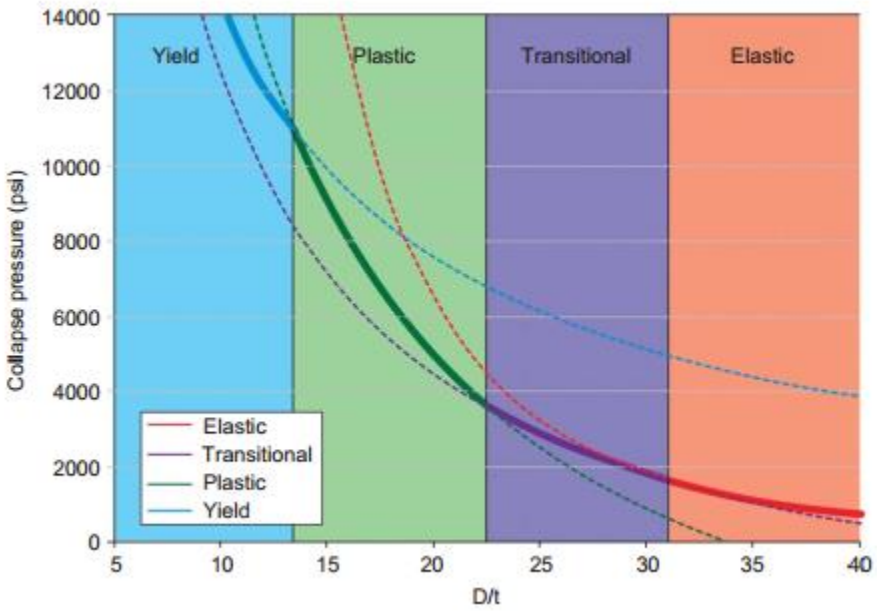

Figure 13: Collapse pressure as a function of slenderness [9]

The collapse models for various grading tubular (casing/tubing) are listed in Table A2. The four collapse ranges for tubing T-95 used in this study are provided in Table 1.

Table 1: T-95 collapse models [9]

Grade (ksi)	Elastic Collapse (D/t)	Transitional Collapse (D/t)	Plastic Collapse (D/t)	Yield Collapse (D/t)
80	> 31.02	22.47 - 31.02	13.38 - 22.47	< 13.38
95	> 28.36	21.33 - 28.36	12.85 - 21.33	< 12.85

Yield Strength Collapse Formula

Bellarby [9] stated that the yield strength collapse formula is the external pressure that generates a stress equivalent to the minimum yield stress on the inside wall of the tubing, given by:

$$P_c = 2\delta_y \left[\frac{\left(\frac{D}{t}\right) - 1}{\left(\frac{D}{t}\right)^2} \right] \tag{2.25}$$

where

P_c is the minimum collapse pressure (psi)

D is the nominal outside diameter (in)

t is the nominal wall thickness (in)

σ_y is the minimum yield strength of the material (psi)

Plastic Collapse Pressure

The collapse limits for plastic collapse region are given by [9]:

$$P_c = \left[\frac{A}{D/t} - B\right] - C \tag{2.26}$$

Table 2 displays the constants A, B, and C for T-95 tubing, which is analyzed in this thesis. For other tubing, the constants are provided in Table A4.

Table 2: Plastic collapse factors [9]

Grade (ksi)	A	B	C
95	3.124	0.0743	2404

Transitional Collapse Pressure

The collapse limits for transition collapse region are given by [9]:

$$P_c = \left[\frac{F}{D/t} - G\right] \tag{2.27}$$

Table 3 shows the constants F and G for T-95 tubing and for other tubulars, the constants are provided in Table A5.

Table 3: Transitional collapse factors [9]

Grade (ksi)	F	G
95	2.029	0.0482

Elastic Collapse Pressure

The collapse limits in the elastic collapse pressure are given by [9]:

$$P_E = \frac{46.95 \times 10^6}{(D/t)[(D/t) - 1]^2} \tag{2.28}$$

Safety Factor (SF)

The safety factor for collapse is determined by:

$$Collapse\ SF = \frac{P_C}{P_E} \tag{2.29}$$

where

$$P_E = P_O \left[1 - \frac{(d_o - d_i)}{d_o}\right] P_i \tag{2.30}$$

Pc is the collapse pressure calculated from the API equation.

2.4.2 Collapse Pressure Based on Tri-axial Design Equation

The solution for external pressure (Po) is given as [10]:

$$P_o = \frac{-\sigma_a + 2\beta P_i - P_i \pm \sqrt{-3{\sigma_a}^2 - 6\sigma_a P_i - 3{P_i}^2 + 4{\sigma_y}^2}}{2\beta} \tag{2.31}$$

When bending stress is considered, the axial stress in equation 2.31 is replaced by:

$$\sigma_{a\,max} = \sigma_a + \sigma_{DL} \tag{2.32}$$

2.5 Load Cases

When the tubing is designed, it must be able to withstand the loads that it may experience. To have a good design, the design load should incorporate all the possible cases and parameters to ensure that they represent the worst cases. The discussion on this subject is taken from Bellarby [9].

1. Initial conditions (base case)

   One needs to establish the base case since the other loads will be calculated relative to this. The input data such as pressures and temperatures should be corrected because if they are set incorrectly, the other cases will also be incorrect.

2. Tubing pressure tests

   Since the tubing forms one of the well barriers, it is necessary to ensure before use that it can withstand the service loads to prevent tubing failures. This service load could be a shut-in case or an injection case. Many companies use the standard operating procedure that the tubing pressure test should be 10% greater than the maximum tubing pressure differential during service loads.

3. Annulus pressure tests

   The main purpose of annulus pressure tests is to ensure that packers or tubing hangers will be capable of serving their function. Ideally, the test should use the same criteria as the tubing test to withstand the tubing leaking scenario. The back-up pressure is normally used to estimate the collapse loads since there is no requirement to do the collapse test.

4. Production

   When the well is being produced, it will be exposed to thermal changes and generate high-temperature loads. Hence, it is important to predict potential temperature changes, which are highly dependent on the fluids involved.

5. Gas-lifted production

   The injected gas through the annulus can develop thermal changes in the tubing (either cooling or heating effects). When the gas lift is at low pressure, it will act as an insulator maintaining tubing temperatures. It can also generate loads due to the bleeding-off of gas and cause high burst load on the tubing and high collapse loads on the production casing.

6. Shut in

A long-term shut in case can develop high pressure and temperature in the well that will produce a critical load. When the well is at high-temperature and steady-state production followed by a quick shut in, it can develop high pressure and temperature, but a normal long-term shut in will cool down the well and the temperature gradient will go back to the geothermal gradient.

7. Injection

   The fluids used for injection such as sea water or water from a river or lake are usually cold and injected at high pressure. These combinations will develop a high tensile load in the tubing that will cause tubing failures if it exceeds the tensile strength. In the gas injection case, injected gas can be hot or cold and since gas has light density, higher pressure is needed to inject it. These combinations also cause severe loads.

8. Stimulation

   In wells with a large amount of scaling, stimulation such as acid stimulation, matrix stimulation, hydraulic fracturing, acid fracturing, and so forth is needed to optimize production. The stimulation jobs will increase the loads, so a test string is needed before stimulation to ensure that the tubing can withstand the possible loads.

2.6 The Finite Element Method (FEM)

In this thesis, the tubing damage caused by mechanical and electrochemical means will be modeled and simulated using FEM via Abaqus CAE software. This section presents background about FEM.

The Finite Element Method (FEM) is a numerical method that provides an analytical model to obtain an approximate solution to engineering problems. The concept used in FEM is to divide the mathematical model into a number of simpler subdomains called *finite elements* or *elements*. In short, this method separates a structure into several elements, then reconnects them at "nodes" that hold elements together and formulates the problems in a system of algebraic equations. FEM has been recognized as a general method that can be applied in a wide variety of mathematical and engineering problems such as solid mechanics, deformations, elasticity, heat transfer problems, fluid flow, and so on. It can also handle very complex geometry, restraints, and loading (thermal, pressure, inertial forces, gravity, etc.). The workflow of FEM is shown in Figure 14 and Figure 15.

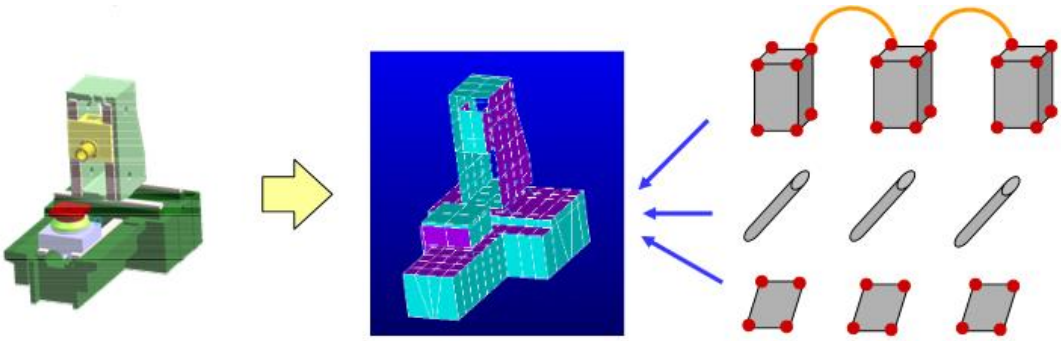

Figure 14 Finite element: Small pieces of structure [12]

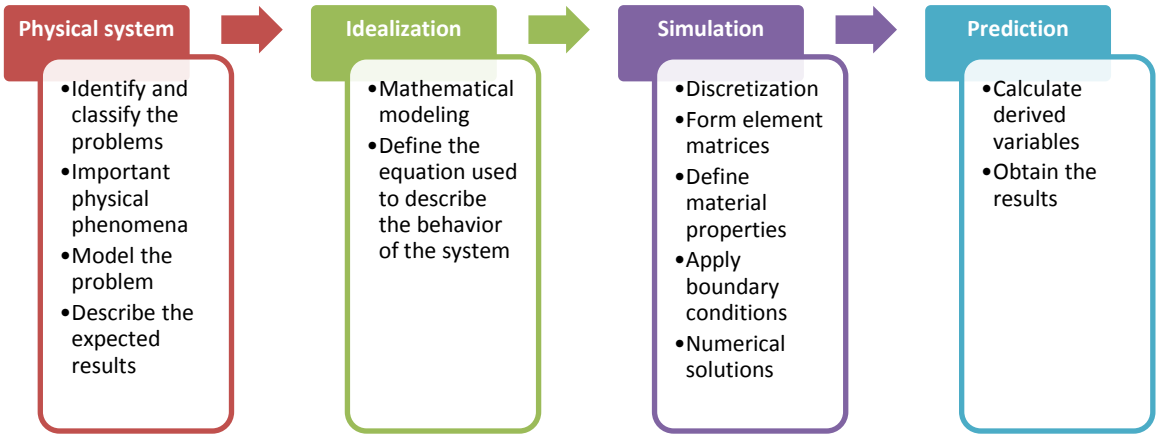

Figure 15: Workflow of FEM study

2.6.1 Idealization

Idealization is a process to build a mathematical model from a physical system [13]. The mathematical model provides an abstraction of the physical reality, manages the complexity, and helps the user to understand the behavior of the system by producing an analytical model or numerical calculation.

The numerical analysis can be approached by using *explicit* and *implicit modeling* to obtain the approximations to the solutions. In explicit modeling, the user builds the model from scratch by

selecting a mathematical model of the physical problem and implementing a finite element program in the model or writing the program themselves. In implicit modeling, specific elements are chosen from the catalog and the user will automatically accept the mathematical models set the elements.

2.6.2 Discretization and Error Sources

Discretization or subdivision of the domain is a process used to convert continuous equations and functions into discrete counterparts that can be used to calculate numerical solutions. Physical systems are usually described in terms of partial differential equations (PDE). In many engineering problems which have high complexity, PDE cannot be solved with analytical methods. Hence, numerical models are needed to obtain the approximation of the solutions by using discretization methods [14]. In this step, the domain is divided into elements that are connected at nodes. At every node, the properties of the domain are defined. This step might be the most important one in FEM since the method of element discretization will affect the accuracy of the numerical results and the computational time. One of the advantages of FEM is the privilege to choose the type of discretization used in both the elements and the functions. Figure 16 shows the discretization process in a domain.

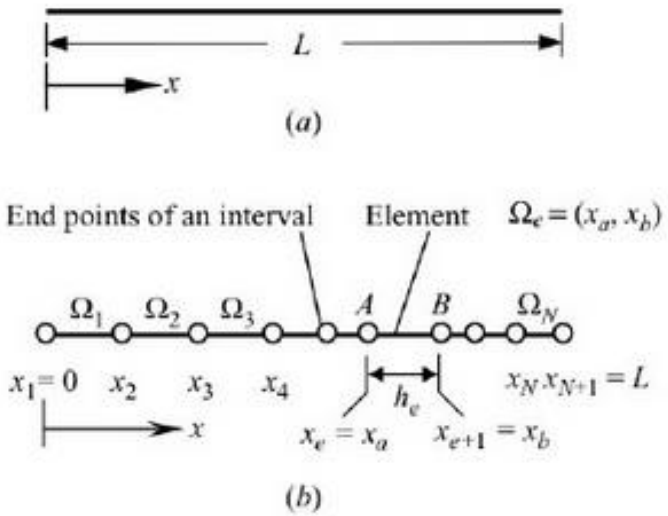

Figure 16 Discretization process in a domain [15]

According to Cook [16], discretization will introduce two types of error: *modeling error* and *discretization error*. Modeling error can be reduced by improving the model, while discretization

error can be minimized by using more elements. When the computer performs the numerical calculation, it also introduces *numerical error* caused by the use of numbers of finite precision [16]. In short, the accuracy of the numerical result depends on the number of subdomains and the function of the subdomains.

2.6.3 Element Attributes

The elements used in FEM are isolated from each other and are considered as individual entities by which material properties are defined. The element geometry can be modeled in one dimension (straight liner or curved segments), two dimensions (quadrilateral or triangular shape), or three dimensions (tetrahedral, hexagonal, wedges).

2.6.4 Nodes

A set of points called *nodes* is also introduced in each element. The function of nodes is to describe the element geometry and the place for the degree of freedom (DOF). The combination of elements and nodes will specify a *finite element mesh* and will define the discretization of a domain.

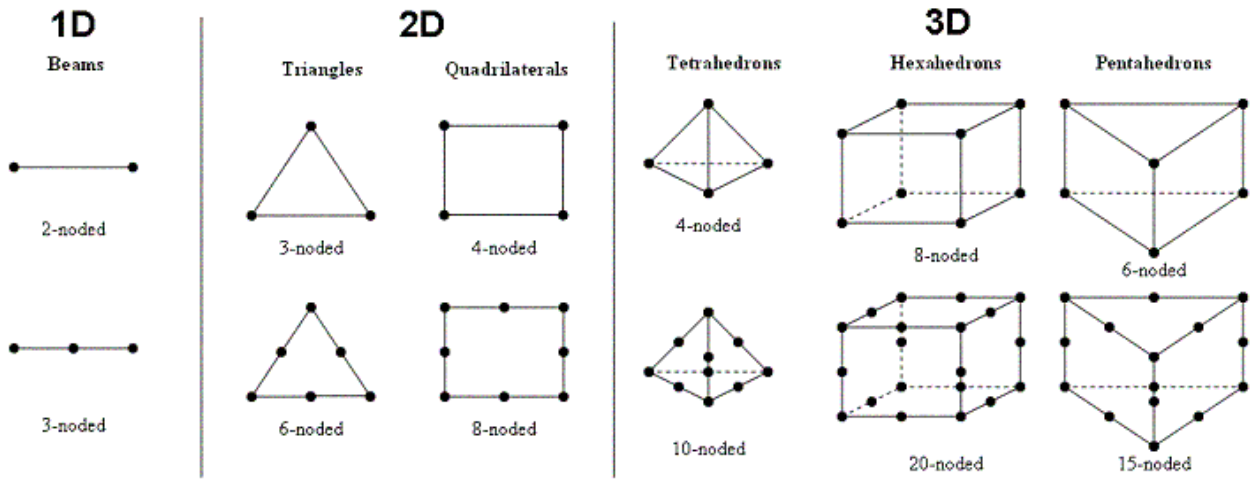

Figure 17 Sample of simple element shapes and standard node placement [17]

2.6.5 Degree of Freedom (DOF)

In general, the degree of freedom is the number of values that are free to vary in the equation system that is being solved. In FEM, DOF defines the *state* of the element and also serves to

determine how different element types can be connected. For example, in solid mechanics modeling, DOF specifies the type of loads that can be transmitted through the nodes.

2.6.6 Boundary Conditions

The boundary condition is commonly defined as the application of the constraints. It needs to be defined before solving the finite element equations.

Chapter 3 Literature Study

This section presents basic corrosion theory, types, effects, and prevention methods. The corrosion cases that occur in oil field equipment will be discussed. Some CO_2 corrosion prediction models and the main corrosion parameters are summarized.

3.1 Effect and Consequences of Corrosion

Corrosion gives rise to many problems in the oil and gas industry and causes mechanical damage, economic loss, and safety issues. It is important to have a good understanding of its mechanism and various types so that appropriate preventions can be applied in order to prevent or minimize the impacts of corrosion. During the design stage, the selection of appropriate material for casing, tubing, flowline, and other parts is important, particularly for high-cost activities so that future losses of the metal can be diminished. According to NORSOK D-010 criteria, the material should be of high quality that will enable it to resist a corrosive environment and carry operational loads [1].

Some of the major corrosion consequences can be outlined as follows:

1. The deterioration of metal and its properties will attack every component throughout the life cycle of the well and lead to reduced mechanical strength.
2. Time will be lost due to maintenance of corroded equipment, which leads to higher operating costs.
3. Corroded equipment can affect public health and safety (e.g., structural failures due to corrosion is a hazard).

3.2 Basic Corrosion Theory

Corrosion is degradation of the material due to reactions with the surrounding environment and it often produces new compounds. It is an electrochemical process composed of two half-cell reactions involving electrical currents which require four fundamental components:

1. An anode
2. A cathode
3. A conducting electrolyte for ionic movement

4. An electrical current

The corrosion cell:

a. Anodic Reactions

In anodic reactions, the oxidation process occurs and the electrons are released from the anode's surface [2].

$$Fe \rightarrow Fe^{2+} + 2e^{-}$$

Fe = metallic iron

Fe^{2+} = ferrous ion which carries a double negative charge

e^{-} = electrons which remain in the metal

b. Cathodic Reactions

The electrons produced at the anodic surface will be consumed at the cathodic surface. Reduction is the type of chemical reactions when it consumes electrons.

$$R + e^{-} \rightarrow R^{-}$$

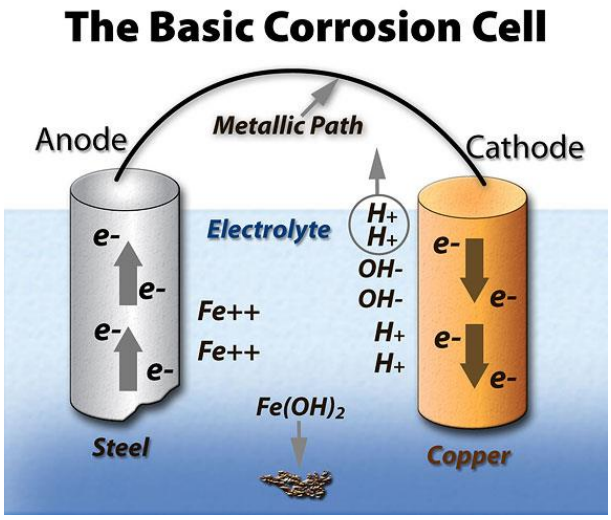

Figure 18 Corrosion cell [18]

3.3 Corrosion Prevention Methods

3.3.1 Cathodic Protection

Cathodic protection is a commonly applied corrosion prevention method. The basic concept of this method is to protect the metal surface by converting it into the cathode of a corrosion cell. Cathodic protection is categorized as follows [2]:

a. Sacrificial anode

Sacrificial anode inhibits corrosion by transforming anodic sites (active) to cathodic sites (passive) and supplying electrical current or free electrons from an alternate source. The sacrificial anodes used are a metal that is less noble than steel (magnesium, aluminum, etc.), usually connected by the wire to the system to be protected. See Figure 19.

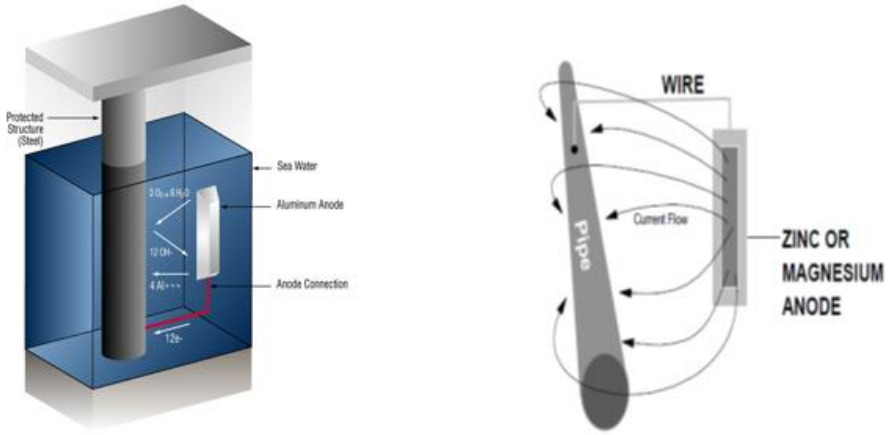

Figure 19: Sacrificial anode [19]

b. Impressed Current Cathodic Protection (ICCP)

This method needs direct current (DC) electricity from an external source that is connected to the impressed-current anode sites. The ICCP system can use platinum, graphite, high-silicon cast iron, or lead-silver alloy. Figure 20 shows this system.

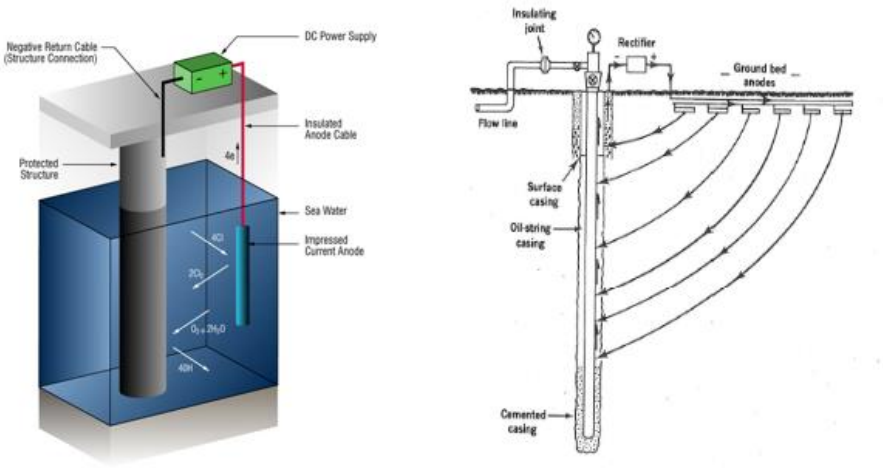

Figure 20: Impressed Current Cathodic Protection (ICCP) [19]

3.3.2 Chemical Inhibitors

A corrosion inhibitor is a chemical substance that, when added to the environment in low concentration, protects the metal surface exposed to that environment. The inhibitor typically works by adsorbing molecules on the metal surface and creating a protective film. Inhibitors are generally classified into two groups [2]:

a. Organic corrosion inhibitors

Organic inhibitors typically act as cathodic, anodic, or together as cathodic and anodic inhibitors and form a hydrophobic film on the metal surface. These inhibitors are the most widely used in the oil and gas industry. Organic inhibitors placed in the medium surrounding the metal must be soluble. Some examples of these inhibitors are urea, heterocyclic nitrogen compounds, succinic acid, amines, and benzoates.

b. Inorganic corrosion inhibitors

Inorganic inhibitors manage corrosion by forming a barrier between the electrolyte and the material surface and applying ion scavenging and cathodic passivation to protect the material. Some examples of these inhibitors are calcium phosphate, zinc phosphate, and calcium borosilicate. This type of inhibitors has a limited use since they must be applied in constant concentrations and are often pH-sensitive.

3.3.3 Protective Coatings

Protective coatings are used to protect metal surfaces against corrosion attack. They work by reducing the cathodic area available for corrosion reaction. They are summarized as follows [2]:

a. Metallic coatings

Metallic coatings provide a protective layer that inhibits corrosion. The coating material to be applied depends on the type of corrosion and the environment where the corrosion occurs. The common methods for applying metallic coatings are electroplating and hot dipping.

b. Organic coatings

Organic coatings are generally composed from animal constituents, vegetables, or aggregates rich in carbon. They act as a barrier to an electrolyte and increase the electrical resistance of the coating. The most common coating is paint, which is relatively the most cost-effective type.

c. Powder coatings

Powder coatings are typically applied electrostatically as a dry powder and then heated to allow the coating to flow and form a "skin". Examples of powder coatings include vinyl, acrylic, nylon, and epoxy.

3.3.4 Material Selection

According to NORSOK D-010, the design requirement is all about selecting the best material that tolerates a corrosive environment and carries realistic loadings during the life of the well [1]. Materials in general are categorized into metals, polymers, ceramics, and composites. An important step of any project is to select the material that satisfies the design criteria before construction begins. The practical method to be used and the selection of the optimal material is a combination of design criteria (strength and corrosion), availability, and cost.

Different countries and oil and gas operators have their own material selection charts. For instance, NORSOK M-001 is a recommended material selection standard developed by the Norwegian government [20]. The standard is designed generally for injection and production wells in light of the operational conditions (temperature, pH, partial pressure of the corrosive gas, chloride concentration, etc.). As illustrated in Table 4, the application of different materials is limited by certain parameters. Figure 21 illustrates the material selection chart for low alloy steel grades (carbon steel) L-80 tubing. The chart presents data for pH and partial pressure of hydrogen sulfide

(pH_2S) and it shows the accepted standards for the use of low alloy steel grades tubing. The selection of the right material prolongs the life of the materials. It is therefore important to consult the recommended standards and best practices during the selection process.

Table 4: Production and injection tubing selection chart [21]

	Hydrocarbon production	Gas injection	Water Injection	Turnaround, WAG/SWAG	Disposal (Drill Cuttings)
Carbon steel			TO BE AVOIDED	TO BE AVOIDED	
Low alloy steels NOTE1	NOTE 2	NOTE 2	NOTE 2	NOTE 2	
3%Cr Alloyed Steel			TO BE AVOIDED	TO BE AVOIDED	TO BE AVOIDED
13%Cr Martensitic Stainless steel			TO BE AVOIDED NOTE 3	TO BE AVOIDED NOTE 3	TO BE AVOIDED
13Cr (5Ni 2Mo) Super Martensitic Stainless steel			TO BE AVOIDED NOTE 3	TO BE AVOIDED NOTE 3	TO BE AVOIDED
25%Cr Super Duplex Stainless Steel					NOT NORMALLY USED
Nickel based Alloys			NOT NORMALLY USED	NOT NORMALLY USED	NOT NORMALLY USED
Titanium Based Alloys	NOT NORMALLY USED	NOT NORMALLY USED			NOT NORMALLY USED
FRP/GRE lined Low Alloy Steel	NOT NORMALLY USED	NOT NORMALLY USED	NOTE 4	NOTE 4	NOTE 4

NOTE 1: LOW ALLOY STEELS FOR USE IN WATER SERVICE SHALL CONTAIN 1% CHROMIUM
NOTE 2: ACCEPTABLE WHEN FLOW VELOCITY IS BELOW 5 m/s (SOLIDS FREE)
NOTE 3: THESE ALLOYS ARE ACCEPTABLE FOR PRODUCED OR AQUIFER WATER WHEN DISSOLVED OXYGEN CONTROLS ARE MAINTAINED BELOW 10ppb FOR 100% OF THE INJECTION PERIOD.
NOTE 4: ACCEPTABLE WHEN FLOW VELOCITY IS BELOW 15 m/s (SOLIDS FREE)

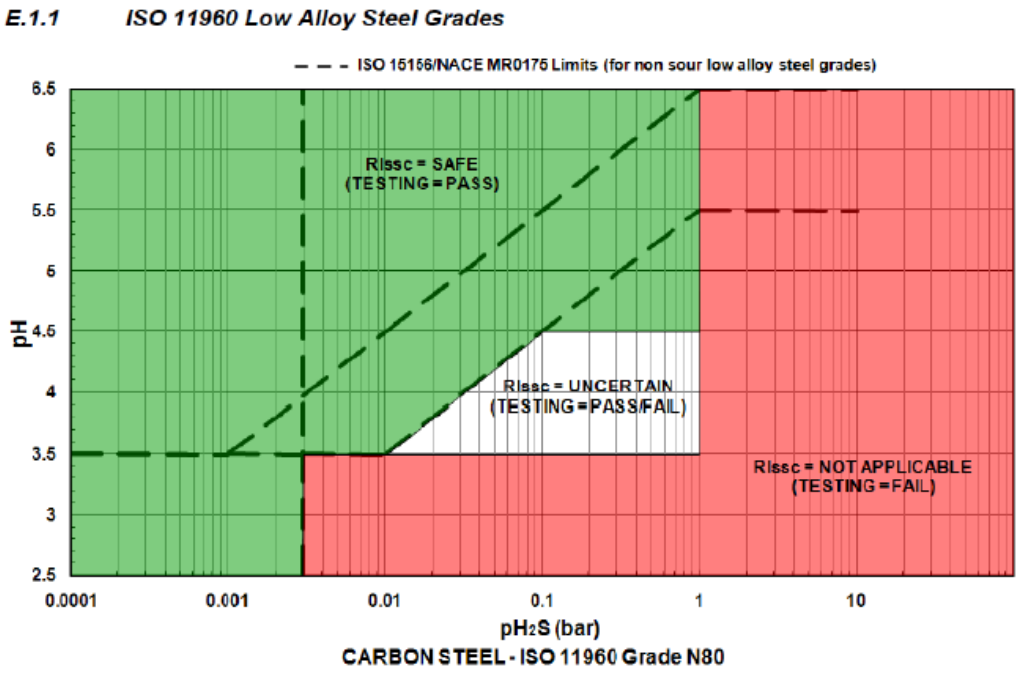

Figure 21: Low alloy steel grades chart [21]

3.4 Types of Corrosion

3.4.1 Uniform Corrosion

This type of corrosion is the most common. Its process occurs at approximately at the same rate over the exposed surface and leads to a uniform reduction of the thickness of the metal. The main cause of uniform corrosion is applying improper materials in corrosive environments. In acidic environments, hydrogen ion reduction occurs, while in an alkaline (pH > 7) or neutral (pH = 7) environment, oxygen reduction takes place. Both reactions arise uniformly and there is no preferential location for those processes. The corrosion attack process is generally an electrochemical process [2].

Figure 22 Uniform corrosion [22]

Uniform corrosion is the easiest to monitor and requires the least expensive monitoring techniques [2].

Prevention:

- Use thicker materials to allow for corrosion
- Use cathodic protection (sacrificial anode)
- Use paints or coatings

3.4.2 Pitting Corrosion

Corrosion damage occurs locally in this type of corrosion, by which cavities are produced in the material due to the outbreak of an open passive layer. The process of pitting corrosion first attacks the formation of a passive layer on the surface. There is a potential Hydrogen (pH) reduction in the interface between passive layers and electrolytes, resulting in the slow dissolution of the passive film and eventual rupture [23]. Since it is difficult to anticipate and detect, this type of corrosion is one of the most disastrous. In addition, the location of occurrence is very small but it can cause sudden equipment damage.

Prevention:

- Use cathodic protection
- Use higher alloys to increase resistance to pitting corrosion

- Use appropriate materials

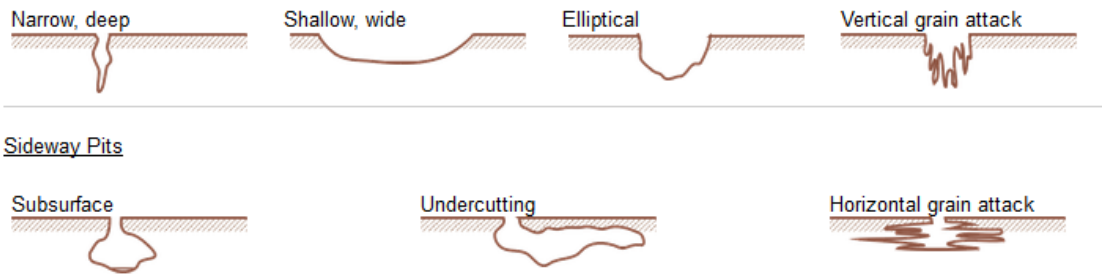

Figure 23 Types of pitting corrosion [24]

Figure 24 Pitting corrosion [24]

3.4.3 Crevice Corrosion

This type of corrosion has many similarities with pitting corrosion. Crevice corrosion is associated with stagnant solution conditions formed by particular geometries such as flanges, holes, gaskets, and so forth. Rothwell [23] states that a highly corrosive micro-environment will be formed as a result of the stagnant solution in the crevice geometry, identical to what happens in the case of pitting corrosion. Localized corrosion is initiated by different chemical concentrations of some chemical components, usually oxygen, that form an electrochemical concentration cell. In the stagnant solution space, the concentration of oxygen is lower relative to the bulk solution, which leads to the first attack of corrosion.

Like pitting corrosion, crevice corrosion is difficult to detect. The hidden damage that occurs needs special techniques to observe, such as using micro-electrodes or fiber optic sensing devices [23]. The methods used to control this type of corrosion are summarized as follows:

- Use higher alloys
- Use welds rather than bolted or riveted joints
- Use solid, non-absorbent gaskets such as Teflon
- Use continuous welding to eliminate crevices in lap joints

3.4.4 Galvanic Corrosion

Galvanic corrosion takes place when two different materials are connected to an electrolyte and have an electrical contact. The less noble material will be corroded preferentially and become the anode, while the more noble material will become the cathode and not be dissolved in the galvanic couple [23]. The differences of corrosion potential between the two materials become the main driving force of the corrosion rate.

To monitor galvanic corrosion, a sensor is required to measure the corrosion rates in real time [23]. Zero Resistance Ammetry (ZRA) is a simple technique that can be used to detect galvanic corrosion. Galvanic corrosion can be prevented using some methods such as:

- Select materials which have the same corrosion potentials
- Do not mix tube and fitting or valve alloys wherever possible
- Insulate parts of the material from each other
- Apply coatings to both materials
- Add inhibitors

3.4.5 Intergranular Corrosion

Intergranular corrosion is also called *intergranular stress corrosion cracking* because it may occur along the grain boundaries in the presence of tensile stress. In this type of damage, highly localized dissolution occurs along the grain boundaries due to composition differences that result in the grain being removed from the metallic alloys [23]. The corrosion attack will develop along the grain boundaries. A microscopic observation is usually needed to identify this corrosion. Prevention methods for this type of corrosion include:

- Use stainless steels with low carbon grades
- Apply titanium or niobium in the stainless steels to stabilize the elements

3.4.6 Stress Corrosion Cracking (SCC)

A lower concentration of sulfide can cause sulfide stress cracking (SCC), which is defined by the National Association of Corrosion Engineers (NACE) as "the cracking of a metal under the combined action of tensile stress and corrosion in the presence of water and H_2S [25]. This type of corrosion is caused by the combination of corrosive environment and differential stresses in materials, especially tensile stress. It is believed that corrosion and tensile stress have a symbiotic relationship, hence the corrosion as a result of the combined influence will form more damage than the sum of the individual effects. The factors needed to form SCC include hydrogen sulfide, water, tensile stress, and a liable material.

In stress corrosion, the area of highest stress becomes anodic, while the area of lower stress becomes cathodic; this can be observed at couplings. Stress corrosion cracking is regarded as the most complex of all corrosion types due to the various parameters that influence it such as the type of stress, stress level, temperature, microstructural features, and so forth. [23]. Detecting this type of corrosion can be very challenging. One of the methods to detect SCC events in certain systems is to use corrosion sensors which apply the electrochemical noise technique. Preventive methods against SCC include:

- Reduce the stress level and design out stress concentrations
- Use coating
- Appropriate material selection
- Minimize thermal and residual stresses
- Avoid the chemical components that cause SCC

3.4.7 Corrosive Gases

3.4.7.1 Hydrogen Sulfide Corrosion

Hydrogen sulfide is a poisonous, acidic, and dangerous gas which can be found naturally in crude oil and gas as well as in hot springs. It can lead to catastrophic damage to metals used by the oil industry in gas treatment facilities, pipelines, and oil refineries due to corrosion and sulfide stress corrosion cracking (see Figure 25). H_2S corrosion is mainly controlled as a result of the iron sulfide

film that is a by-product of the corrosion process [2]. Some other common prevention methods include:

- Use chemical inhibitors
- Apply galvanization process
- Apply cathodic protection

Figure 25 Hydrogen sulfide corrosion [26]

3.4.7.2 Carbon Dioxide Corrosion

CO_2 corrosion or "sweet corrosion" is one of most common corrosion type in oil and gas industry. This corrosion will form when CO_2 is dissolved in an aqueous phase state to build up an electrochemical reaction between steel and aqueous phase. CO_2 will be soluble in water and produce carbonic acid (H_2CO_3). It should be noted that CO_2 dry itself will not form corrosion at the temperature experienced within oil and gas production unless it is dissolved in an aqueous phase. CO_2 usually will form corrosion such as uniform corrosion, pitting corrosion, erosion corrosion, corrosion fatigue, and raindrop corrosion [2]. This reaction will produce carbonic acid (HCO_3^-) which is a weak acid compare to mineral acids since it does not fully dissociate [27].

CO_2 generally can be formed in oil and gas industry such as:

- CO_2 injection and sequestration
- Gas condensate wells

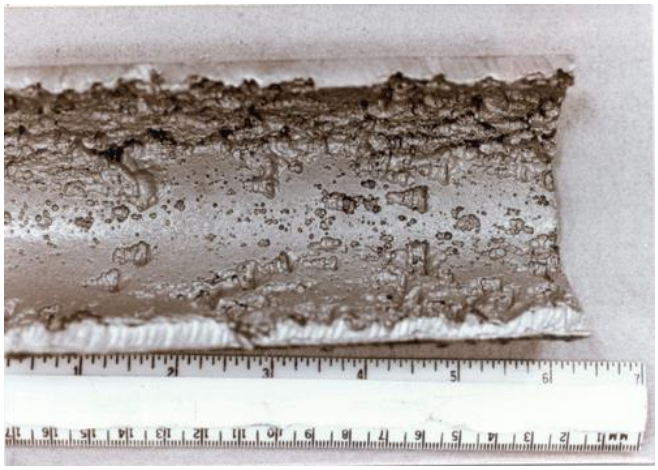

Figure 26 CO_2 corrosion [28]

3.4.7.3 Oxygen Corrosion

In oil and gas industry, oxygen corrosion mostly can be found in production or water injection systems and it is a highly reactive gaseous element. This corrosion is known as major hazards especially when sea water is injected into a reservoir for pressure maintenance.

As shown in Figure 27, an example of time-lapse caliper on an injection well has the thickness reduced from the top to the bottom due to the oxygen corrosion. The thickness reduction of the tubing at the bottom is much lower than the top since the oxygen has been consumed and no further corrosion takes place [9]. The poor removal of the oxygen prior to injection is one of the typical cause of oxygen existence in water injection cases. Hence, a proper way of removing oxygen shall be obtained to prevent the corrosion attack. The most common methods are using mechanical de-aeration (counter gas stripping towers or vacuum towers) and chemical scavenging (usually sulfites or sulfur dioxide).

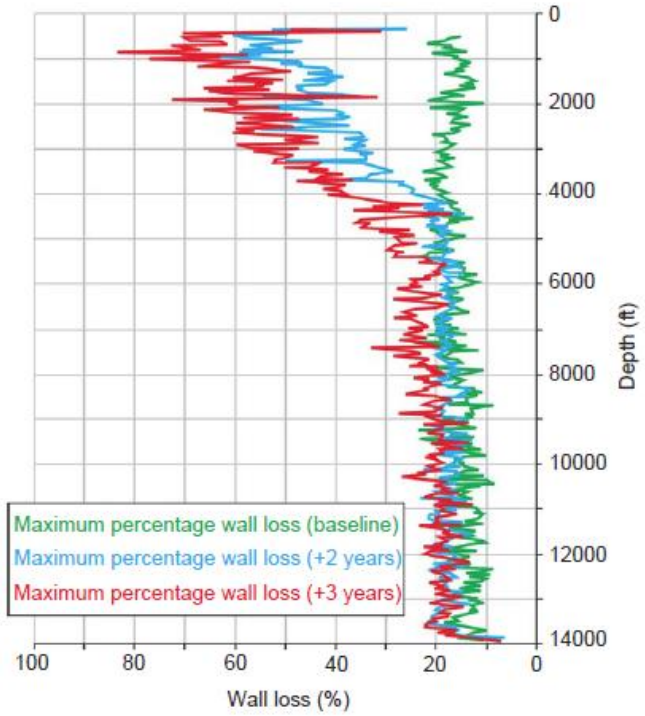

Figure 27 Time lapse caliper on a water injection well [9]

3.5 Corrosion in Oil Field Equipment

Corrosion can generate many problems in the oil and gas industry since it may attack any material at any stage in the life cycle of the well, from the drilling stage through the plug and abandonment process, and will increase operating costs significantly. It is important to understand the deterioration of the metal in every component in order to develop corrosion control strategies. Since it is almost impossible to prevent corrosion, controlling its rate may become the most economical solution. For the purposes of this study, the discussion in this thesis will be limited to casing, tubing, and drill pipe, artificial lift, well stimulation, surface equipment, and Enhanced Oil Recovery (EOR).

3.5.1 Casing, Tubing, and Drill Pipe

3.5.1.1 Drill Pipe Corrosion

In the drilling stage, the formation fluids coming out from the reservoir and the drilling fluids used can cause corrosion; this is a major cause of drill pipe failure. The most frequent corrosion

accelerator in drilling fluids is oxygen, which causes reduction in the thickness of the drill pipe. To improve the rate of penetration (ROP), oxygen may be purposely injected into the fluids stream. When stress is applied to the drilling equipment, the equipment will also be subjected to stress corrosion. The most common technique to control oxygen corrosion is to use oxygen scavengers.

When the formation being drilled contains hydrogen sulfide, H_2S corrosion problems will result. Additives used in drilling fluids such as water containing hydrogen sulfide and sulfate-reducing bacteria may also become contaminants. Even in a very low concentration of sulfide ions, H_2S can stimulate rapid corrosion rates and failures [29]. To counteract drill pipe failures, drill pipe with H_2S-resistant internal coating has been used, and it is well proven to control the corrosion rate. The common technique to detect hydrogen sulfide is to use an electrochemical sensor, but the industry has been developing detection methods using nanotechnology that can provide more accurate H_2S readings while using less energy than traditional methods [30].

3.5.1.2 Casing and Tubing Corrosion

a. Internal and Annulus Corrosion

Corrosion attacks on the internal surface of the casing or tubing typically are caused by hydrogen sulfide, oxygen, carbon dioxide, or organic acids used for well stimulation. The type of corrosion usually depends on the completion fluid. After the well is completed with a packer, the fluid will be a combination of reservoir fluids, drilling mud, and completion fluid. In many cases of corrosion, hydrogen sulfide coming out from the reservoir fluid that is produced is believed to be the main cause of the internal attack. The galvanic cell is the iron sulfide, and the pipe becomes an anode. This reaction is responsible for the pitting detected in sulfide corrosion [31]. After the perforation is completed to produce reservoir fluid, the casing-tubing annulus will be exposed to reservoir gases containing hydrogen sulfide. In the reservoir condition, the gas is saturated with water, and as the gas flows upwards through the hole, the water will condense on the surface of the casing area where the temperature is below the dew point. As a result, hydrogen sulfide will dissolve in the water droplets and corrosion will start. As the fluid is being produced, the fluid flow will increase the temperature to above dew point on the tubing and there will be no water

condensation. Hence, the corrosion rate on the tubing will be lower as compared to the casing [31]. Methods of preventing these types of corrosion include:

- Install packer with the annulus filled with corrosion inhibitor or sweet oil in the well; this may prevent internal corrosion, but this method will only provide corrosion prevention to the section above the packer
- Circulate corrosion inhibitor through the well
- Use casing with internal coating

b. External Corrosion

Corrosion attack on external casing is caused by several issues, separately or in combination. The discussion in this part is a summary of Goodnight‘s paper[31]:

1. **Acidic water attack**

   Formation water can contain acid gases such as hydrogen sulfide and carbon dioxide. If these gases react with the metal (casing), they will cause corrosion attack on the outside of the casing.

2. **Bacteria attack**

   Bacteria attack could cause severe localized pitting corrosion as a result of chemical attacks from the products of bacteria metabolism or decomposition, or due to depolarization of the metal surfaces due to their consumption of hydrogen. Bacteria capable of reducing sulfate is one of the main organisms that attack the outside of the casing. These anaerobic bacteria metabolize sulfate ions (SO_4) contained in water and soils using an organic carbon source and produce hydrogen sulfide (H_2S), which causes corrosion. The result of bacteria activity that leads to corrosion is shown in Figure 28.

Figure 28 Bacterial corrosion outside of casing [31]

3. Electrolytic effects

Electrolytic effects that can cause corrosion attack on the outside of the casing can be categorized into two cases: two different electrodes (galvanic) or the same electrode in different environments (electrolytic). In the galvanic case, the first electrode is the surface line and the second electrode is the subsurface line (casing), and both electrodes form a galvanic couple that produces corrosion. In the electrolytic case, the anode is the casing and the electrolyte is earth or the formation. When the formation is connected to the casing, the electric currents will flow through the anode and enter the electrolyte. As a result, corrosion will form at the anode. Electrolytic effects can be prevented by the following methods:

- Use cathodic protection such as sacrificial anodes or impressed currents to restrict current discharge on the casing by making the earth more positive than the casing
- Use coatings on the casing to isolate the steel structure from the electrolyte

3.5.2 Artificial Lift Corrosion

In depleted wells where the reservoir pressure is not strong enough to lift the reservoir fluids, the application of an artificial lift will significantly enhance well productivity. Electrical Submersible Pumps, Gas Lift, and Sucker Rod Pumps are some of the artificial lift methods that are currently in use. Each is associated with different types of corrosion.

3.5.2.1 Electrical Submersible Pumps (ESP)

ESP has been widely used as an artificial method especially for wells which have a high fluid rate and a high productivity index. The formation fluids that will be produced contain many natural components. When an ESP is installed in the well, it will add other materials to the system such as rubber used for ESP O-rings and other elastomers, nickel-alloy for pump components, galvanized armor for cables, and so forth. When the ESP interacts with the formation fluids, the main concern is that the fluids themselves contain hydrogen sulfide and cause SCC and hydrogen embrittlement, which leads to premature failure. Coatings, corrosion inhibitor, and special materials used to overcome the H_2S environment are commonly used to prevent the corrosion attack.

Gas Lift

The corrosion that occurs in gas lift systems usually takes place in the water-dependent type of wells, which typically experience no corrosion problems for years until water starts to produce significantly, at which point the corrosion rate becomes relentless [32]. These problems become more complicated with the presence of CO_2 from the produced gas as CO_2 also initiates corrosion. This condition usually leads to pitting corrosion and metal loss in the tubing string above the operating gas lift valve. Corrosion inhibitor injected through the gas stream and the proper selection of tubing material used for the gas lift system may help to prevent corrosion.

Sucker Rod Pumps (SRP)

Corrosion is one of the main causes of SRP failures, especially when dealing with an environment containing high salt content in formation water, oxygen, hydrogen sulfide, and so on. The SRP is operated under cyclic loading and has fatigue limits before failure. The corrosive components will reduce the fatigue strength of the sucker rods and limit the number of pump strokes. When the cyclic stress resulting from high loading is combined with the corrosive environment, it causes corrosion-fatigue failures which lead to more deterioration of the sucker rods than either fatigue or corrosion alone [33]. Protective coatings such as epoxy and spray metal couplings have been used in sucker rods to reduce corrosion rates. The use of chemical inhibitors has been proved to add string protection.

3.5.3 Well Stimulation

Well stimulation programs can promote internal corrosion due to the use of corrosive chemicals and additives such as hydrochloric acid (HCl) and hydrofluoric acid (HF). These acids will remove the scales formed inside the tubing and casing and improve permeability near the wellbore. However, the scales act as protective layers to prevent corrosion attacks. When the scales are removed after stimulation jobs, the injected acid will have direct contact with the metals and cause a higher corrosion rate. Hence, it is important to use corrosion inhibitors in order to have successful well stimulation jobs without corroding the well strings.

3.5.4 Enhanced Oil Recovery (EOR)

CO_2 injection and sequestration, steam injection, and polymer injection are some EOR methods that have been developed to optimize oil recovery. These techniques also play a critical role in the corrosion of the strings since the components injected into the reservoir contain corrosive constituents. In CO_2 injection and sequestration, CO_2 gases may come from in-situ gases or external injection. The higher CO_2 concentration will result in higher corrosion rates

3.6 CO_2 Corrosion Prediction Models

In this section, some of the experimental studies of uniform corrosion prediction models will be presented. In the interest of brevity, one example of uniform corrosion case will be chosen. In this case, CO_2 corrosion case will be reviewed in further detail.

A number of CO_2 prediction models have been established to estimate corrosion rates in the oil and gas industry, and these models vary from modeling-based to experiment-based. The main parameters that drive the model diverge for each model.

3.6.1 NORSOK M-506

The NORSOK M-506 standard "CO_2 Corrosion Rate Calculation Model" [34] was developed by the Norwegian petroleum industry and is based on a large amount of flow loop data from research programs at the Institute for Energy Technology (IFE) in Norway [35]. This empirical model is defined for carbon steel in water containing CO_2 at different pH, temperatures, wall shear stresses, and CO_2 fugacity.

The following general equation of the CO_2 corrosion rate for carbon steel is used at each of the following temperatures (t): 20°C, 40°C, 60°C, 80°C, 90°C, 120°C, and 150°C [34]:

$$CR_t = K_t \times {f_{CO_2}}^{0.62} \times \left(\frac{S}{19}\right)^{0.146+0.0324\log(fCO_2)} \times f(pH)_t \quad (mm/year) \tag{3.1}$$

The equation for temperature 15°C:

$$CR_t = K_t \times {f_{CO_2}}^{0.36} \times \left(\frac{S}{19}\right)^{0.146+0.0324\log(fCO_2)} \times f(pH)_t \quad (mm/year) \tag{3.2}$$

The equation for temperature 5°C:

$$CR_t = K_t \times {f_{CO_2}}^{0.36} \times f(pH)_t \quad (mm/year) \tag{3.3}$$

where

K_t is a constant dependent upon temperature

f_{CO2} is the fugacity of CO_2

S is the wall shear stress (Pa)

$f(pH)_t$ is a complex function of pH

t is temperature (°C)

Some limitations for the basic input parameter in this model are given in Table 5. For corrosion at the value of temperatures above and below the required value, linear interpolation can be used.

Table 5: Limitations for basic input parameters for NORSOK M-506 model [34]

Parameter	Units	Range
Temperature	°C	5 to 150
	°F	68 to 302
Total pressure	bar	1 to 1000
	psi	14.5 to 14500
Total mass flow	kmole/h	103 to 105
CO_2 fugacity in the gas phase	bar	0.1 to 10
	psi	1.45 to 145
	mole %	variable
	kmole/h	variable
Wall shear stress	Pa	1 to 150
Acidity	pH	3.5 to 6.5
Glycol concentration	weight %	0 to 100

Stein Olsen [36] pointed out that the NORSOK M-506 model has some of the limitations as follows:

- When H_2S is present, this model cannot be implemented since it was developed based on experimental data without H_2S in the system.
- When total content of organic acids is higher than 100 ppm and the CO_2 partial pressure (pCO_2) is less than 0.5 bars, the corrosion rate prediction is more pessimistic.
- When amines or sodium hydroxide are present in the system, this model cannot be implemented.
- A system with temperatures lower than 20°C is set equivalent to a system at 20°C since this model was initially developed based on experimental data for temperatures higher than 20°C.

3.6.2 De Waard, Lotz, and Milliams 1991 (DLM)

In 1975, De Waard and Milliams first presented an experiment-based model to predict the corrosion rate [37]. This early model was based on the temperature and pCO_2 only and showed that the corrosion rate increases at temperatures from 30°C to 60°C, and the maximum rate occurs at temperatures between 60°C to 70°C. Then it decreases after 70°C until 90°C. In 1991, an improved model was proposed which took into account the correction factors for CO_2 at high pressure, the formation of $FeCO_3$ scales, and changes in pH and F_E^{2+} ion concentration. This model

uses the assumption that the CO_2 corrosion is an Arhennius or activation-controlled type of corrosion, meaning that the concentration of the reacting constituents depends on the pCO_2 [35]. The DLM equation is given by [38]:

$$log(C_{DLM}) = 5.8 - \frac{1710}{T} + 0.67\ log(f_{CO_2}) \tag{3.4}$$

where

C_{DLM} is the corrosion rate in mm/year

T is the temperature in Kelvin

f_{CO2} is the CO_2 fugacity in bar

The model in equation 3.4 was revised to include the impact of $FeCO_3$ protective film on the corrosion rate, represented as the scale temperature, T_{Scale}, as [38]:

$$T_{Scale} = \frac{2400}{6.7+0.6\log(f_{CO_2})} \tag{3.5}$$

where T_{Scale} is the temperature where the corrosion rate is at the maximum after the predicted corrosion rate is reduced by a scale factor F_{Scale} [35]:

$$\log(F_{Scale}) = 2400\ \left(\frac{1}{T} - \frac{1}{T_{Scale}}\right) \quad for\ T > T_{Scale} \tag{3.6}$$

$$\log(F_{Scale}) = 0 \qquad for\ T \leq T_{Scale} \tag{3.7}$$

Hansen [39] stated that there are some limitations of the DLM model. It is valid only for:

- Non-turbulent flow
- Clean carbon steel surfaces and unprotected by surface deposits
- Immersed service
- Systems that have no cathodic polarizers

3.6.3 De Waard, Lotz, and Dugstad 1995 (DLD)

The De Waard 1991 model has been revised two times. The first [40] revised the correlation between corrosion rate and velocity, temperature, and pCO_2. The second [41] proposed a semi-empirical model for corrosion rate prediction that combines a flow-dependent mass transfer of CO_2 and the flow-independent kinetics of the DLM model. The DLD version is the best fit to most of the corrosion flow loop data data generated at the author's laboratory [42].

The DLD model is given as [41]:

$$\frac{1}{C_{DLD}} = \frac{1}{C_{Act}} + \frac{1}{C_{Mass}} \tag{3.8}$$

where C_{DLD} is the corrosion rate in mm/year and C_{Act} is the contribution from the activation reaction kinetics given by [41]:

$$(log\ C_{Act}) = 4.93 - \frac{1119}{T} + 0.58\ log\left(f_{CO_2}\right) \tag{3.9}$$

where

f_{CO2} is CO_2 fugacity in bar and T is the temperature in Kelvin.

C_{Mass} is the contribution from the mass transfer kinetics and is given by:

$$C_{Mass} = 2.45\frac{U^{0.8}}{d^{0.2}} f_{CO_2} \tag{3.10}$$

3.6.4 Comparison of Data Input for Modeling Based Equations

The comparison of data input variables required by each model is shown in Table 6. The NORSOK and DLD models are a function of several variables needed compared with DLM model. In the NORSOK model, the fluid and pipe parameters such as density, viscosity, velocity, and pipe

diameter are included in the Reynolds Number (Re), and this parameter is needed to calculate S. For DLM and DLD, the constants in the model include change in density and viscosity with temperature.

Table 6: Data input variables required by each model [35]

Data Input	NORSOK	DLM	DLD	Value
T	√	√	√	20 - 140 0C
f_{CO2}	√	√	√	0.1 - 3 bar
pH	√			
U			√	1 m/s
S	√			
d			√	0.1 m
ρ				
μ				

Chapter 4 Simulation Studies

This chapter presents tubing damage modeling and design de-rating related simulation studies. The effect of CO_2 in various conditions and the factors that affect corrosion rate will be presented first. The use of WELLCAT for tubing design, PROSPER for gas lift design, and finally, FEM-based modeling will then be discussed.

4.1 CO_2 Effect on Tubing Simulation Studies

In this section, the prediction of CO_2 corrosion rate based on the three experimental models explained in Chapter 2 will be tested and the same data input will be used. In addition, the simulation results for the NORSOK model will be discussed in further detail.

4.1.1 Simulation Setup

A simulation sensitivity study on some parameters that have an impact on corrosion rate such as temperature, CO_2 fugacity, and pH will be performed. The input data used throughout the simulation is shown in Table 7. The well data used are from the tubing design exercise in the PET 600 Well Completion Course at the University of Stavanger, and the reservoir and fluids parameters are taken from averaged data from wells in the Norwegian Continental Shelf (NCS).

Table 7: Data input for CO_2 corrosion rate simulation

General Data Input		
Parameter	**Value**	**Unit**
Temperature	20 - 110	^{0}C
CO_2 Fugacity	0.5 - 3	bar
Pressure	372.3	bar
Mole CO_2	1	%
Additional Data Input for NORSOK Model		
Liquid Superficial Velocity	0.4	m/s
Gas Superficial Velocity	0.2	m/s
Water Cut	50	%
Pipe Inner Diameter	3.548	in
Water Type	Formation water	
Bicarbonate	400	mg/l
Ionic Strength	50	g/l

A computer program for calculating CO_2 corrosion rate developed by NORSOK standard is based on equations 3.1, 3.2, and 3.3. The normative reference for using this model is NORSOK M-001 "Materials Selection" [20]. This model also contains modules to calculate wall shear stress and pH. The main screen of the software is shown in Figure 29.

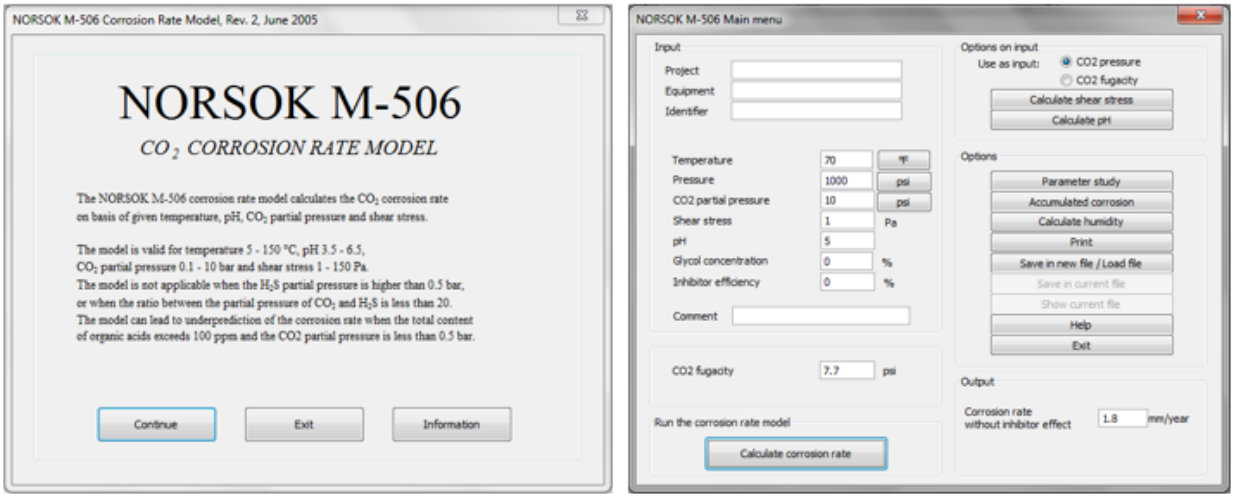

Figure 29: NORSOK M-506 main screen

4.1.2 Simulation Results

4.1.2.1 Effect of Temperature on Corrosion Rate

Figure 30 shows the corrosion rate predictions obtained from the NORSOK model over the temperature range 70°F – 230°F. For the temperatures in the range of 70°F – 120°F, the corrosion rate increases with the temperature. On the other hand, starting from 130°F, the corrosion rates decrease very gently as the temperature increases up to 170°F. Above 120°F, the model shows a decline in corrosion rate since it takes into account the effect of the precipitation of iron carbonate. Solid iron carbonate precipitates on the steel surface when the concentration of Fe^{2+} and $CO3^{2-}$ ions exceeds the solubility limit [35]. This generates the iron carbonate ($FeCO_3$) film that reduces the corrosion rate by forming a protective layer, establishing a diffusion barrier for the constituents involved, and inhibiting the underlying steel from further dissolution [43]. For corrosion occurring at the value of temperatures above and below the required value, linear interpolation can be used.

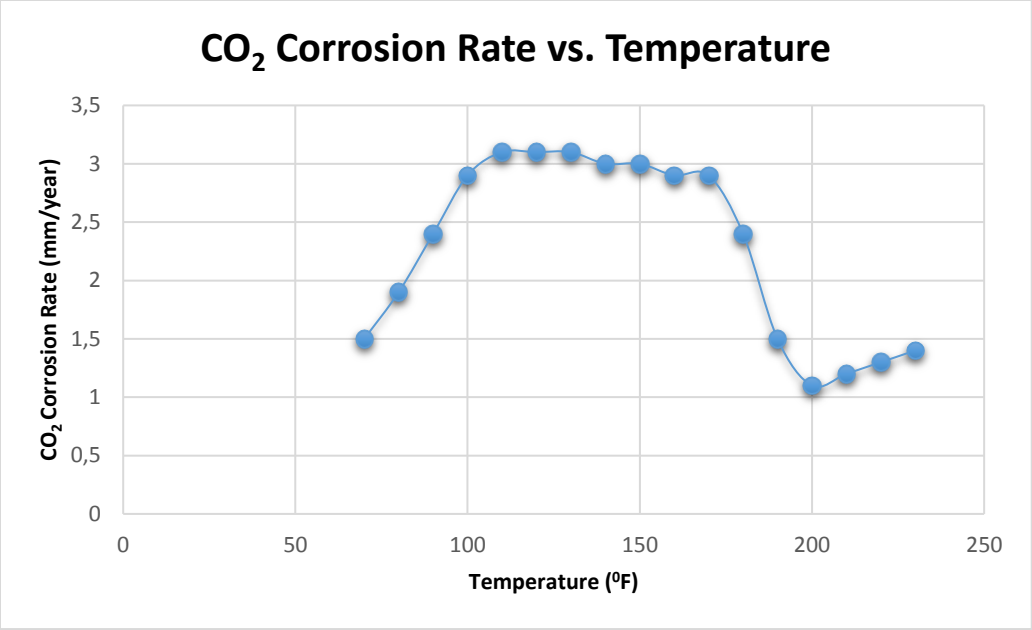

Figure 30: Corrosion rate prediction from NORSOK model for a range of temperatures from 70°F - 230°F

Using the same input parameters, the corrosion rate predictions obtained from the DLM and DLD models are compared with the NORSOK model. Figure 31 shows the simulation results for different models. As shown, below 170°F, all models show that the corrosion rate decrease with the temperature due to the effect of the formation of protective iron carbonate film. It has to be pointed out that the NORSOK model takes greater account of the effect of protective corrosion films [44].

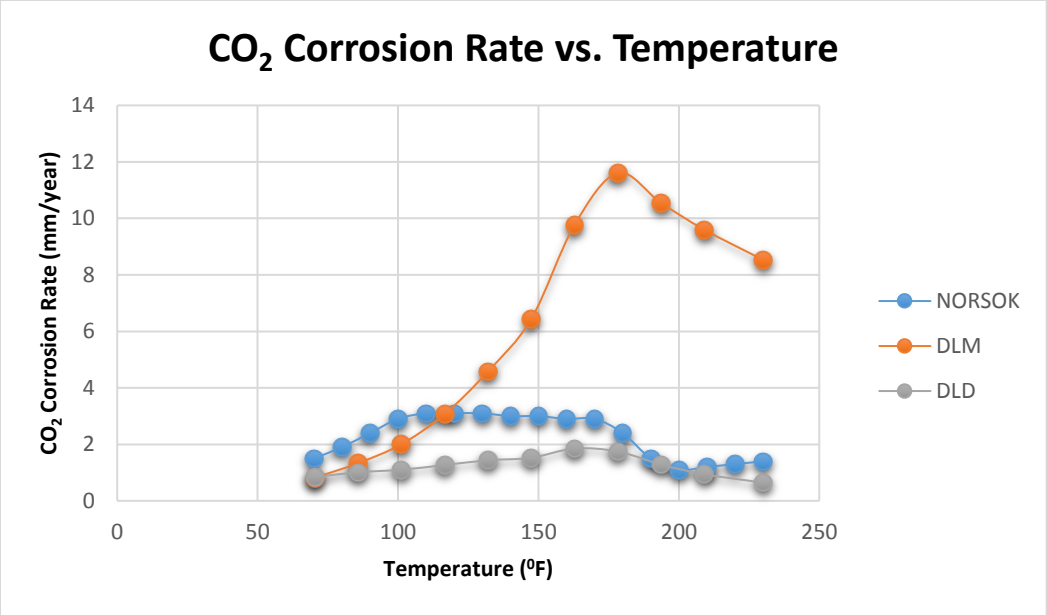

Figure 31: Corrosion rate prediction for a range of temperature from 70°F - 230°F

4.1.2.2 Effect of pH on Corrosion Rate

Figure 32 shows the NORSOK model corrosion rate prediction for tubing that is exposed to pH 3.5 – 6.5. The result shows that the corrosion rate decreases as the pH increases. The presence of hydrogen ions in the solutions with the ability to interact with the metal surface is the main factor that promotes corrosion. Shreir [45] stated that low-pH solutions accelerate corrosion by providing hydrogen ions and increase the redox potential of aqueous solutions with an increased corrosion rate as a consequence. In this case, the NORSOK model is considerably more sensitive to the variation in pH. To control the corrosion rate, it is necessary to maintain high pH to reduce the effects of acid. The most common method is to neutralize acids caused by CO_2 by applying neutralizer products.

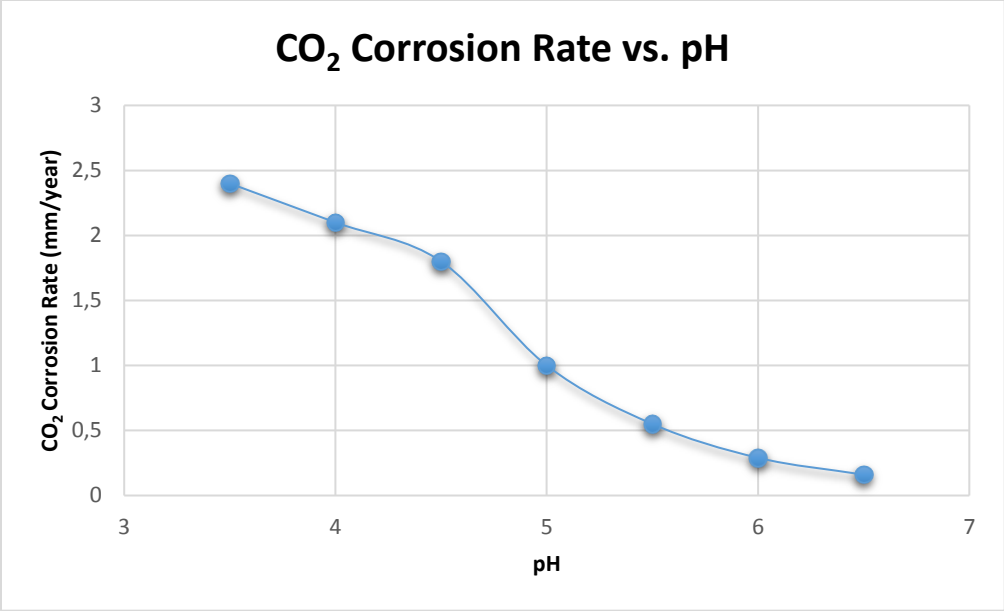

Figure 32: Corrosion rate prediction for a range of pH from 3.5 – 6.5 at temperature 176°F

4.1.2.3 Effect of CO_2 Fugacity on Corrosion Rate

Figure 33 shows the corrosion rate prediction due to the effect of CO_2 fugacity in the range of 8 – 42 psi. The trend shows an increase in corrosion rate as CO_2 fugacity increases. CO_2 fugacity highly influences the corrosion rate, and the relationship is directly proportional. The fugacity itself is defined as the corrected partial pressure of a gas and is equivalent to partial pressure under ideal conditions.

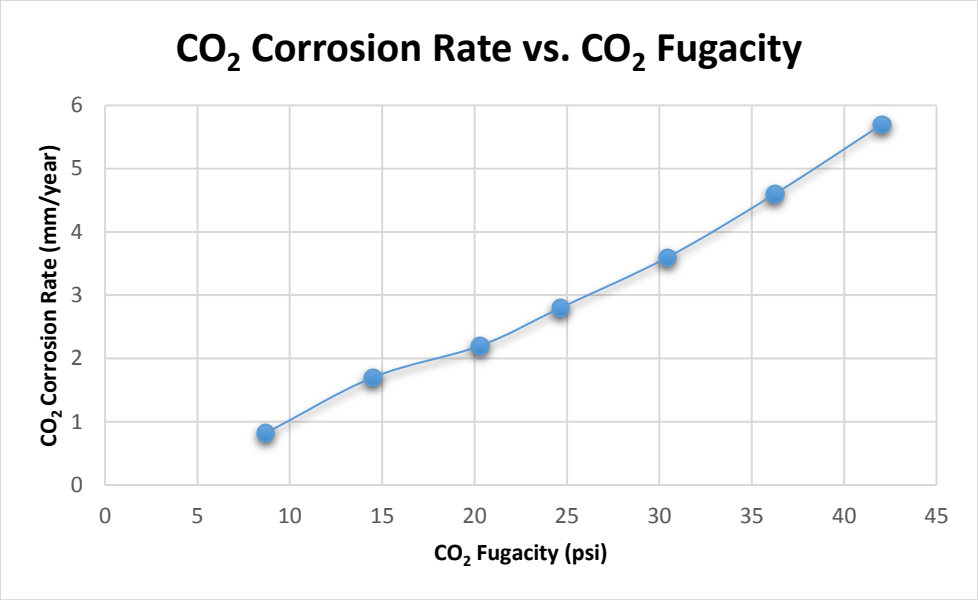

Figure 33: Corrosion rate prediction for a range of CO2 fugacity from 8 – 42 psi at temperature 176°F

The equation to calculate CO_2 fugacity for the NORSOK model is given as [36]:

$$f_{CO_2} = a \times p_{CO_2} \tag{4.1}$$

$$fp_{CO_2} = (mole\ \%CO_2\ in\ the\ gas\ phase\ (kmole/h) \times P \tag{4.2}$$

The fugacity coefficient (a) is given as:

$$a = 10^{P \times (0.0031 - 1.4/T)} \qquad \text{for P} \leq 250 \text{ bar} \tag{4.3}$$

$$a = 10^{250 \times (0.0031 - 1.4/T)} \qquad \text{for P} \geq 250 \text{ bar} \tag{4.4}$$

As shown in equation 4.2, CO_2 fugacity highly depends on the mole concentration of the CO_2 and pressure.

Figure 34 shows the corrosion rate prediction results obtained from the three models with the same range of CO_2 fugacity at temperature 176°F. All models have the general trend that the corrosion rate increases as the CO_2 fugacity increases. Among the three models, the DLM model predicts the highest corrosion rate.

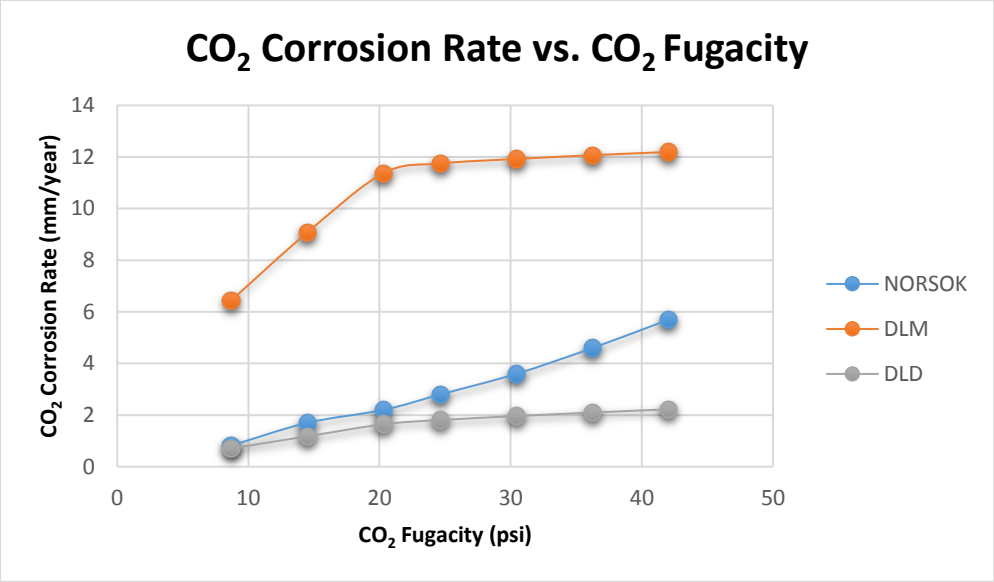

Figure 34: Corrosion rate prediction for a range of CO_2 fugacity from 8-42 psi at temperature 176°F

4.1.2.4 Effect of Inhibitor on Corrosion Rate

NORSOK M-001 [20] recommends the use of the inhibitor efficiency concept to determine the inhibited corrosion rate. Olsen [36] defined this concept as the reduction of the un-inhibited predicted CO_2 corrosion rate in %. It can be measured by the following equation:

$$E_f = \frac{R_i - R_o}{R_o} \tag{4.5}$$

where

- E_f is inhibitor efficiency (%)
- R_i is corrosion rate of metal with inhibitor
- R_o is corrosion rate of metal without inhibitor

The effect of inhibitor efficiency is entered directly as a reduction factor in the corrosion rate prediction. Figure 35 shows the predicted corrosion rate for a range of inhibitor efficiency of 0 – 30% for different temperatures. The general trend is shown as a decrease in corrosion rate as the inhibitor efficiency increases for each temperature.

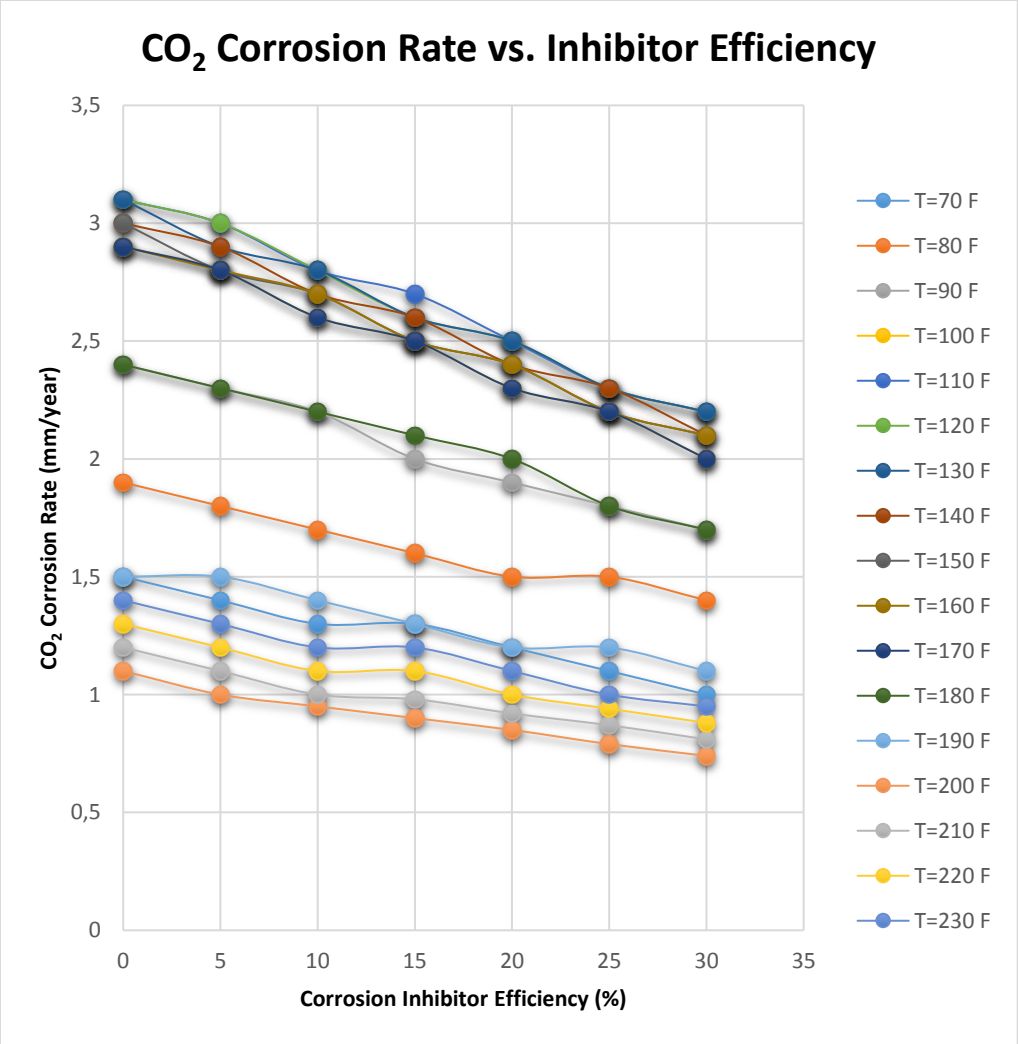

Figure 35: Corrosion rate prediction for a range of inhibitor efficiency from 0 – 30%

The application of corrosion inhibitor is essential to control corrosion and prevent tubing failure. Figure 36 shows the accumulated tubing thickness reduction for different inhibitor efficiencies from 2017 to 2021. The thickness reduction is lower when inhibitor efficiency is higher. If the thickness reduction is too large, the tubing will leak.

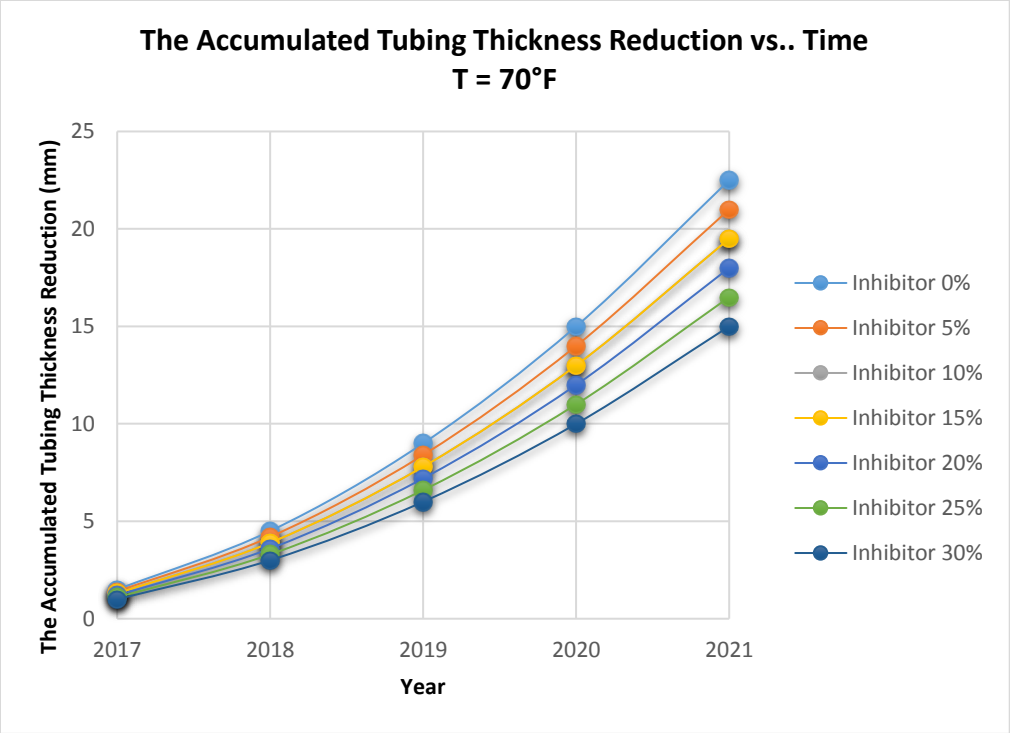

Figure 36: The accumulated tubing thickness reduction for different inhibitors (2017 to 2021)

4.2 WELLCAT Simulation

WELLCAT is part of the Landmark Solutions software (Halliburton, Houston, United States) used to provide solutions for both casing and tubing design and wellbore analysis. As mentioned in section §1.1, tubing damage in production tubing reached 47% reduction in wall thickness. Therefore, in this section, tubing simulation for different wear depth (5 – 50%) will be performed. The idea behind this simulation is that a uniform corrosion attack on production tubing will reduce its thickness. By the time of well production, the reduction will increase and affect material strength. Some loadings due to production and well service will be applied and the Von-Mises stress will be observed. The tubing design workflow in WELLCAT is summarized in Figure 37.

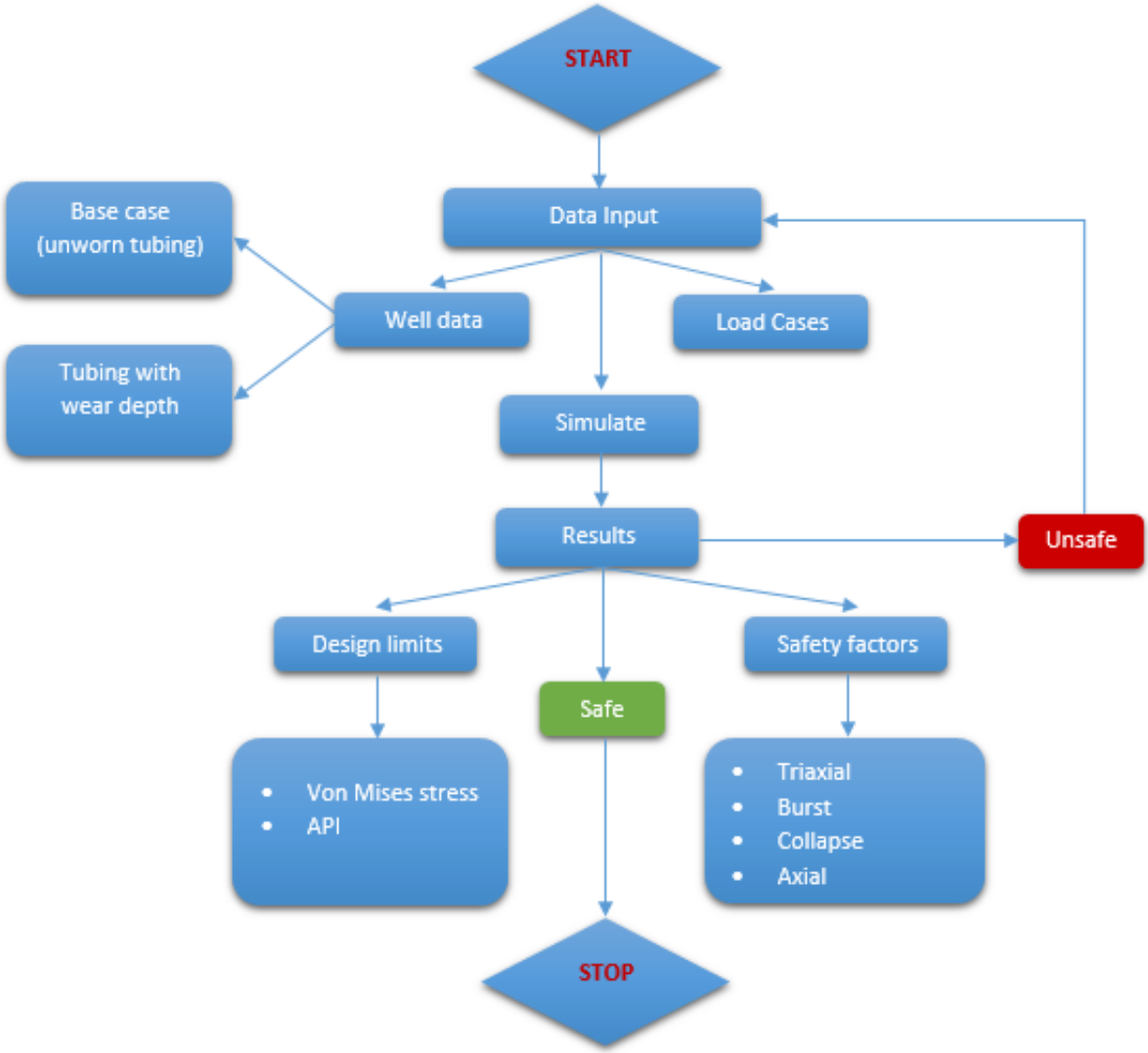

Figure 37: Tubing design workflow in WELLCAT

4.2.1 Simulation Setup

In this simulation, a fictitious well with the data taken from the PET-600 Well Completion Course at the University of Stavanger will be used. Tubing with OD 4.000 inch is used for the base case simulation, and the data are shown in Table 8. The casing and tubing configuration dataset in WELLCAT is shown in Table 9 and the well structure is presented in Figure 38. The main objective of this simulation is to illustrate how tubing damage responds to loading that was within the safe operational window for undamaged tubing.

As illustrated in Figure 37, when the simulation result shows that the tubing is unsafe, the operators should re-calculate the appropriate loading magnitude until the loads are within the allowable safe operational envelope.

Table 8: Production tubing data for base case

Production Tubing Data		
Grade	T-95	
OD	4	in
ID	3.548	in
Yield strength	95000	psi
Thickness	0.226	in
Weight	9.50	lb/ft

Table 9: Casing and tubing configuration

Name	**Type**	**OD (in)**	**MD (ft)**			**Hole Size (in)**	**Annulus Fluid (ppg)**
			Hanger	**TOC**	**Base**		
Conductor	Casing	18.625	0	600	2000	24.00	Mud 8.8
Surface	Casing	13.375	0	1500	5400	14.50	Mud 10.0
Production	Casing	9.625	0	6800	9700	12.25	Mud 11.2
Production	Liner	7.000	9200	9200	13000	8.50	Mud 12.0
Production	Tubing	4.000	0		12800		Mud 10.0

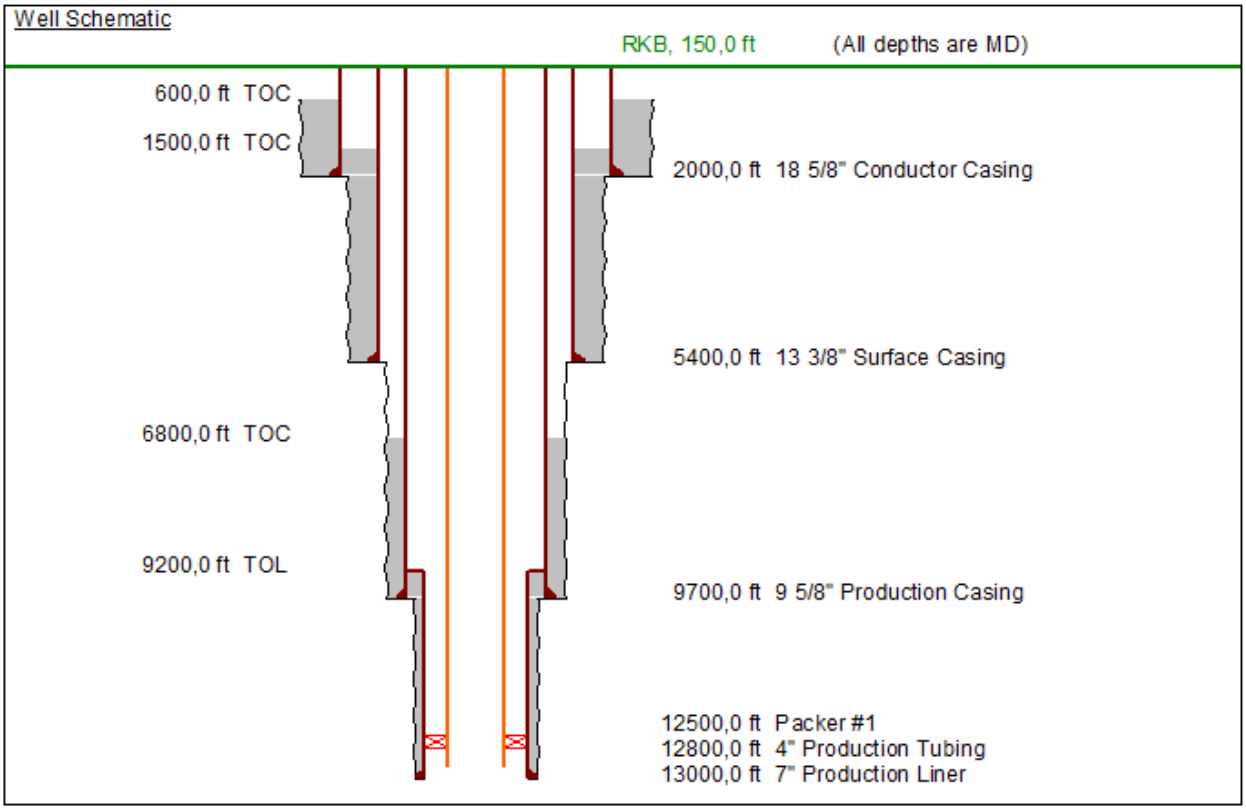

Figure 38: Well structure

Tubing for different wear depth (5 – 50%) is calculated. The deration represents the reduction in thickness due to corrosion during production. In this case, since uniform corrosion is assumed, tubing thickness is reduced uniformly over the inner surface. The assumption is that the corrosion attacks only the inner diameter of the tubing. Hence, for all wear depth, the outer diameter is constant while the inner diameter changes. Tubing size data for different wear depth are shown in Table 10.

Table 10: Tubing size for different wear depth

Wear Depth (%)	Reduced Thickness (in)	New thickness (in)	Area (m^2)	OD (in)	New ID (in)	Weight (ppf)
0	0	0.226	2.68	4	3.548	9.50
5	0.011	0.215	2.55	4	3.571	9.05
10	0.023	0.203	2.42	4	3.593	8.60
15	0.034	0.192	2.30	4	3.616	8.15
20	0.045	0.181	2.17	4	3.638	7.69
25	0.057	0.170	2.04	4	3.661	7.23
30	0.068	0.158	1.91	4	3.684	6.77
35	0.079	0.147	1.78	4	3.706	6.30
40	0.090	0.136	1.65	4	3.729	5.84
45	0.102	0.124	1.51	4	3.751	5.37
50	0.113	0.113	1.38	4	3.774	4.89

4.2.2 Loading Scenarios and Design Factors

All possible combinations of loadings which could occur during the life of a well should be considered. Based on these loadings, the right tubing in terms of load carrying capacity can be selected. Tubing will experience different loading cases during production such as installation, production, and well service loads. It is important to define the new limit of material strength after it is de-rated so that appropriate loadings can be applied without damage the tubing. In this case, the same loadings will be applied to unworn and de-rated tubing, then the stress distribution will be observed. The loads applied in this case are summarized in Table 11.

Table 11: Load cases

Load Case	Pressure at Perforation (psi)	Tubing Pressure (psi)	Annulus Pressure (psi)	Remarks
Pressure test tubing		5000	0	
Pressure test annulus		0	5000	
Early stage production	4600		0	
Steady state production - GL	4600		3500	Check valve depth = 9000 ft MD Gas injection rate = 4.9 MMSCF/D
Late stage production - GL	4600		3500	
Shut in short - GL		2500	0	
Shut in long - GL		2500	0	
Bullheading - GL		3000	0	
Pump kill fluid		2500	0	

The design factors for the pipe body set in this simulation are based on NORSOK Standard D-010 [1] and for the connections are based on Landmark modules. Pipe body strength ratings are usually based on yield, while connection strength calculations are based on failure. Hence, tension and/or compression design factors can be applied differently to the connections. The design factors set in this simulation are presented in Table 12 and Table 13.

Table 12: Design factors for pipe body [1]

Failure Mode	Design Factor
Tri-axial	1.25
Burst	1.10
Collapse	1.10
Axial Tension	1.30
Axial Compression	1.30

Table 13: Design factors for connections

Failure Mode	Design Factor
Burst/leak	1.10
Tension	1.30
Compression	1.30
Envelope Burst	1.00
Envelope Collapse	1.00

4.2.3 Von-Mises Equivalent (VME) Design Limits

Von-Mises stress (also known as Tri-axial stress) considers the combined effect of all the principal stress and it is useful to compare the stress state of material with its yield limit. In WELLCAT, the design limits combine VME with API burst, collapse, and axial plots. A state of stresses within the envelope is interpreted as safe and outside is interpreted as failure.

The design limit plots for unworn and 10% wear depth tubing are shown in Figure 39 and Figure 40. Comparing these two plots, it is apparent that for all loading cases, unworn tubing is in a safe condition while tubing with 10% wear depth is in a failure zone since some loadings such as bullheading and pump kill fluid exceed the design limits of the connection tension. It has to be pointed out that since the de-rated tubing has a reduced thickness due to corrosion, the material

strength decreases, with the result that the design limits window is narrower compared to unworn tubing.

Figure 41 to Figure 44 also show that some loadings are more sensitive in terms of the change of design limits such as bullheading, pressure test tubing, and pump kill fluid. By applying a slight reduction of the tubing thickness, these loadings move relatively closer to the Von-Mises limit compared to other loadings. Simulation results show that the only tubing for which the loadings are within the safe window is the unworn tubing in Figure 42.

This simulation demonstration suggests that during the life of a well, it is important to monitor the condition of tubing and perform re-design calculation based on the severity of the damage.

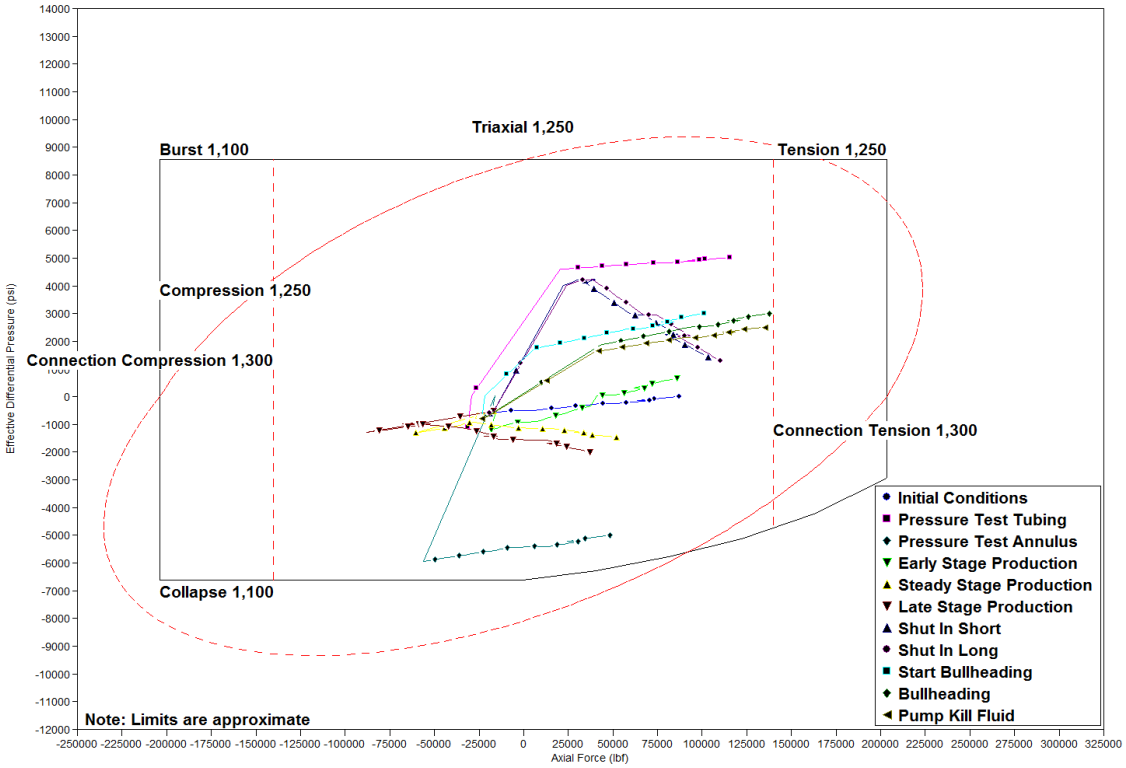

Figure 39: Design limits for various loads for unworn tubing

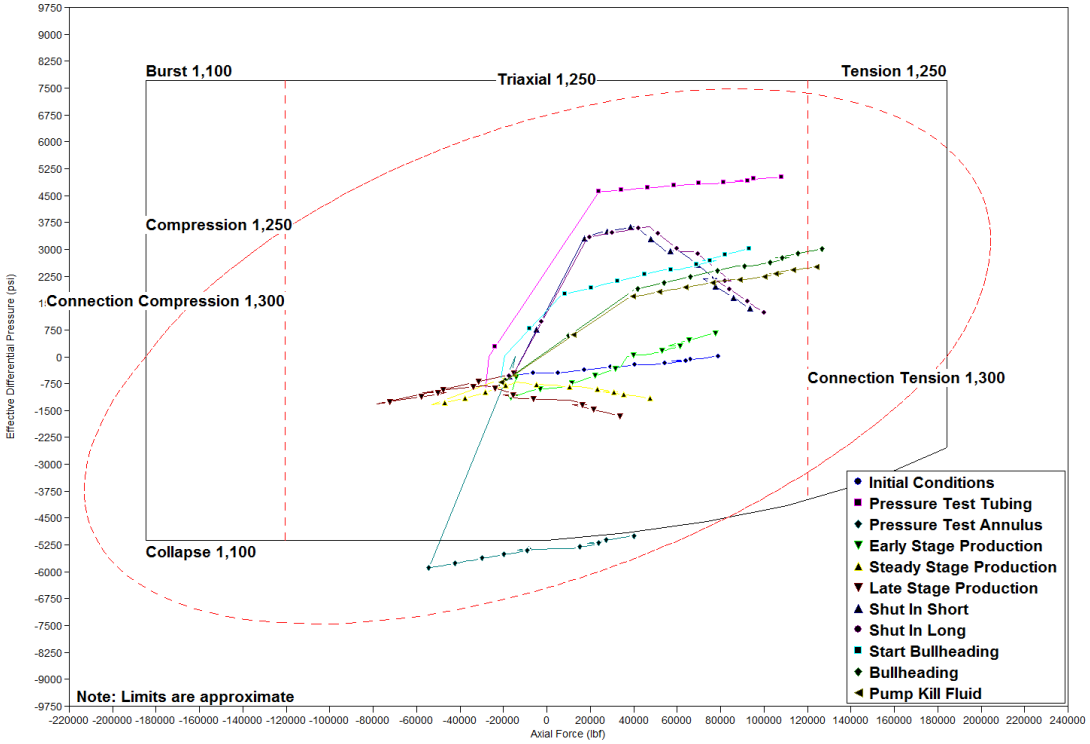

Figure 40: Design limits for various loads for tubing with 10% wear depth

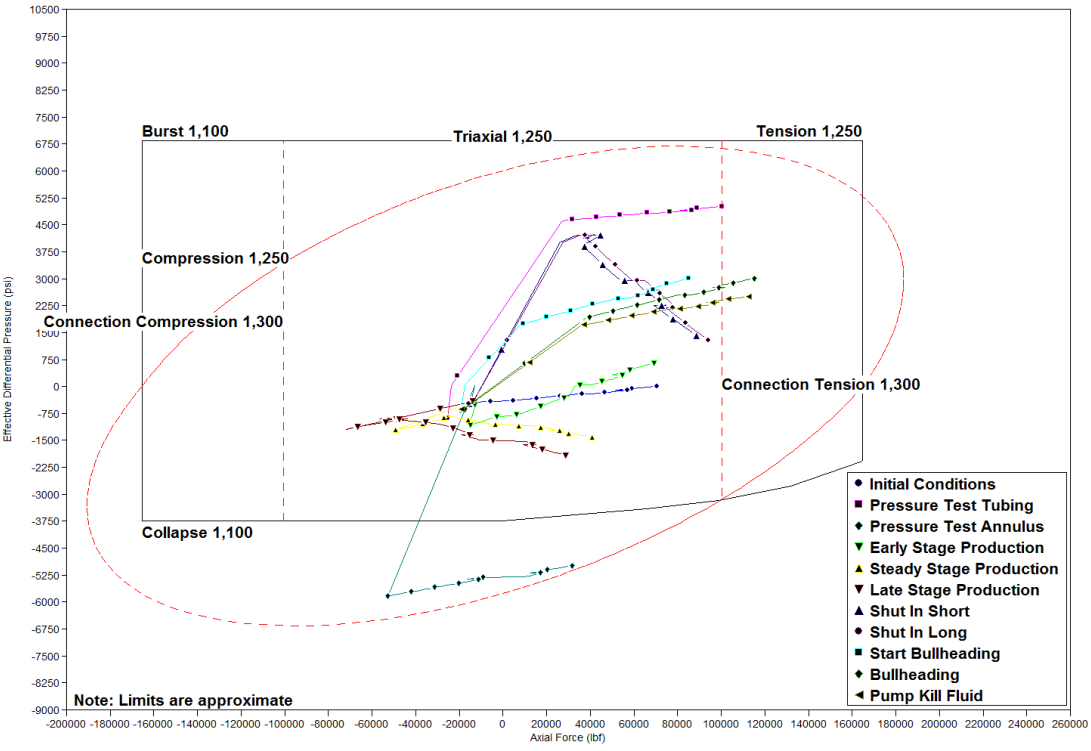

Figure 41: Design limits for various loads for tubing with 20% wear depth

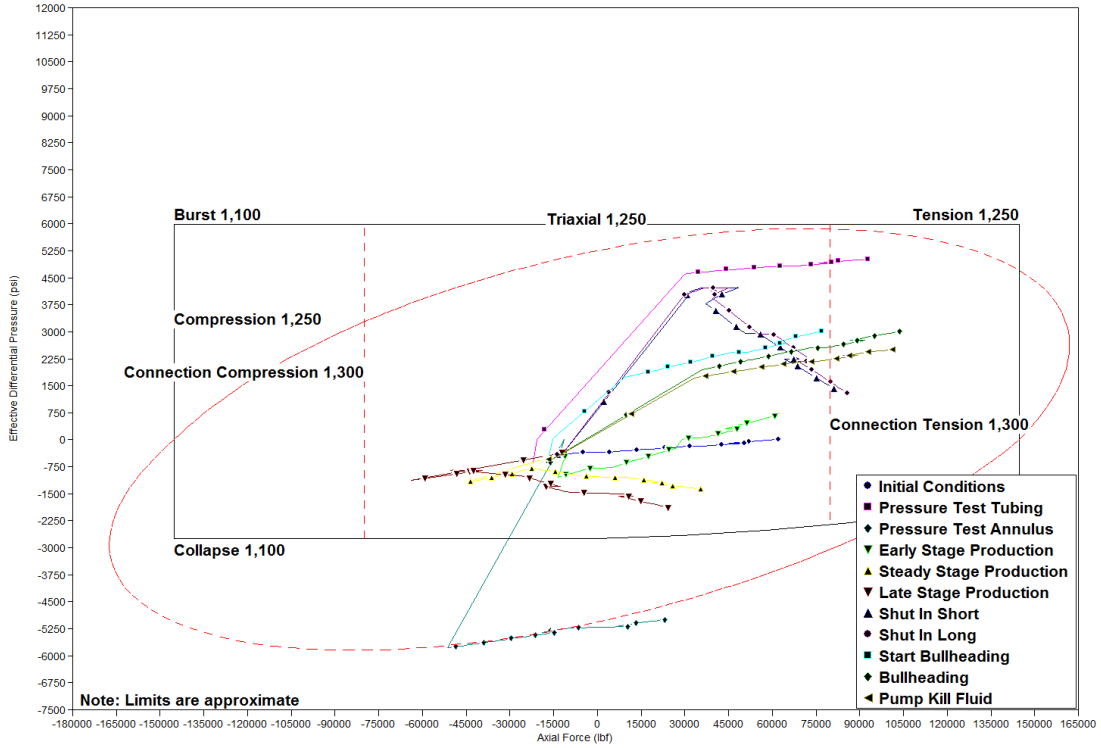

Figure 42: Design limits for various loads for tubing with 30% wear depth

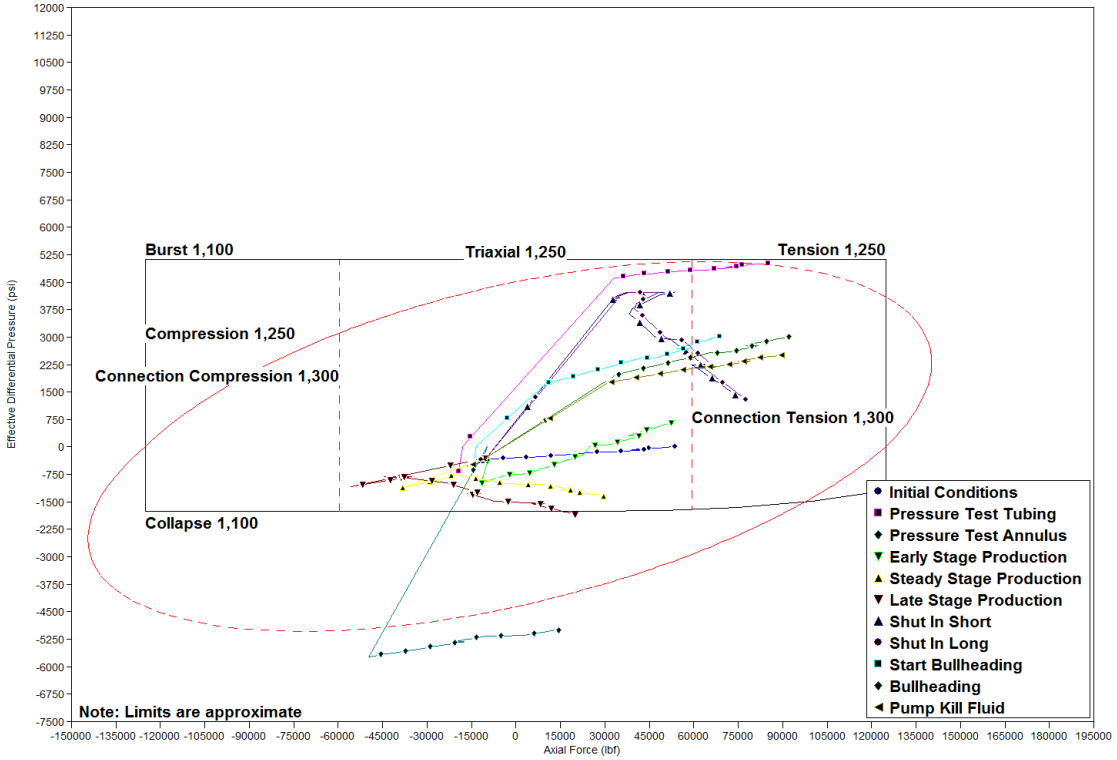

Figure 43: Design limits for various loads for tubing with 40% wear depth

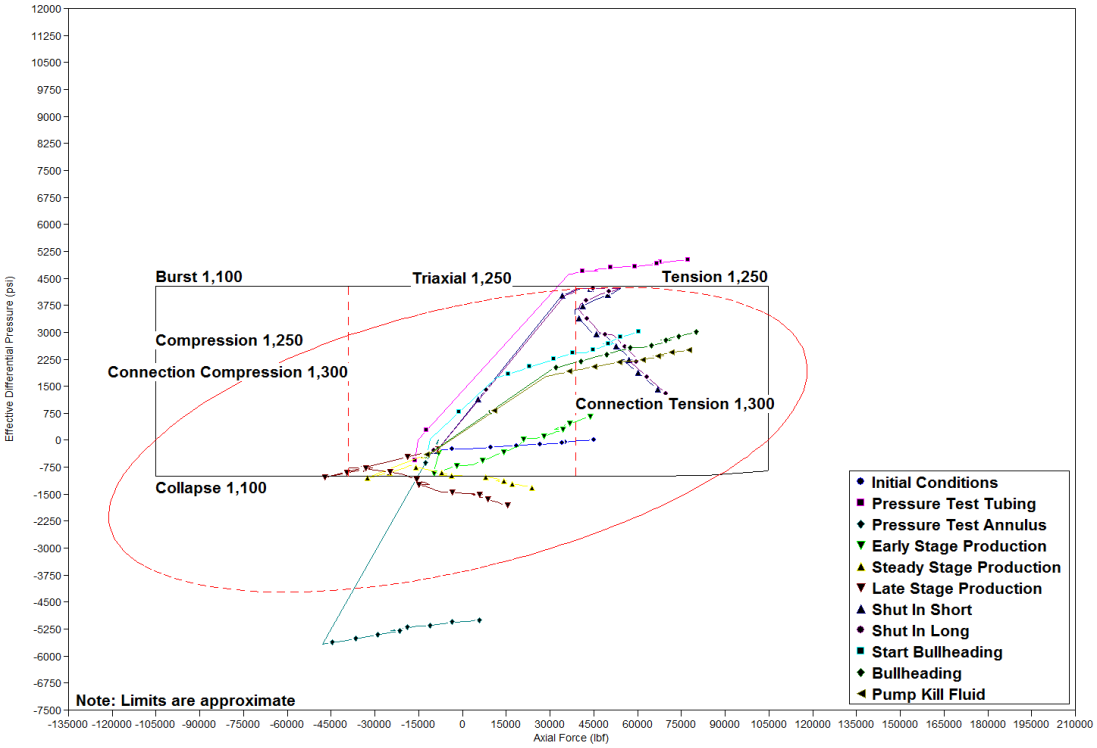

Figure 44: Design limits for various loads for tubing with 50% wear depth

4.3 PROSPER Simulation

PROSPER is part of the Integrated Production Modeling (IPM) software developed by Petroleum Experts (Petex) that is used to build reliable well models to design tubing. It can also model some artificial lift methods such as gas lift (continuous and intermittent), ESP, and SRP. In this case, PROSPER will be used to design a gas lift model as one of the load cases for the tubing.

The WELLCAT simulation shows that as the tubing damage due to corrosion is more severe, the Von-Mises design limits are narrower, resulting in less tubing strength. During production, the reservoir pressure will be depleted and the production will decrease. Hence, an artificial lift installation is needed to lower the bottom hole pressure to optimize well production. When tubing is de-rated, it is necessary to re-design the artificial lift with respect to new material strength after the damaged occurs. The WELLCAT simulation shows that gas lift loading first exceeds the Von Mises envelope when tubing wear depth is 40% as shown in Figure 43.

In this section, gas lift design for the unworn tubing and tubing with 40% wear depth will be performed. The main objective of this simulation is to show that the gas lift design for the unworn tubing cannot be applied if the tubing is de-rated and its material strength has changed. Hence, one needs to re-design the gas lift based on the new material strength after the thickness of tubing has been reduced due to corrosion.

4.3.1 Assumptions

For the gas lift simulation, the following assumptions are made:

- The reservoir has been depleted with reservoir pressure drop of 800 psi. Initial reservoir pressure (Pi) is 5400 psi while current reservoir pressure (Pr) is defined as 4600 psi. During the life of the production, until the reservoir is depleted, the tubing is attacked by corrosion, which causes tubing damage with 40% of wall thickness wear depth.
- Gas lift is an artificial lift method that will be set.

4.3.2 Working Procedure for Gas Lift Model

The general workflow to design the artificial lift in PROSPER is shown in Figure 45.

4.3.3 System Summary

The system summary consists of general well information to establish the model as shown in Figure 46.

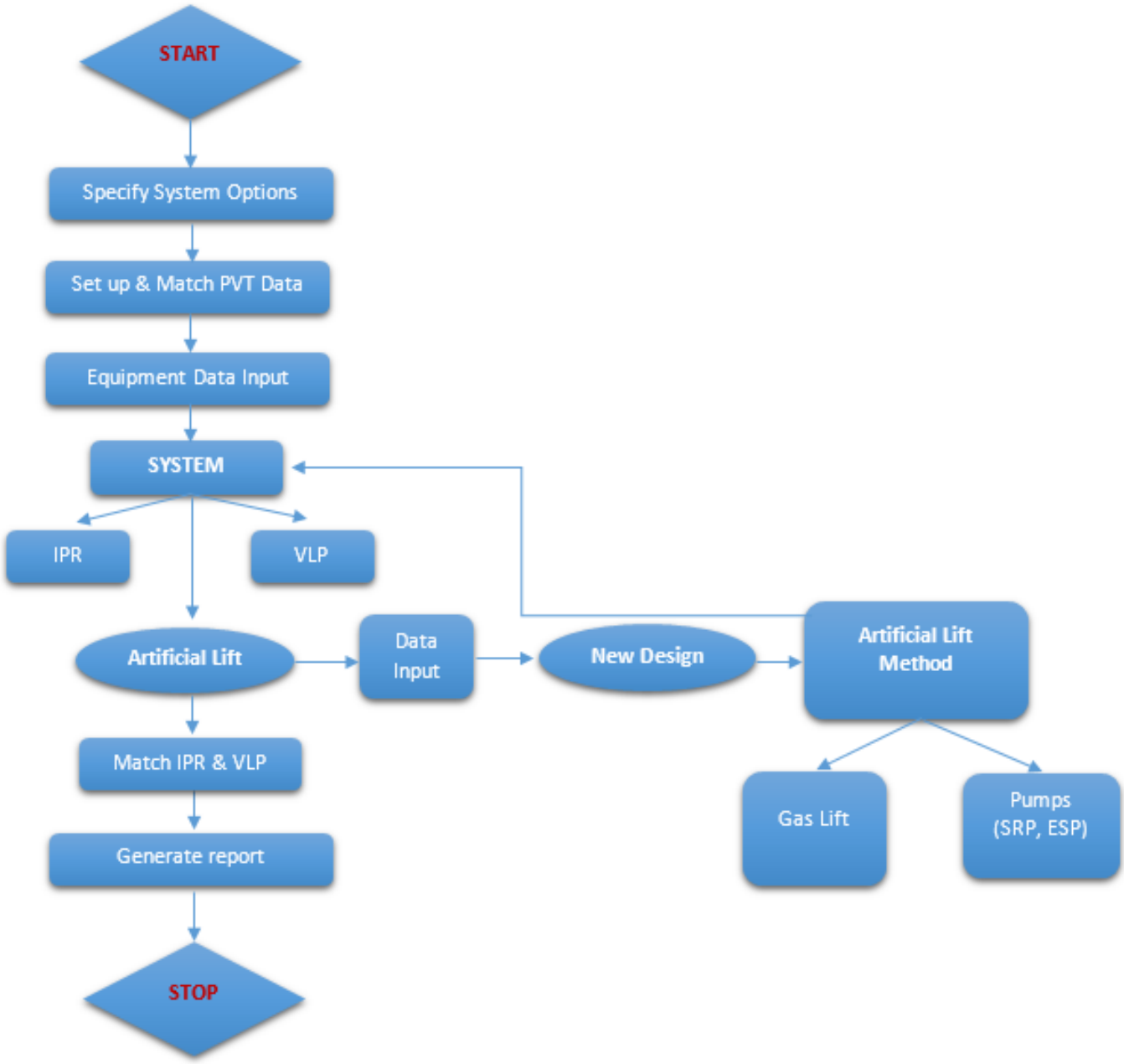

Figure 45: Artificial lift design workflow in PROSPER

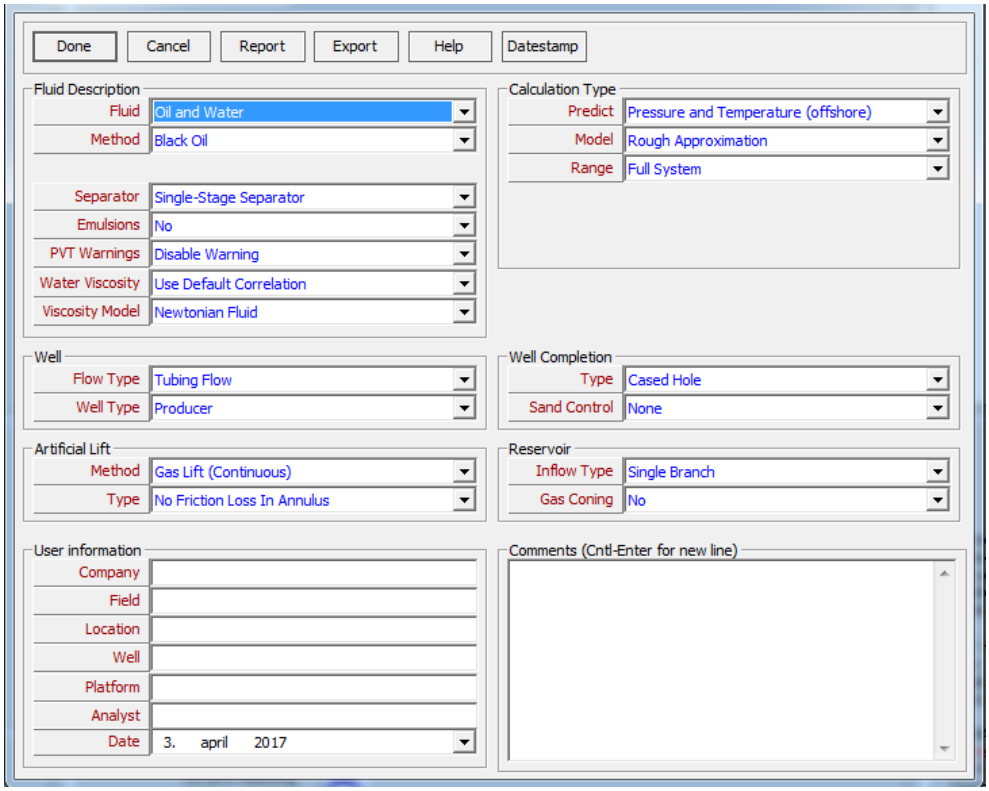

Figure 46: PROSPER system summary

4.3.4 PVT Data

In order to get an appropriate gas lift design, an accurate PVT data shall be obtained and the calculation from the PVT correlation will be matched to measured laboratory data. Figure 47 shows the data input for fluid PVT.

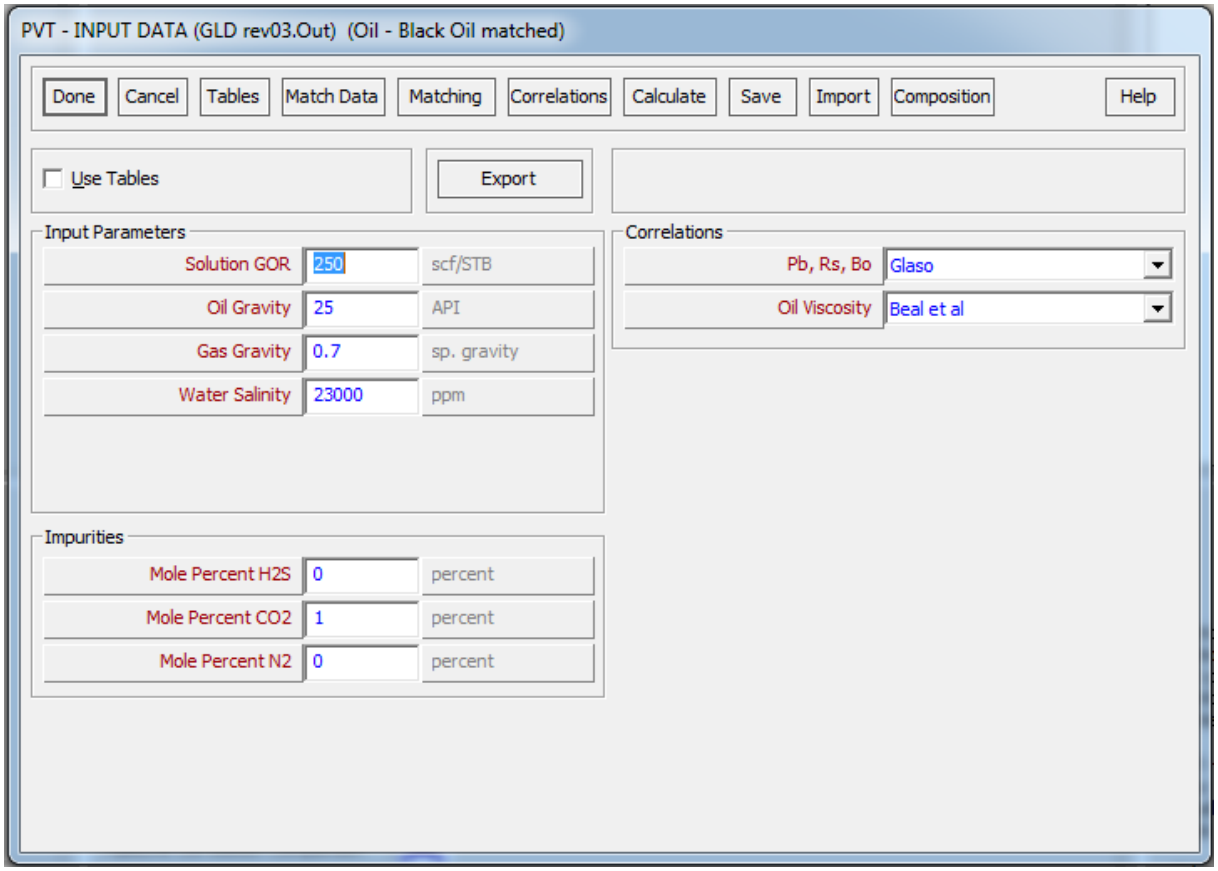

Figure 47: PVT data input

In order to match the calculation from the PVT correlation to the laboratory data, a non-linear regression method has been used. Figure 48 shows the PVT properties used as match variables, such as:

- Bubble point (P_b)
- Gas Oil Ratio (GOR)
- Oil Formation Volume Factor (FVF)
- Oil viscosity

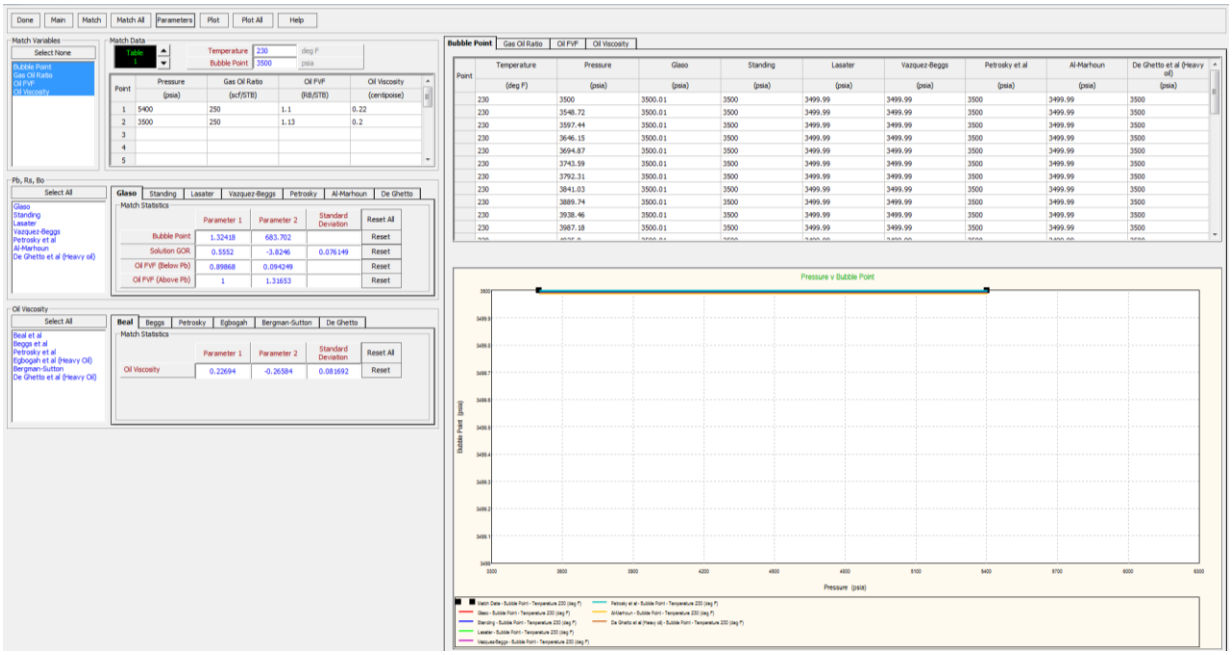

Figure 48: PVT matching

To have a well-fitted simulation to the laboratory data, non-linear regression is performed by PROSPER to adjust the PVT correlations by applying a multiplier (parameter 1) and a shift (parameter 2). Figure 49 shows how PROSPER matches the data. To have the best fit, parameter 1 should be close to one while parameter 2 should be close to zero. A standard deviation approaching zero indicates that the data points tend to be close to the mean. Hence, the smaller the standard deviation, the better the non-linear regression is.

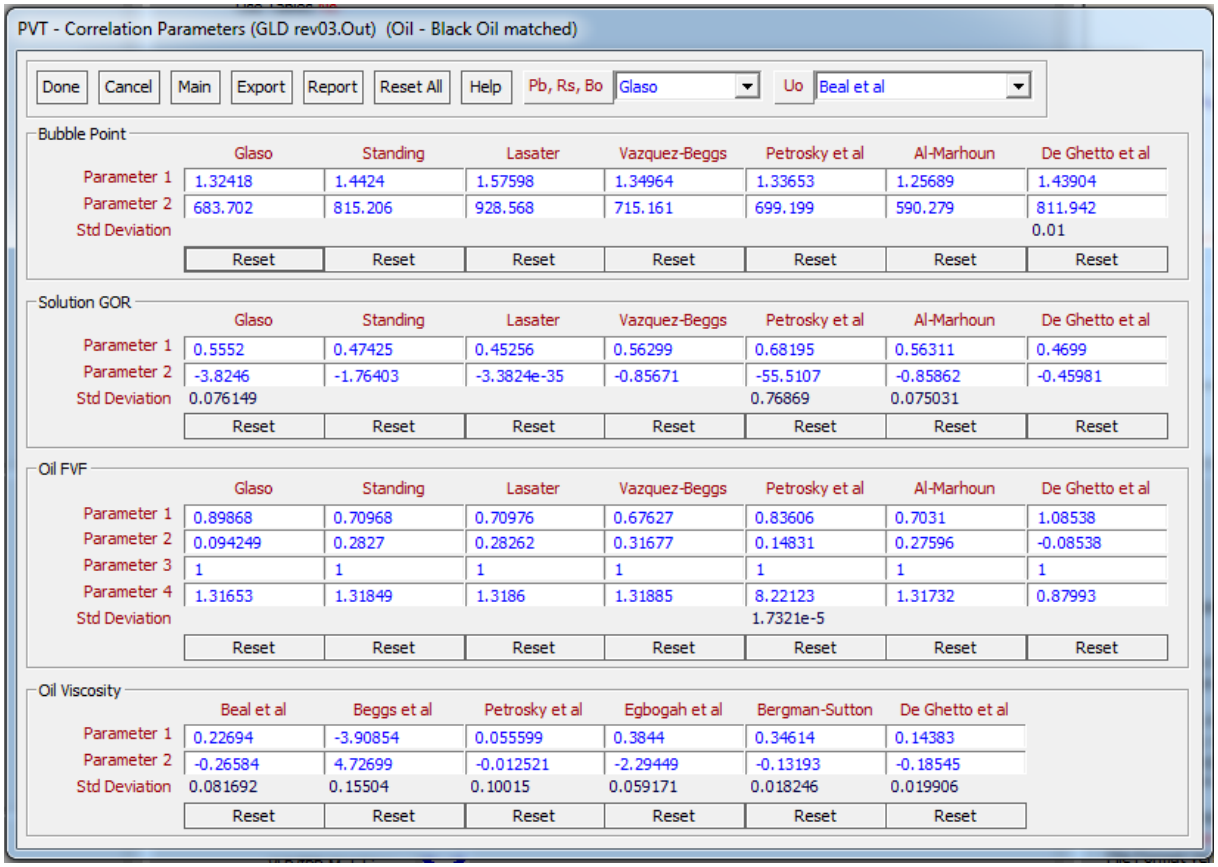

Figure 49: PVT correlation parameters

4.3.5 Equipment Data

The equipment data used in PROSPER are the same as in WELLCAT and consist of five sections:

1. Deviation survey

   The deviation survey data used are the same as WELLCAT.

2. Surface equipment

   In this case, since the gas lift design is only limited to downhole equipment and no surface facility is applied, this section's data are not used.

3. Downhole equipment

   The downhole equipment data used are the same as WELLCAT.

4. Geothermal gradients

   The geothermal gradients data used are the same as WELLCAT.

5. Average heat capacities

In this case, the default values of average heat capacities data from PROSPER are used as shown in Figure 50.

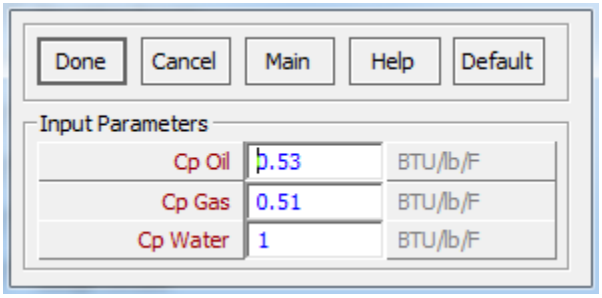

Figure 50: Average heat capacities

4.3.6 Artificial Lift Design for Unworn Tubing

Inflow Performance Relationship (IPR) and Vertical Lift Performance (VLP) data

The reservoir and fluids data used for this simulation are the same as the data input in WELLCAT with some additional artificial data. A Darcy model is used to calculate IPR and Petroleum Expert 2 correlation is used to approximate VLP. The data input is shown in Table 14.

Table 14: Data input for IPR and VLP

Data	Value	Unit
Reservoir permeability (k)	40	md
Reservoir thickness (h)	30	ft
Drainage area (A)	100	acres
Dietz shape factor	31.6	
Wellbore radius (r_w)	0.354	ft
Mechanical skin (S)	3	
Top node pressure	1000	psi

The IPR curve expresses the reservoir's capability to deliver the fluids. The maximum liquid production is achieved when the bottom hole pressure approaches zero. In this case, the maximum liquid rate is 17,301 STB/day as shown by the IPR curve (red line) in Figure 51.

Economides [46] stated that VLP represents how the rate of the fluid flows from the bottom hole to the surface will be affected by the drop in tubing pressure. In this case, the VLP curve is shown as the blue line in Figure 51, and the intersection of the IPR and VLP curves defines the flow rate produced by the well. In this case, since the IPR curve does not intersect the VLP curve, it indicates that the well does not flow and an artificial lift is needed.

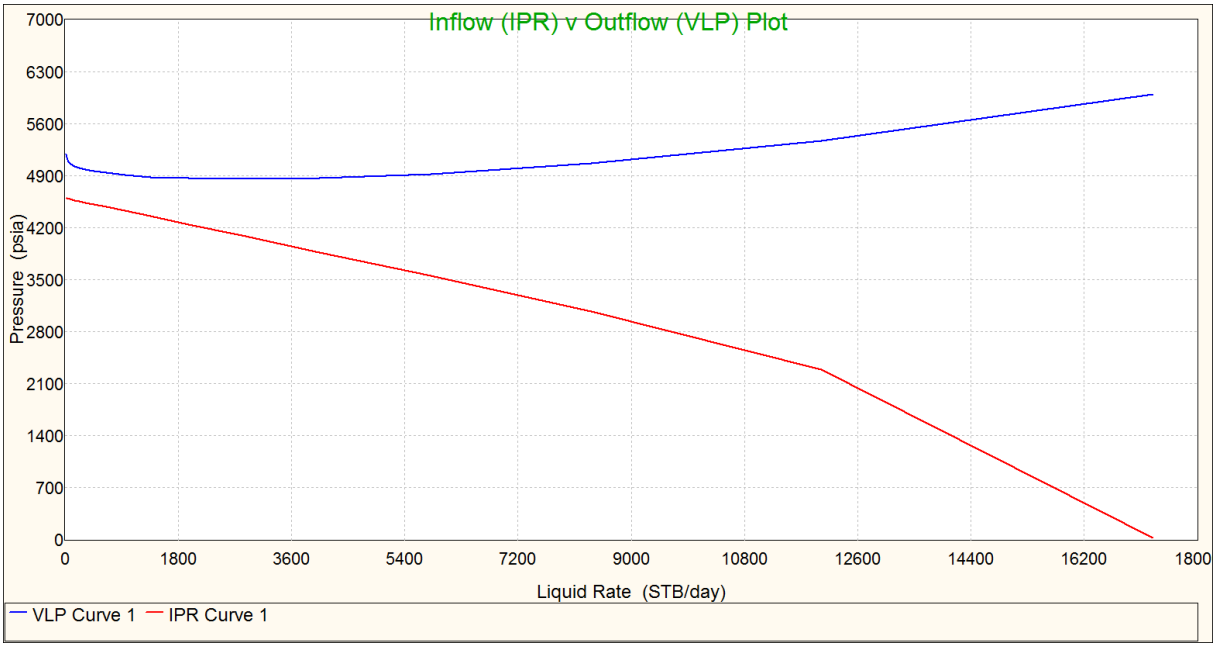

Figure 51: System (IPR vs. VLP) curve

Gas Lift Design (GLD)

In unworn tubing, the operating injection pressure in GLD is set to be 3500 psi. Based on the WELLCAT simulation, this pressure is within te Von-Mises envelope. The GLD data are shown in Figure 52.

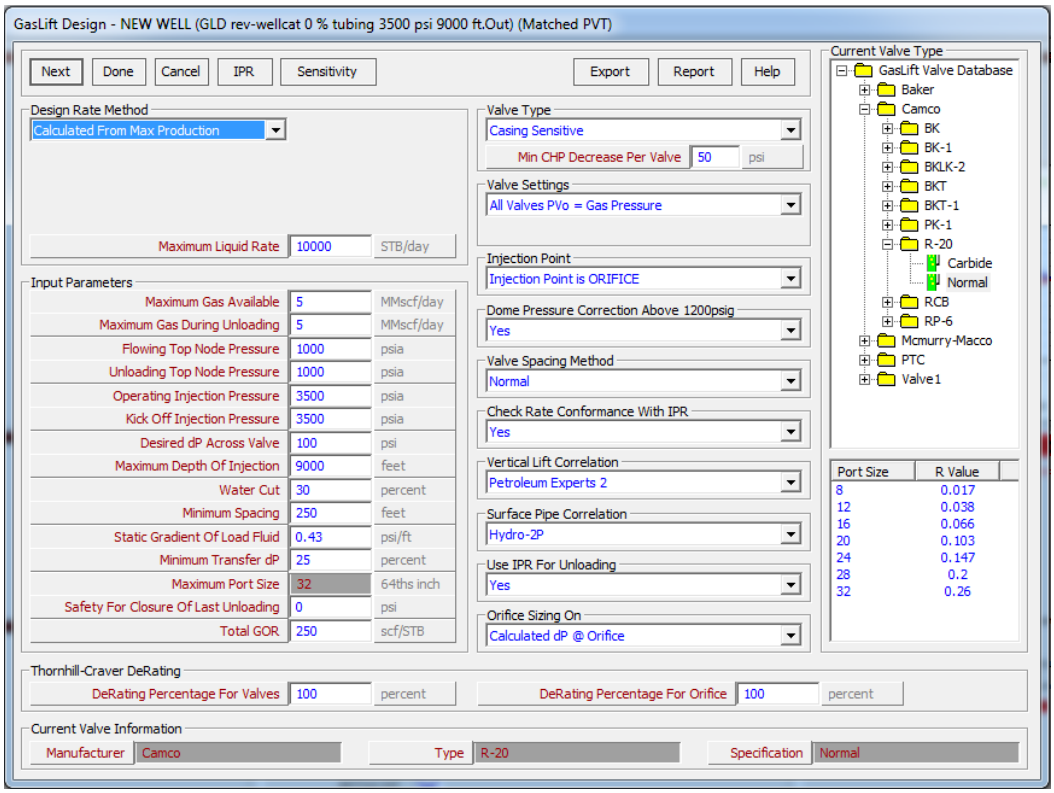

Figure 52: Gas lift design data for unworn tubing

The GLD result in Figure 53 shows that two valves are needed. The deepest valve (operating valve) is set at 9000 ft MD with the optimum gas injection rate is 4.916 MMscfd. The GLD report is summarized in Table 15.

Table 15: Gas lift design report for unworn tubing

Gas Lift Design Report			
Parameter		**Value**	**Unit**
Valve type		Casing sensitive	
Min CHP decrease per valve		50	psi
Design rate method		Calculated from maximum P	
Design oil rate		3625.6	STB/day
Injection point		Orifice	
Orifice sizing method		Calculated dP at orifice	
Valve manufacturer		Camco	
Valve type		R-20	
Valve specification		Normal	
Maximum gas available		5	MMscf/day
Maximum gas during unloading		5	MMscf/day
Flowing top node pressure		1000	psi
Unloading top node pressure		1000	psi
Operating injection pressure		3500	psi
Kick-off injection pressure		3500	psi
Desired dP across valve		100	psi
Maximum depth of injection		9000	ft
Water cut		30	%
Minimum spacing		250	ft
State gradient of load fluid		0.43	psi/ft
Maximum port size		32	64ths inch
Total GOR		250	scf/STB
Actual liquid rate		5179	STB/day
Actual oil rate		3626	STB/day
Actual gas injection rate		4.916	MMscf/day
Actual injection pressure		3394	psi
Valve depth	Valve 1	8540	ft MD
	Valve 2 (operating valve)	9000	ft MD

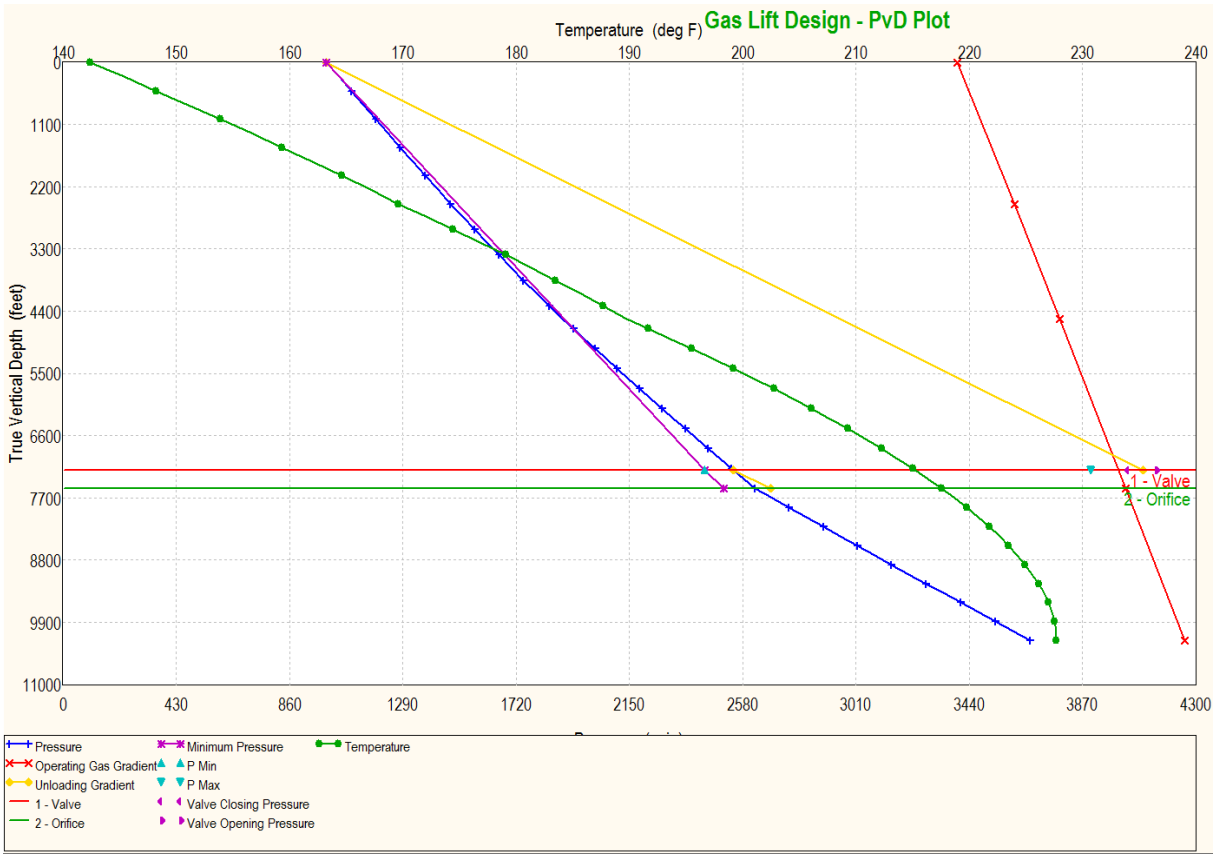

Figure 53: Gas lift valve design for unworn tubing

Figure 54 presents the new system (IPR vs. VLP) curve after the gas lift is installed. The gas lift is designed to modify the flowing system so that the fluid can flow to the surface with a given bottom hole pressure. In this case, the optimum fluid rate is 5196 STB/day where the VLP intersects the IPR.

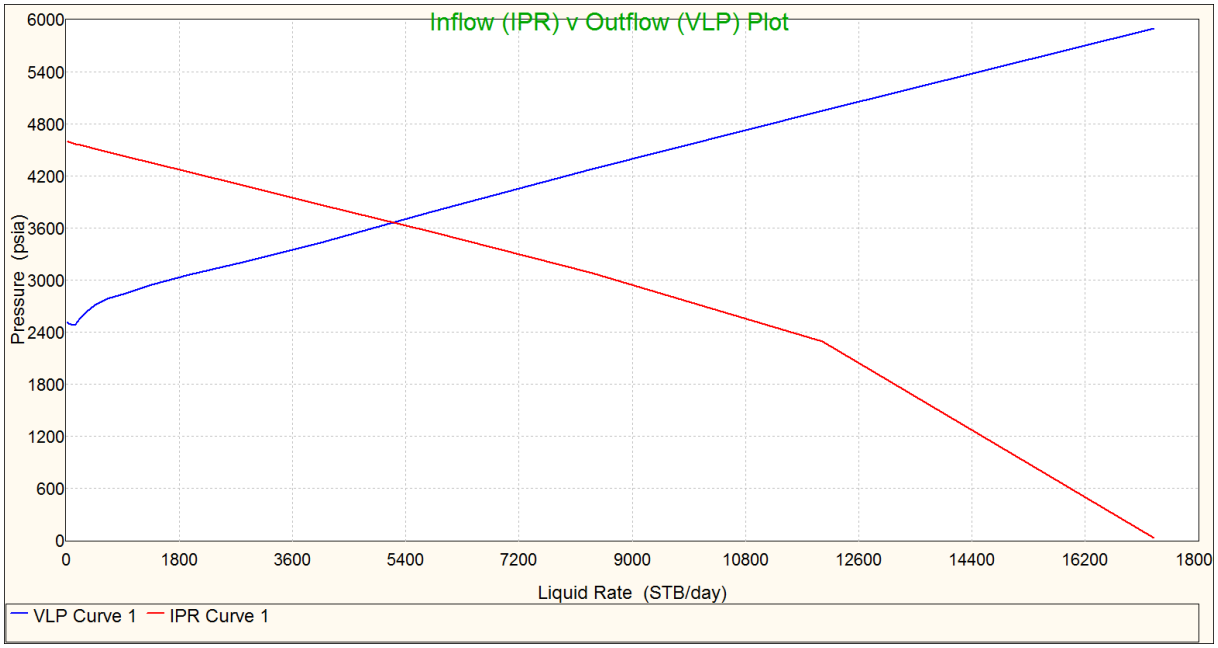

Figure 54: System (IPR vs. VLP) after gas lift installation

4.3.7 Artificial Lift Design for Tubing With 40% Wear Depth

Based on the WELLCAT simulation for tubing with 40% wear depth in Figure 43, the gas lift loads set in unworn tubing exceed the Von-Mises envelope and cannot be applied to this damaged tubing. Hence, it is necessary to re-design the gas lift based on the new material strength after the tubing is de-rated. In this case, the gas lift injection pressure is reduced and set to 3000 psi to overcome the material strength reduction. The gas injection rate is lowered to 4 MMSCF/day and the check valve is set at 8000 ft to compensate for the lower injection pressure.

Inflow Performance Relationship (IPR) and Vertical Lift Performance (VLP) Data

The absence of intersection between the VLP and the IPR curves in Figure 55 indicates that in this damaged tubing, the fluid cannot flow to the surface and an artificial lift installation is needed.

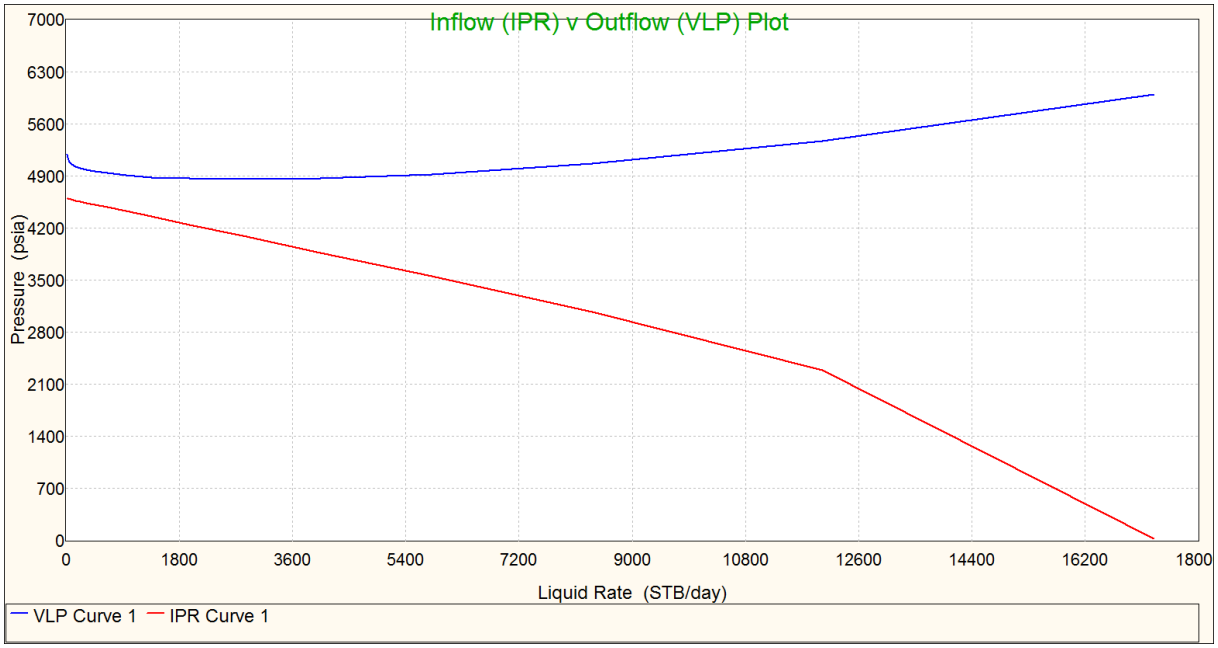

Figure 55: System (IPR vs. VLP) before gas lift installation

Gas Lift Design

In this case, the gas lift injection pressure is set to be 3000 psi and the maximum valve depth is reduced to 8000 ft MD. As shown in Table 16, the gas lift valve depth is shallower since the lower injection pressure is applied. In some cases, the lower injection pressure requires that more gas valves be set. The valve depth design is summarized in Figure 56. The change of gas lift design also affects the forecast of the produced liquid rate. In unworn tubing, the liquid rate is predicted to be 5179 STB/day, but after the new GLD is applied in tubing with 40% wear depth, the liquid rate decreases to 4845 STB/day as shown in Figure 57.

Table 16: GLD report for tubing with 40 % wear depth

Gas Lift Design Report			
Parameter		**Value**	**Unit**
Valve type		Casing sensitive	
Min CHP decrease per valve		50	psi
Design rate method		Calculated from maximum P	
Design oil rate		3392	STB/day
Injection point		Orifice	
Orifice sizing method		Calculated dP at orifice	
Valve manufacturer		Camco	
Valve type		R-20	
Valve specification		Normal	
Maximum gas available		4	MMscf/day
Maximum gas during unloading		4	MMscf/day
Flowing top node pressure		1000	psi
Unloading top node pressure		1000	psi
Operating injection pressure		3000	psi
Kick-off injection pressure		3000	psi
Desired dP across valve		100	psi
Maximum depth of injection		8000	ft
Water cut		30	%
Minimum spacing		250	ft
State gradient of load fluid		0.43	psi/ft
Maximum port size		32	64ths inch
Total GOR		250	scf/STB
Actual liquid rate		4845	STB/day
Actual oil rate		3392	STB/day
Actual gas injection rate		3.9	MMscf/day
Actual injection pressure		2950	psi
Valve depth	Valve 1	6256	ft MD
	Valve 2 (operating valve)	8000	ft MD

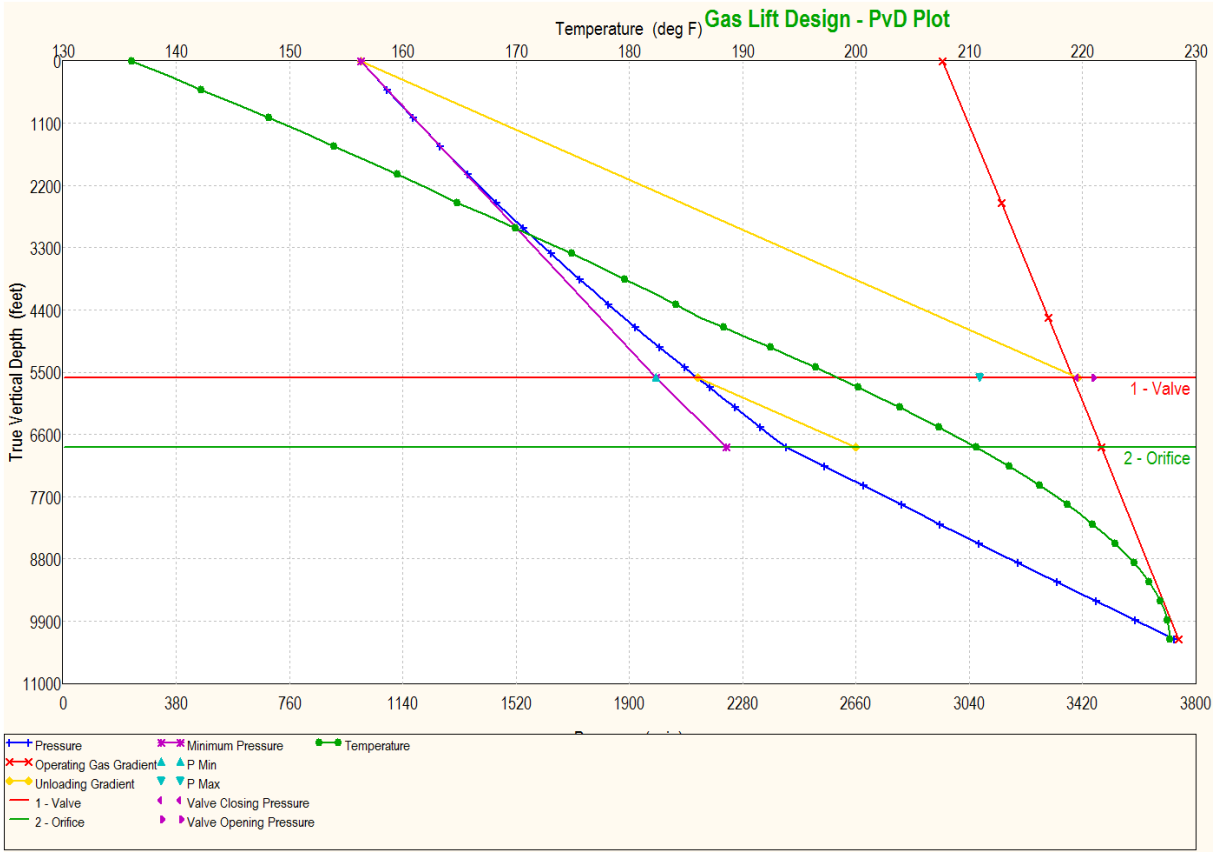

Figure 56: Gas lift valve design for tubing with 50% wear depth

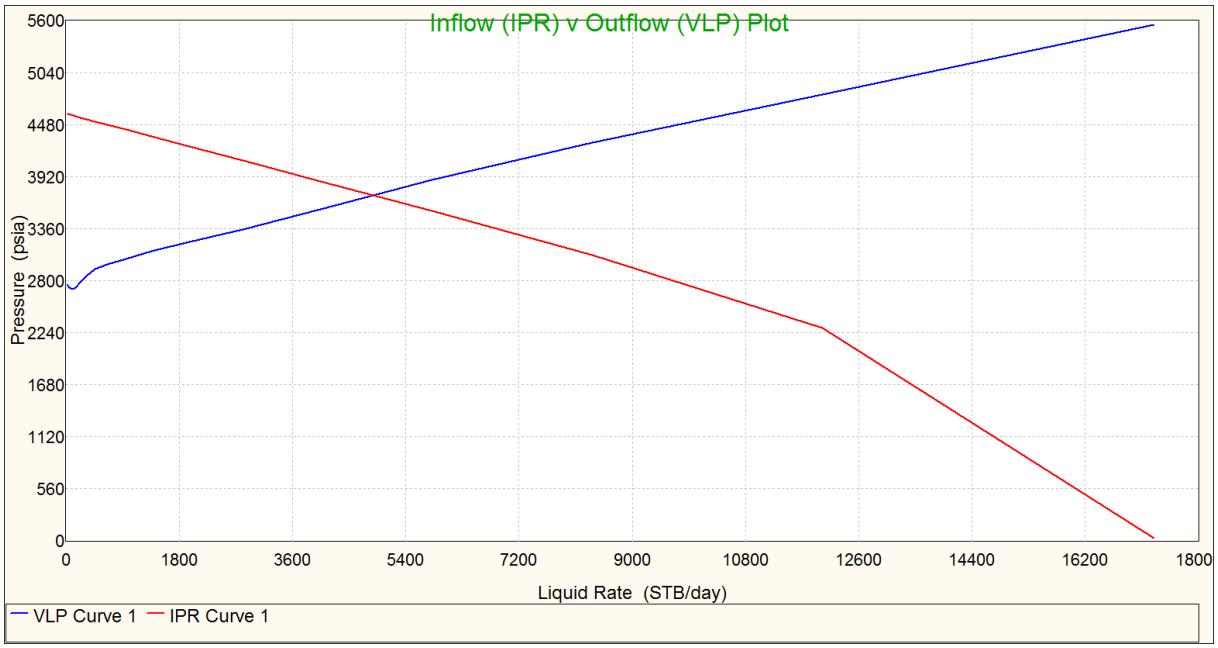

Figure 57: System (IPR vs. VLP) curves for new GLD

The new gas lift load is applied in WELLCAT to check if these loads are within the Von-Mises envelope and will not cause tubing failure. Figure 58 and Figure 59 show the comparison of design limits between the previous GLD and the new one. The WELLCAT simulation proves that the newer gas lift design is safe for tubing with 40% wear depth.

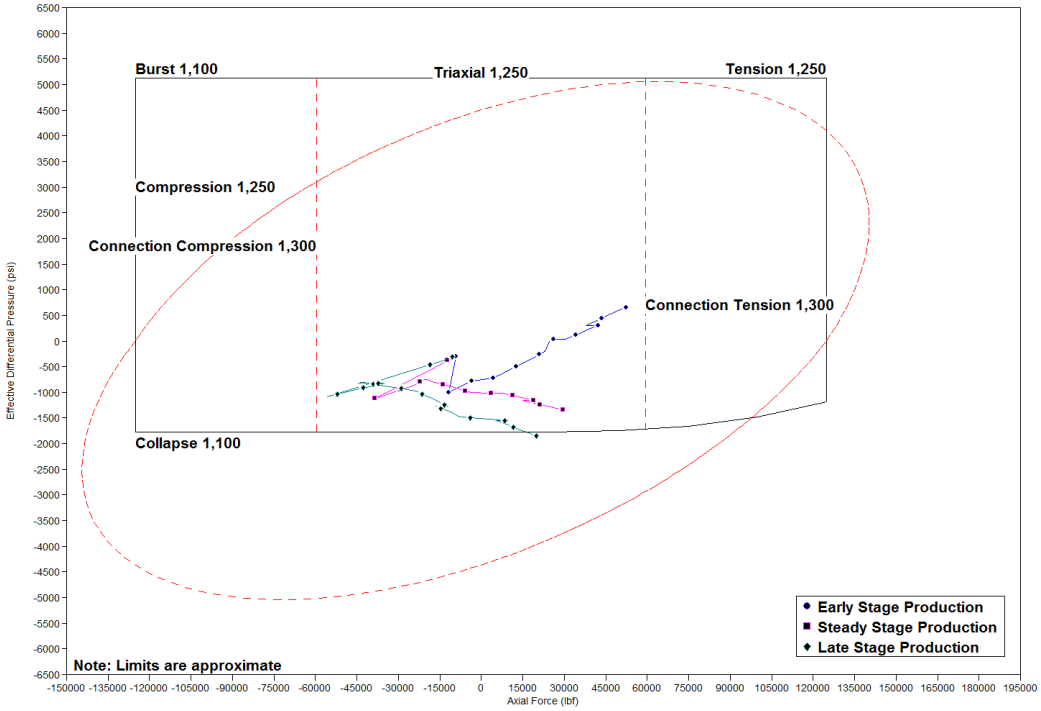

Figure 58: Design limits for gas lift loads before re-design

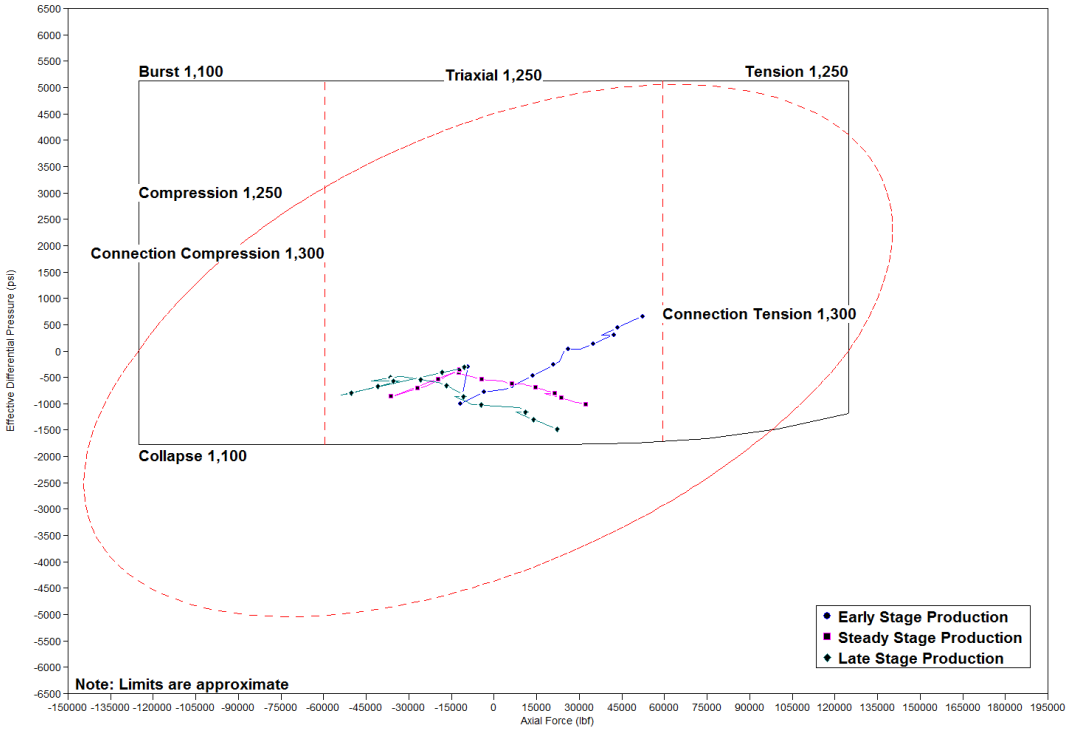

Figure 59: Design limits for gas lift loads after re-design

4.4 Finite Element Method (FEM) for Damaged Tubular Modeling

Abaqus CAE is a commercial finite element analysis tool used to simulate a wide range of engineering problems and visualize the results of FEM analysis. In this thesis, the production tubing will be simulated in different inner diameters and damage shapes as a result of thickness deration due to uniform corrosion and pitting corrosion. A simple pipeline solid model has been created and the loading scenarios will be applied to simulate real production loadings and their effects on tubing stress distribution. The procedure of FEM modeling in Abaqus CAE is shown in Figure 60.

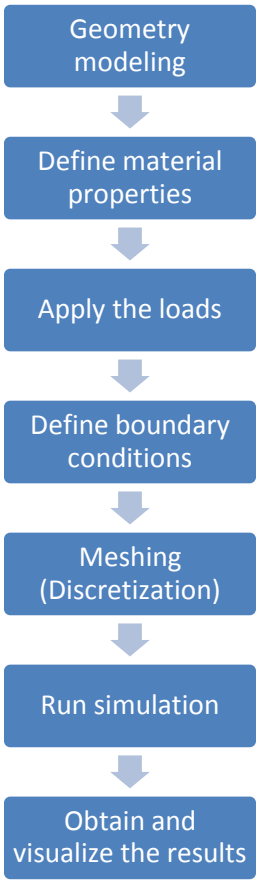

Figure 60 FEM modeling steps in Abaqus CAE

4.4.1 Data Input

In this FEM simulation study, a simple tubing model has been built and the fluids data have been defined based on the WELLCAT data as shown in Table 17 and Table 18. The effect of uniform corrosion is described as thickness reduction on the tubing. Tubing is de-rated uniformly from 5 – 50%, meaning that the longer it is exposed to corrosion, the more the thickness is reduced as shown in the WELLCAT input data (see Table 10).

Table 17: Well and fluids data

Well and Fluids Data		
Properties	**Unit**	**Values**
Ppore @ 10,000 ft TVD	psi	5400
DLS @ max penetration	deg	2
TVD @ max DLS	ft	4527.7
Pi @ max DLS	psi	3758
Completion Fluid Density (NaCl)	SG	1.05
	ppg	8.76
Fluid gradient inside tubing	psi/ft	0.3

Table 18: T-95 Tubing data

T-95 Tubing Data		
Properties	**Unit**	**Values**
Grade	N/A	T-95
Inner Diameter	in	4.000
Outer Diameter	in	3.548
Thickness	in	0.226
Weight	ppf	9.5
Yield Strength	psi	95,000
Burst Pressure (Barlow)	psi	9393
Collapse Pressure (API)	psi	7306

4.4.2 Geometry Modeling

Geometry modeling is an important step in building a FEM. In this simulation study, the pipe is modeled based on the real tubing used in WELLCAT as shown in Figure 61. T-95 tubing with OD 4.000 inch and ID 3.548 inch is used as the base case. The damage caused by uniform corrosion that affects thickness reduction of the tubing will be simulated in separate models for different inner diameters (5 – 50% wear). Abaqus CAE uses X-Y-Z in the global coordinate system. The geometry modeling starts with creating an isolated point as the point of origin (0, 0). The outer and inner diameters are defined by creating a circle in the X-Y plane relative to the point of origin coordinate. The length of the pipe will be set afterward.

For the pitting corrosion cases, the damage due to localized pitting is modeled as surface indentations spread in the inner pipe. The depth of indentation is defined as 10 – 50% of tubing wear and the geometry is set the same for ease of computation.

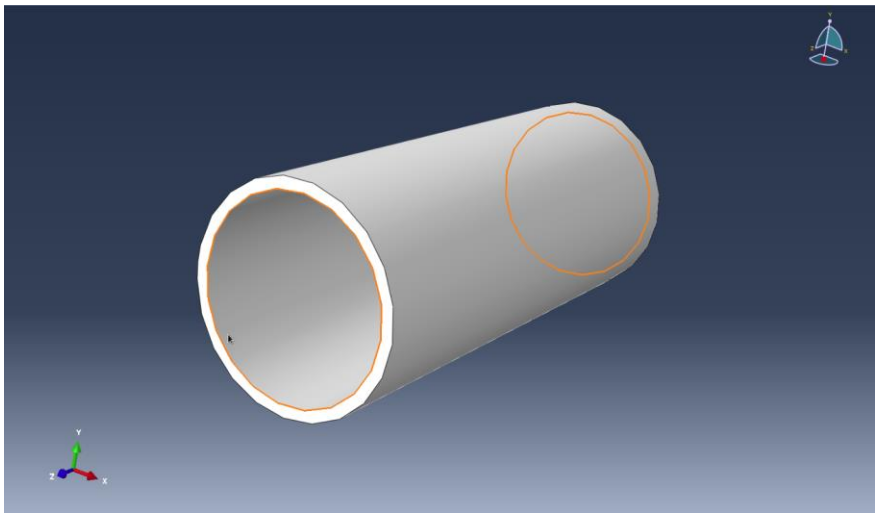

Figure 61: Tubing geometry

4.4.3 Material Properties

In this model, an elastic material type is used. Its mechanical properties are set such as Young's Modulus and Poisson's Ratio. These properties represent material behavior in the elastic region. One can obtain the engineering quantities from a tension test that provides important material properties for use in structural design. In this case, the data used are the common values for steel as shown in Table 19.

Table 19: Mechanical properties of solid elastic materials

Material behavior	Elastic, Isotropic
Young's Modulus	30 x 10^6 psi
Poisson's Ratio	0.25

4.4.4 Boundary Conditions

The purpose of applying boundary conditions is to define the constraint. Since there is no axial stress applied to the pipe, the boundary conditions are defined to be free ends as shown in Figure 62.

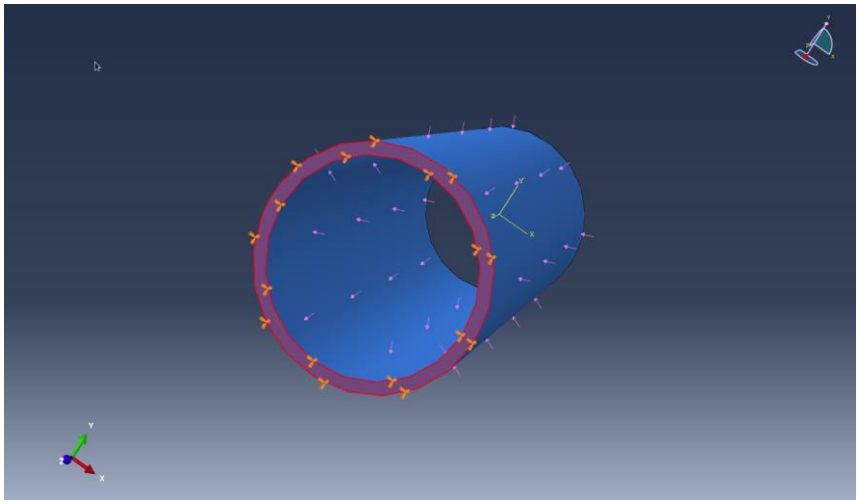

Figure 62: Boundary conditions

4.4.5 Loading

The pressure loads on the pipe are applied only on the outer and inner pipe since there are no axial compressive loads. The loading cases are defined based on the real condition of the tubing in a well. The inner pressure is set as the pressure of fluids inside the well, while outer pressure is set as the pressure of fluids (completion fluids) in the annulus as shown in Figure 63.

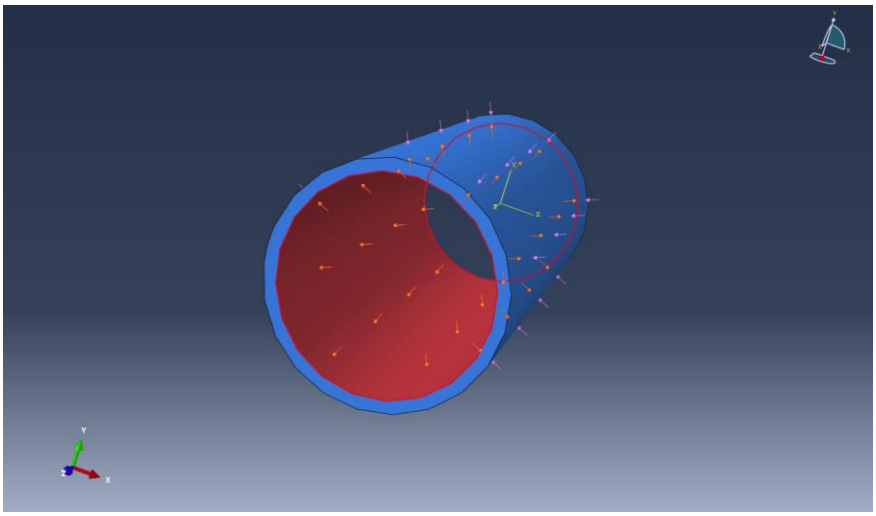

Figure 63: Pressure loadings

4.4.6 Meshing

Meshing is a process of dividing the whole geometry into small finer elements so that when the load is applied, it will be distributed uniformly throughout the elements. Creating a clean and uniform mesh can be an advantage for structural modeling since good shape metrics on every finite element will improve the meshing algorithms. The first step of meshing is to divide the geometry into shapes and choose the appropriate algorithm. The element shape used in this model is hexahedral with a medial axis as its algorithm as shown in Figure 64. The meshing has proven to be good enough since it gives an acceptable level of accuracy when comparing the results to the theoretical data.

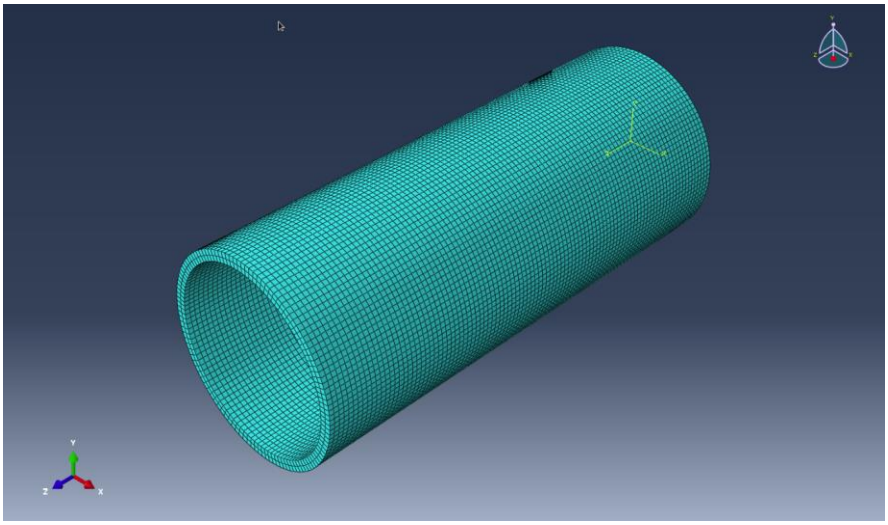

Figure 64: Meshing

4.4.7 FEM Simulation Results and Analysis

The main objective of this FEM simulation is to study the effects of the damage due to uniform and pitting corrosion on the production tubing and compare the results with the standard theoretical equations used to calculate the strength of the tubing in terms of burst and collapse rating. The application of theoretical API equations to the de-rated tubing due to uniform thickness reduction and localized pitting damage will also be investigated.

4.4.7.1 Simulation Cases

The most important mechanical properties of the production tubing are burst and collapse ratings, which represent the strength of the tubing. By the time of production, the strength of the tubing will decrease as the wear depth increases due to corrosion damage in the tubing. This deterioration shall be taken into account when the well is subjected to some production and workover loadings such as stimulation jobs, bullheading, gas lift, and so forth. It is important to determine the real burst and collapse strengths that can withstand the loadings after the tubing is de-rated to prevent tubing failures.

The two main simulation cases have been built to study Von-Mises stress distributions and real tubing strengths after damage has occurred uniformly and locally. T-95 tubing with OD 4.000

inch, ID 3.548 inch, and 9.5 ppf will be used as the base case. The burst rating is calculated from Barlow equation, while the collapse strength is calculated from the API collapse equation. The loadings applied on both the inner and outer pipe are taken from the pressure at the depth where the dogleg severity is at maximum since it has been shown from some real-world cases that the greatest damage occurs in the deviated hole section. As shown in Figure 4 in Chapter 1, the recorded damage from caliper tools in a ConocoPhillips well [6] is most severe at the depth of 1626 ft, where the deviation is at maximum.

The inner loading is defined as the pressure inside the tubing due to the hydrostatic fluids in a static well or the well pressure due to well service and production enhancement activities such as acid and matrix stimulation, fracturing, bullheading, and so forth. The outer loading is defined as the pressure in the annulus due to the hydrostatic column of completion fluids or production activities which apply pressure through the annulus such as kick off in gas lift installation, tubing leakages, and so on.

4.4.7.2 Uniform Corrosion Cases

In uniform corrosion, the wear depth is distributed consistently in the inner tubing as the corrosion attack takes place over the entire tubing surface. The model is built based on the real geometry of the tubing, and the wall thickness is reduced uniformly as shown in Figure 65. The tubing will be simulated from 5 – 50% wear, as the corrosion attacks will be more severe as the production goes on. As shown in Table 20, there are two types of cylinders after the tubing is de-rated: thick-walled and thin-walled. A comparison of stress distribution between thin-walled and thick-walled cylinders after applying the loads will also be conducted as part of this study.

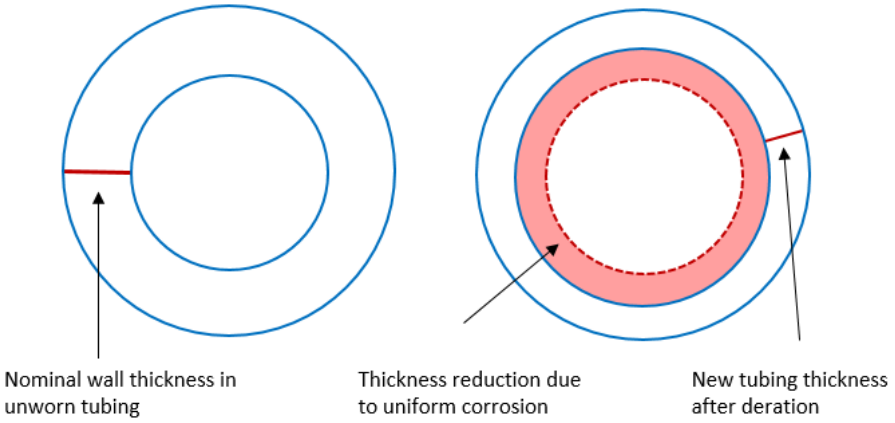

Figure 65: Tubing geometry for uniform corrosion (A) Before deration (B) After deration

Table 20: T-95 Tubing data after de-ration due to uniform corrosion

T-95 Tubing Data after De-ration					
Wear (%)	**Weight (ppf)**	**OD (in)**	**ID (in)**	**Thickness (in)**	**Cylinder Types**
5	9.05	4.000	3.571	0.215	Thick-walled
10	8.60	4.000	3.593	0.203	Thick-walled
15	8.15	4.000	3.616	0.192	Thick-walled
20	7.69	4.000	3.638	0.181	Thin-walled
25	7.23	4.000	3.661	0.170	Thin-walled
30	6.77	4.000	3.684	0.158	Thin-walled
35	6.30	4.000	3.706	0.147	Thin-walled
40	5.84	4.000	3.729	0.136	Thin-walled
45	5.37	4.000	3.751	0.124	Thin-walled
50	4.89	4.000	3.774	0.113	Thin-walled

4.4.7.2.1 Case 1 – Burst

Burst pressure is defined as the internal pressure that a pipe can withstand before it causes the material to yield. In this simulation study, the burst cases are developed based on real-world cases such as well stimulation and bullheading which forcibly apply pressure in the pipe into the formation. The inner pressure applied in Abaqus CAE will be varied to determine when the pipe yields and exceeds the yield strength of T-95 tubing (σ_y = 95,000 psi). The external pressure is defined as the annulus pressure exerted from completion fluid at the maximum deviation point (4525.7 ft TVD).

External pressure calculation:

$$P_o = 0.052 \times \rho fluids\ (ppg) \times depth\ (ft) \tag{4.6}$$

$$P_o = 0.052 \times 8.76\ ppg \times 4525.7\ ft = 2062\ psi$$

The two cases will be simulated for Po ≠ 0 and Po = 0 to study the application of theoretical burst equations in different conditions.

Abaqus CAE Simulation Results

The following two cases are presented based on the different outer pressure (**Po**) loading.

a. Case Po ≠ 0

The main objective of simulating with Abaqus CAE is to define the Von-Mises stress (σ_{VME}) based on FEM. For each wear depth, varied internal pressures are applied and the point where σ_{VME} intersects σ_y must be determined. The external pressure is set to be the completion fluid pressure in the annulus. For example, the stress distribution resulting from the simulation for a base case where tubing is unworn (0% wear depth) can be seen in Figure 66.

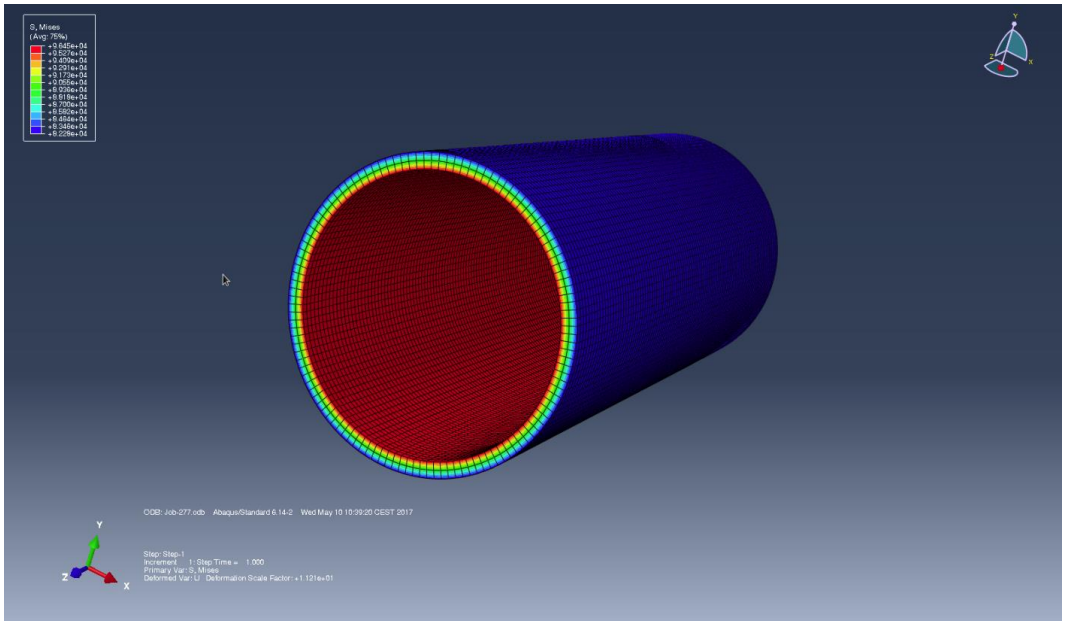

Figure 66: Stress distribution in unworn tubing for burst case (Po ≠ 0) – uniform corrosion

The red color shows the point where the tubing has the highest Von-Mises stress, and the blue color shows the lowest. After applying Pi = 12,000 psi, the simulation shows that σ_{VME} = 86,260 psi, which is still below σ_y = 95,000 psi. To get the intersection, the applied inner pressure should be higher. In this case, where Pi = 13,000 psi, the result shows that σ_{VME} = 95,030 psi. The other inner pressures can be applied to get the trend between σ_y and σ_{VME}, and the point when the Von-Mises stress intersects the material yield strength can be obtained by using interpolation. For 0% wear depth, the intersection point equals Pi = 12,997 psi, which excludes the safety factor at σ_y = 95,000 psi as shown in Table 21. The point where σ_y includes the safety factor (87.5%) is also obtained. With the $\sigma_{y(SF)}$ = 83,125 psi, the interpolation shows that σ_{VME} = 11,642 psi.

Table 21: Abaqus CAE simulation results for base case (unworn tubing)

External Pressure (psi)	Internal Pressure (psi)	Von Mises Stress (psi)
2062	5000	24940
2062	6000	33690
2062	7000	42440
2062	8000	51210
2062	9000	59970
2062	10000	68730
2062	11000	77500
2062	**11642**	**83125**
2062	12000	86260
2062	12500	90650
2062	12900	94150
2062	**12997**	**95000**
2062	13000	95030
2062	14000	103800
2062	15000	112600

The same steps are then implemented for the other wear depth. At 5% wear, the stress distribution is still uniform and there is no localized stress point as shown in Figure 67. The same trends also appear for wear depth 10 – 50%. The intersection point between σ_{VME} and σ_y equals 12,769 psi for σ_y without a safety factor and 11,443 psi for σ_y with a safety factor. The reduction of the burst strength is approximately 1.75%. For extremely higher wear (50%), σ_{VME} equals 7548 psi without a safety factor and the strength is reduced about 41.9%.

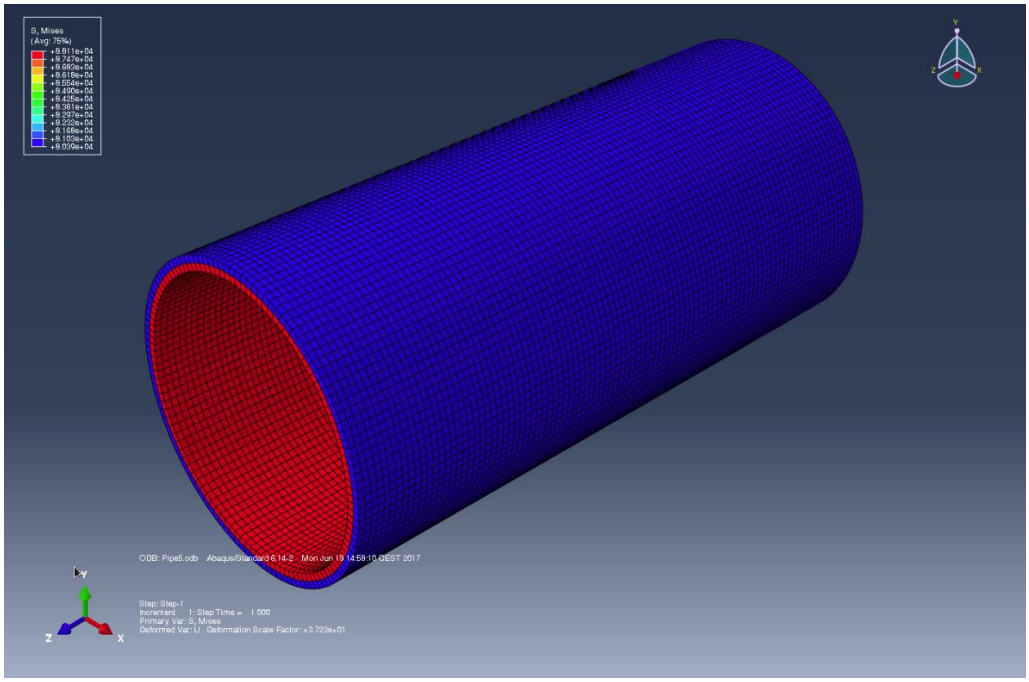

Figure 67: Stress distribution in tubing with 5% wear depth for burst case (Po ≠ 0) – uniform corrosion

Table 22: Abaqus CAE simulation results for 5% wear depth

External Pressure (psi)	Internal Pressure (psi)	Von Mises Stress (psi)
2062	5000	25740
2062	6000	34410
2062	7000	43360
2062	8000	52310
2062	9000	61260
2062	10000	70210
2062	11000	79160
2062	**11443**	**83125**
2062	12000	88110
2062	12500	92590
2062	12700	94380
2062	**12769**	**95000**
2062	12800	95280
2062	13000	97070
2062	14000	106000
2062	15000	115000

It is clearly shown that the higher the wear percentage, the lower the Von-Mises stress that causes the tubing to yield. This means that the deterioration of the tubing will cause its strength limit to decrease. This decrease must be considered when applying pressure for some field jobs to prevent tubing failures. This simulation will take into account the safety factor of 87.5% for yield strength. Hence, σ_y = 83,125 psi will be used throughout the simulation. The simulation results for all wear percentages are shown in Figure 68.

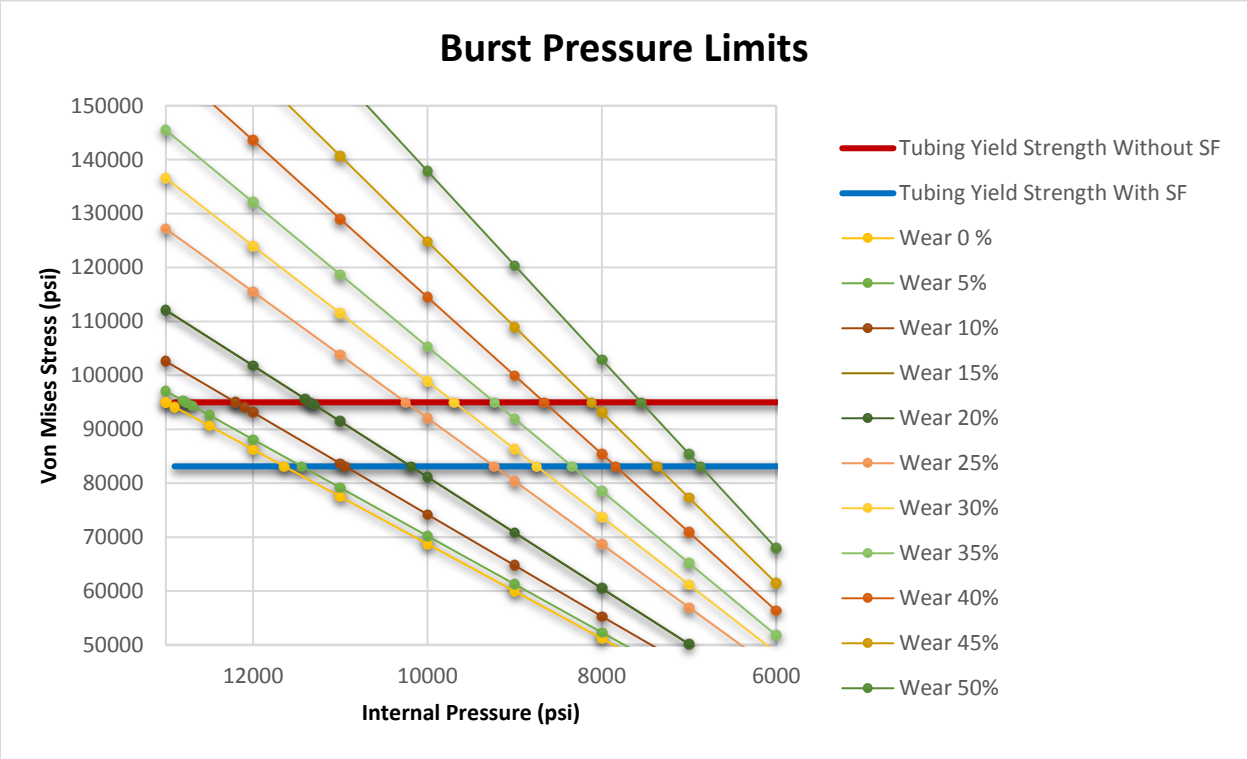

Figure 68: Burst pressure limits for 0-50% wear depth – Po ≠ 0

The figure shows that the slopes for each wear seem to be linear and parallel to each other. The intersection between σ_{VME} and σ_y can be obtained from the linear interpolation for each wear data point and is interpreted as the point where material starts to yield for the given wear percentages.

The linear interpolation equation is given as:

$$y = y_1 + (y_2 - y_1)\,\frac{x - x_1}{x_2 - x_1} \tag{4.7}$$

Table 23 shows the intersection points between σ_{VME} and σy for various wear depth.

Table 23: The intersection points between σ_{VME} and σy for 0 – 50% wear depth - Po ≠ 0

Wear (%)	Pressure from Abaqus CAE Simulation (psi)	
	σy = 95000 psi	σy = 83125 psi
0	12997	11642
5	12769	11443
10	12199	10943
15	11341	10191
20	10809	9726
25	10249	9234
30	9691	8746
35	9229	8342
40	8659	7842
45	8118	7368
50	7548	6869

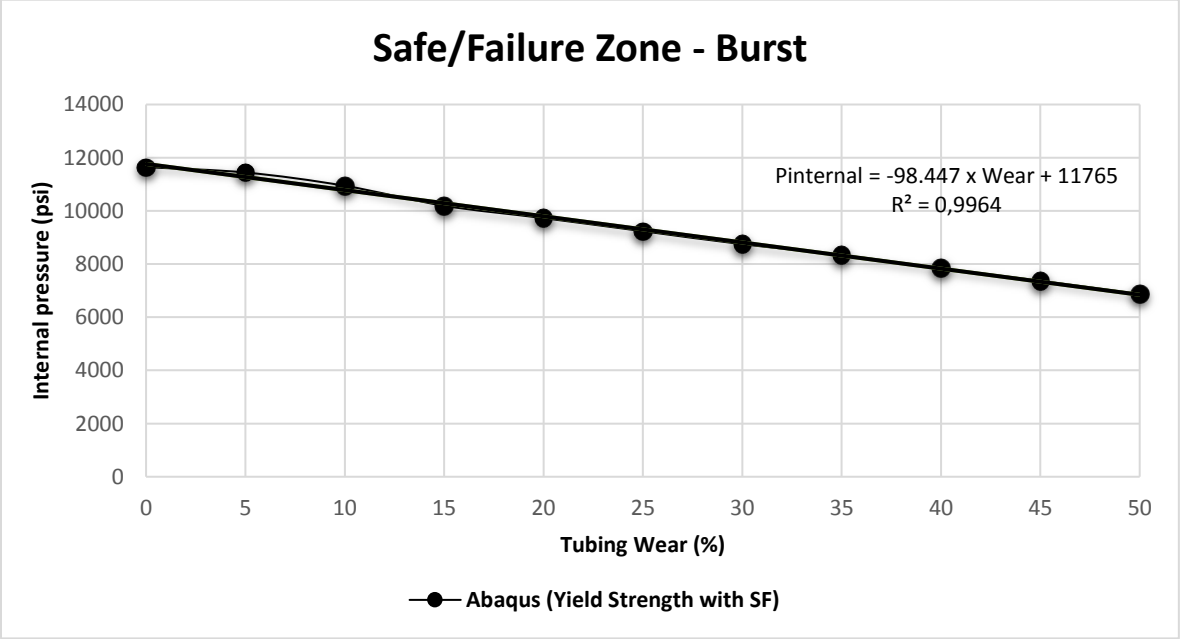

Figure 69: Safe/failure zone for varied internal pressure – Po ≠ 0

As shown in Figure 69, the pressure line set by all the intersection points will develop burst limits at different wear depth for a given tubing grade. From these simulation results, the burst pressure equation for the de-rated tubing can be developed as:

$$Pinternal = -98.447\ x\ Wear + 11765 \tag{4.8}$$

The linear regression gives a high value of R^2 = 0.9964 and almost approaches 1. The higher R^2 means the simulation data are closer to the fitted regression line. The trend of the slope is approaching straight line. This may mean that the thickness reduced uniformly around the tubing will give a linear reduction of burst strength. The zone below the line is the safe zone where the pressure acting on this area will not cause the tubing to yield, while the zone above the line is the failure zone where the pressure applied will cause tubing failures. It is important to note that when the tubing is de-rated, one cannot apply the pressure as high as when it is in an unworn condition because tubing failures can occur.

b. Case Po = 0

The same steps are applied as in the previous case, but the external pressure is set to be zero throughout the simulations. The objective of this case is to compare the burst strength between Abaqus CAE and theoretical equations, some of which are derived based on the Po = 0 assumption. The simulation results for all degrees of wear can be seen in Appendix C.

The trend of the slopes seems to be the same as in Case Po ≠ 0: linear and parallel to each other. The summary of the linear interpolation applied to the intersection points gives the results as shown in Figure 70.

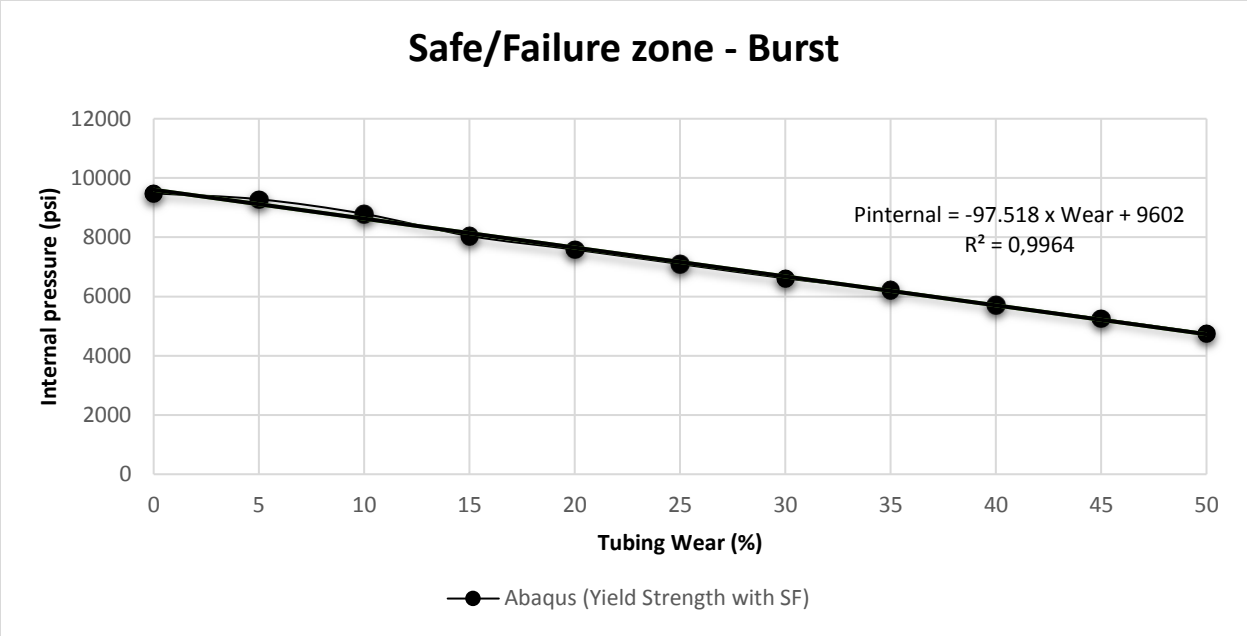

Figure 70: Safe/failure zone for varied internal pressure – Po = 0

The intersection points in this case also have the same trend compared to Case Po ≠ 0. The linear regression is obtained and gives the burst equation model as:

$$Pinternal = -97.518\, x\, Wear + 9602 \tag{4.9}$$

$R^2 = 0.9964$ shows that the model has a high confidence when it is fitted to the regression line. The results also show that the burst pressures when Po = 0 are lower compared to Po ≠ 0. This means that when no outside pressure is applied, there is no support that can hold back the pressure acting inside the pipe to reduce the burst load.

Application of API Equation and Tri-axial Equation (Theoretical Equations) for Burst Pressure

The most common theoretical equation used by the API standard to calculate burst strength is Barlow equation. This expression is derived analytically from Lame's equation for a thin-walled cylinder assuming that there is no axial stress and external pressure applied. The burst strength of the T-95 tubing calculated with Barlow equation is 9,393 psi with safety factor (SF = 87.5%). For

a thick-walled cylinder, the Tri-axial design in equation 2.23 will be used to take into account the external pressure in the burst design pressure. In this case, the application of these theoretical equations will be investigated for the uniform corrosion condition.

a. Case Po ≠ 0

In this case, the burst pressure is calculated with both Barlow and Tri-axial equations and is compared with the simulation results. Since there is no σ_a applied, it is set to be 0. The summary of the calculation is presented in Table 24.

Table 24: Calculation of burst pressure vs. simulation – Po ≠ 0

Wear (%)	Cylinder Type	Burst Pressure from Equation (psi)			Burst Pressure from Simulation (psi)
		Barlow	Barlow + Po	Tri-axial	Abaqus
0	Thick-Walled	9393	11455	11473	11642
5	Thick-Walled	8923	10986	11010	11443
10	Thick-Walled	8454	10516	10547	10943
15	Thick-Walled	7984	10046	10082	10191
20	Thin-Walled	7515	9577	9616	9726
25	Thin-Walled	7045	9107	9149	9234
30	Thin-Walled	6575	8637	8681	8746
35	Thin-Walled	6106	8168	8212	8342
40	Thin-Walled	5636	7698	7743	7842
45	Thin-Walled	5166	7228	7272	7368
50	Thin-Walled	4697	6759	6801	6869

The simulations show that the trend approaches linear, while both equations have linear trends. The Tri-axial equation is better fitted to the simulation compared to Barlow with safety factor of 87.5%. In the simulations, the external pressure is not zero, representing the real-world condition of tubing in a well which is exposed to loadings in annulus. The same assumption where Po ≠ 0 is applied to the Tri-axial equation. Hence, the simulation and Tri-axial equation have similar results and satisfy each other.

Comparing the simulations with Barlow shows that Barlow gives the lower values. Barlow is initially derived based on the assumption that the external pressure is zero. To investigate the

application of this equation to the de-rated tubing cases, the same external pressure applied in Abaqus is added to Barlow (P Barlow + Po) to get the same condition as the simulation. It is shown in Figure 71 that this modified equation matches and satisfies the simulation. It is also shown that Barlow has a slightly narrower safe window compared to the simulations, meaning that the equation has higher DF.

For a thick-walled cylinder (wear depth 0-15%), there is a decreasing linear trend with small disturbances at the beginning. This might be due to the meshing size applied on the tubing model. In this FEM simulation, the same meshing size (0.2) is set in the model for all different wear depth. When it is applied to a thick-walled cylinder, each grid resulting from the meshing process has a coarser shape compared to a thin-walled cylinder. In the numerical analysis, the finer grid will resolve a model to a greater accuracy but the simulation takes a longer time.

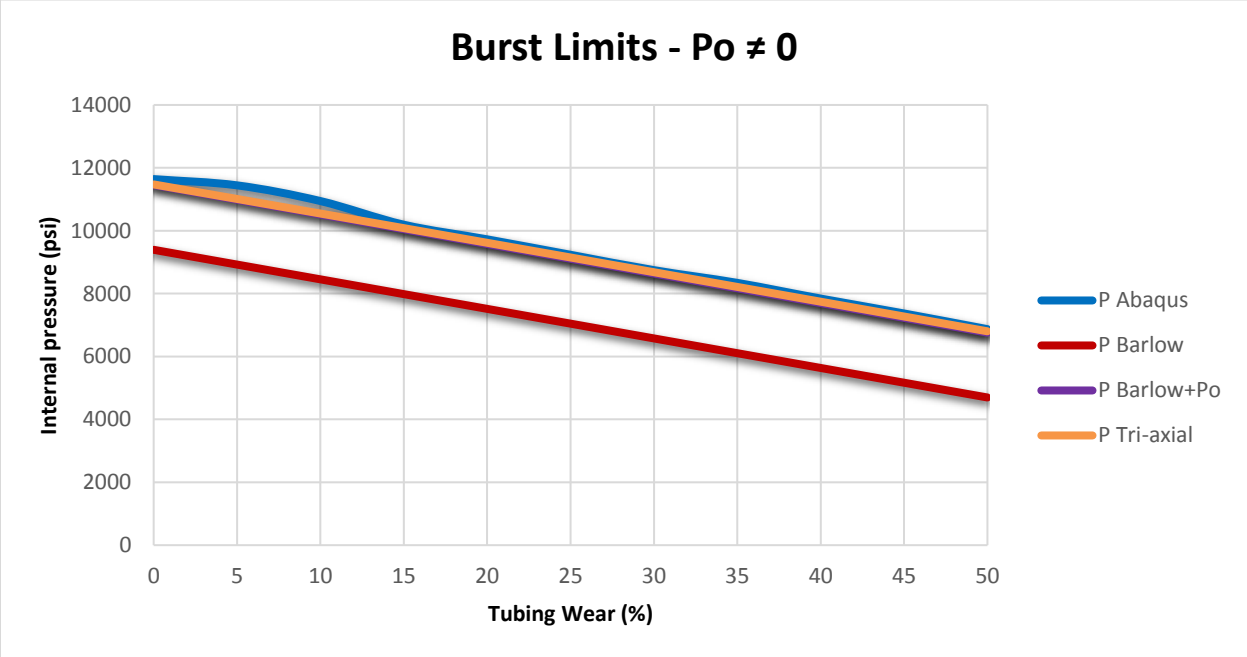

Figure 71: Simulation vs. theoretical results for Po ≠ 0 – burst cases

b. Case Po = 0

To get the same assumption as Barlow equation, the simulation is set with Po = 0. The Tri-axial equation is also used to estimate the burst strength with Po and $\sigma_a = 0$. Figure 72 shows that the

simulation and the equations have broadly similar trends and values in pressure even though the simulations have slightly higher values at the beginning. In general, the simulations satisfy the Barlow and Tri-axial equations as all three set the same assumption of Po = 0.

For a thick-walled cylinder (wear depth 0 – 15%), it is the same case as for Po ≠ 0 where a decreasing linear trend with slightly small disturbances occurs due to the application of the same meshing size for all wear depth.

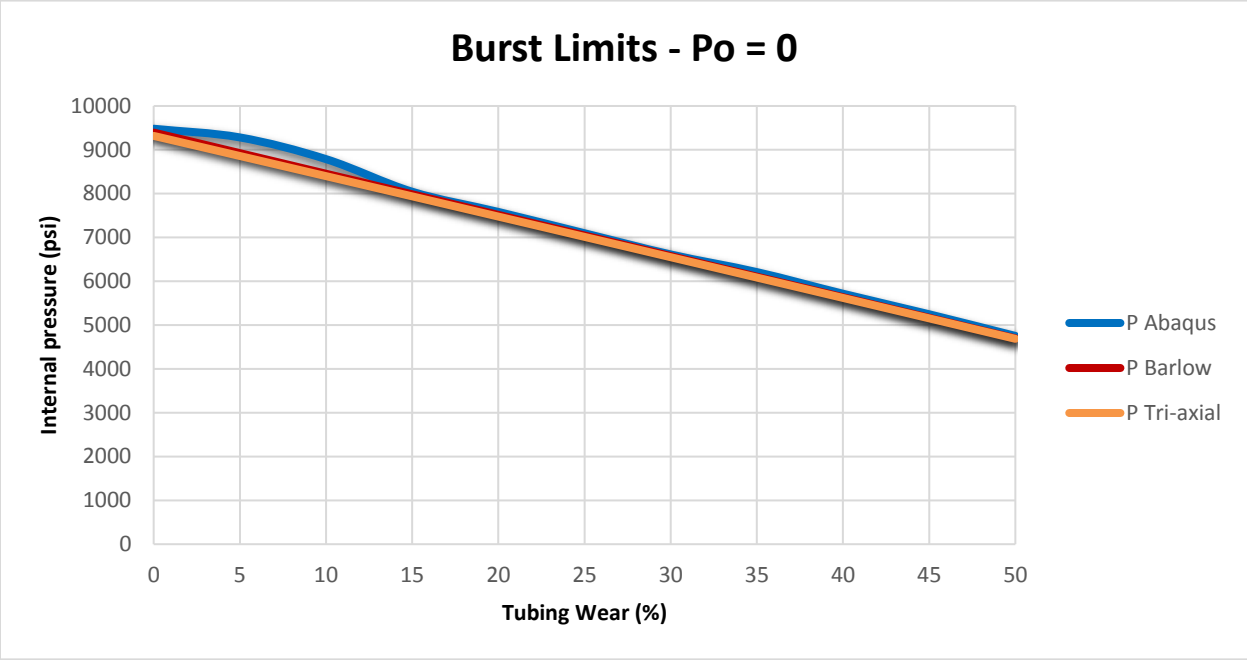

Figure 72: Simulation vs. theoretical results for Po = 0 – burst case

4.4.7.2.2 Case 2 – Collapse

Collapse occurs when the differential pressure between external and internal pressure exceeds the collapse rating pressure of the tubing. In the real world, collapse in tubing can be caused by annular pressure build-up due to fluid heating, a leak in the production casing, pressure testing in the annulus, or some artificial lift installations such as a gas lift. In this simulation study, the collapse cases are developed based on real-world field conditions. In the case where internal pressure exists, it is assumed that the well is optimized using the gas lift. To open the operating valve, the pump pressure has to be applied from the surface and it may develop pressure build-up in the annulus.

In the gas lift unloading process, pump pressure is also needed to evacuate the completion fluid before the gas lift can be operated. If the internal pressure is set to be 0, it is assumed that the well is completed with a sand screen and experiences sand face blockage during the production time. The tubing is full of gas and the wellhead is opened to atmospheric pressure, resulting in very low tubing pressure [9].

The simulation procedure in Abaqus CAE is similar to that of the burst cases, but in the collapse case, the inner pressure will be set as constant throughout the simulation and the external pressure would vary. The same T-95 tubing with σ_y = 95,000 psi is also used with SF = 87.5%. The internal pressure set in this case is the well pressure with oil gradient equal to 0.3 psi/ft at the maximum deviation point (4525.7 ft TVD).

Internal pressure calculation:

$$P_i = P_{res} - \rho_{oil} g h \tag{4.10}$$

$$P_i = 5400\ psi - 0.3\frac{psi}{ft} \times (10000 - 4524.7) ft = 3758\ psi$$

Abaqus CAE Simulation Results

Similar to the burst case, for the collapse simulation, the two cases are evaluated based on the different inner pressure (**Pi**) loading.

a. Case Pi ≠ 0

In this case, the varied external pressures for each wear depth are applied and the point where σ_{VME} intersects σ_y will be determined following the same procedures as in the burst cases. The stress distribution result from the simulation for the unworn tubing (0% wear) is shown in Figure 73. The red color shows the area with the highest stress; the stress distribution is uniform and there is no localized stress point.

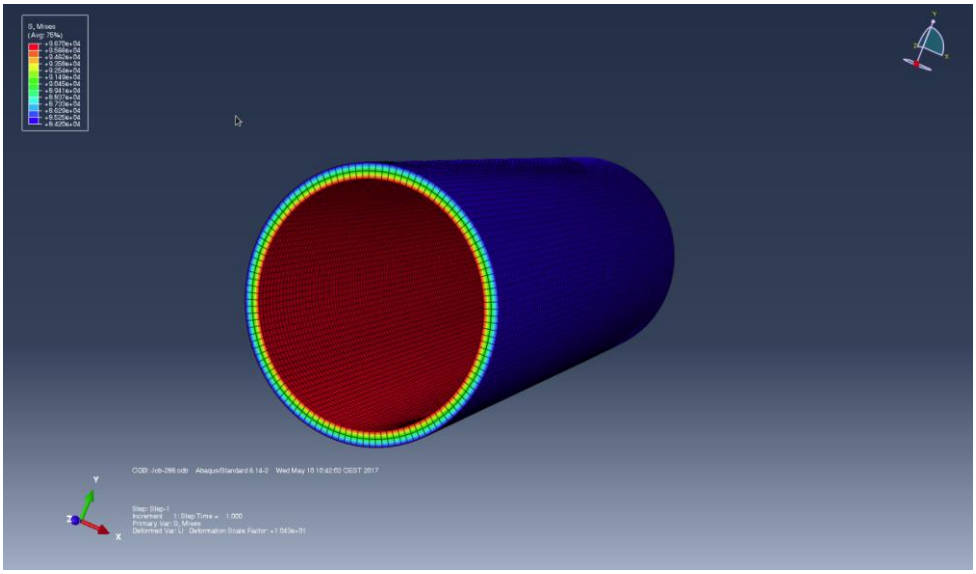

Figure 73: Stress distribution in unworn tubing for collapse case (Pi ≠ 0) – uniform corrosion

The summary of Von-Mises stress comparison between wear 0% and 5% is presented in Appendix C. The reduction of the burst strength is approximately 1.48%. For extremely higher wear (50%), σ_{VME} = 8930 psi and the strength reduction is about 35.4%. The results show the same trend as the burst cases where the higher the wear percentage, the lower the Von-Mises stress that causes the tubing yield.

The simulation results for all wear percentages can be seen in Appendix C. The slopes for each wear seem to be linear and parallel to each other, and the trend is similar to the burst cases. The next step is the same as for the burst case where the intersection points between σ_{VME} and σ_y are obtained. The summary of linear interpolation for σ_y = 95000 psi (without safety factor) and σ_y = 83125 psi (with safety factor 87.5%) is also shown in Appendix C.

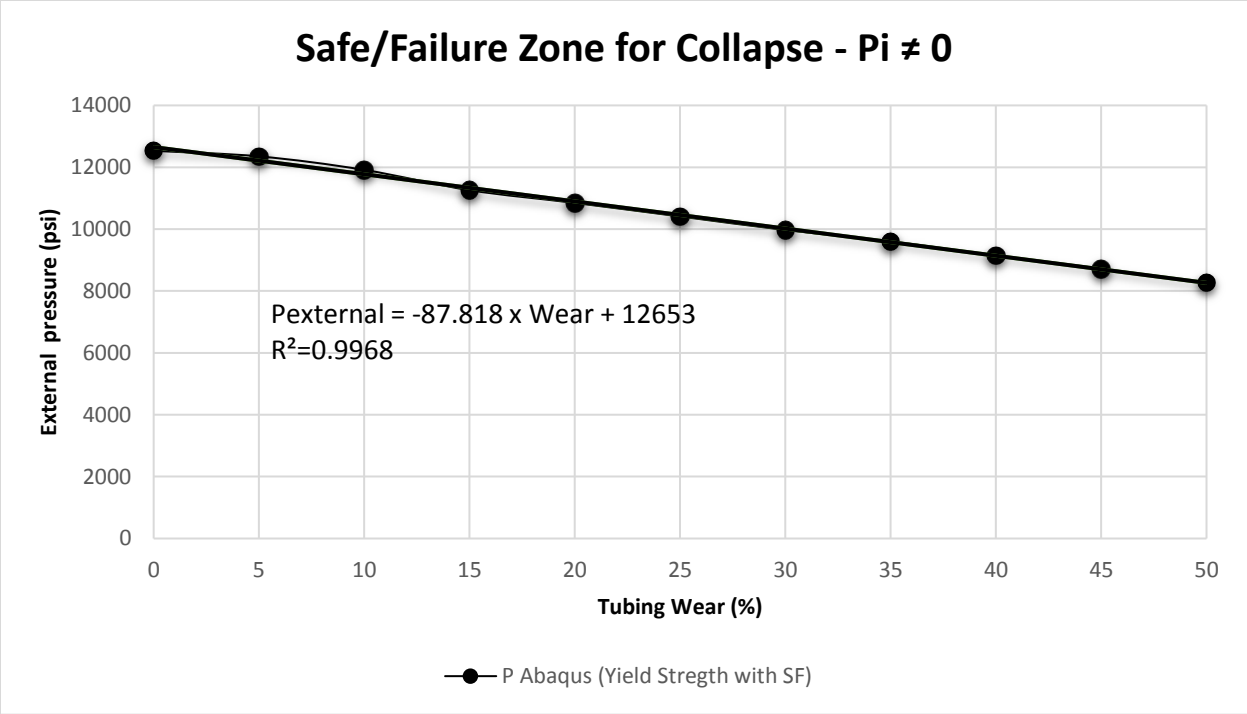

Figure 74: Safe/failure zone for varied external pressure – Pi ≠ 0

The pressure line showing collapse limits for different wear as a result of linear interpolation is shown in Figure 74. From this simulation result, the collapse pressure equation for de-rated tubing can be summarized as:

$$Pexternal = -87.818\ x\ Wear + 12653 \tag{4.11}$$

The high value of R^2 = 0.9968 shows that the simulation data and the fitted regression line are matched. The trend of slope is more linear compared to the burst cases, which illustrates that when the thickness of the tubing is reduced uniformly, the collapse strength is reduced in a linear way. The zone below the pressure line is the safe zone, while the zone above represents the failure zone.

b. Case Pi = 0

The same simulation steps are applied, but the internal pressure is set to be zero throughout the simulation to see the difference compared to the previous case. The simulation results for all degrees of wear can be seen in Appendix C. The trend of the slopes seems to be the same as in the

case Pi ≠ 0: linear and parallel to each other. The linear interpolation applied to the intersection points gives the results as shown in Figure 75.

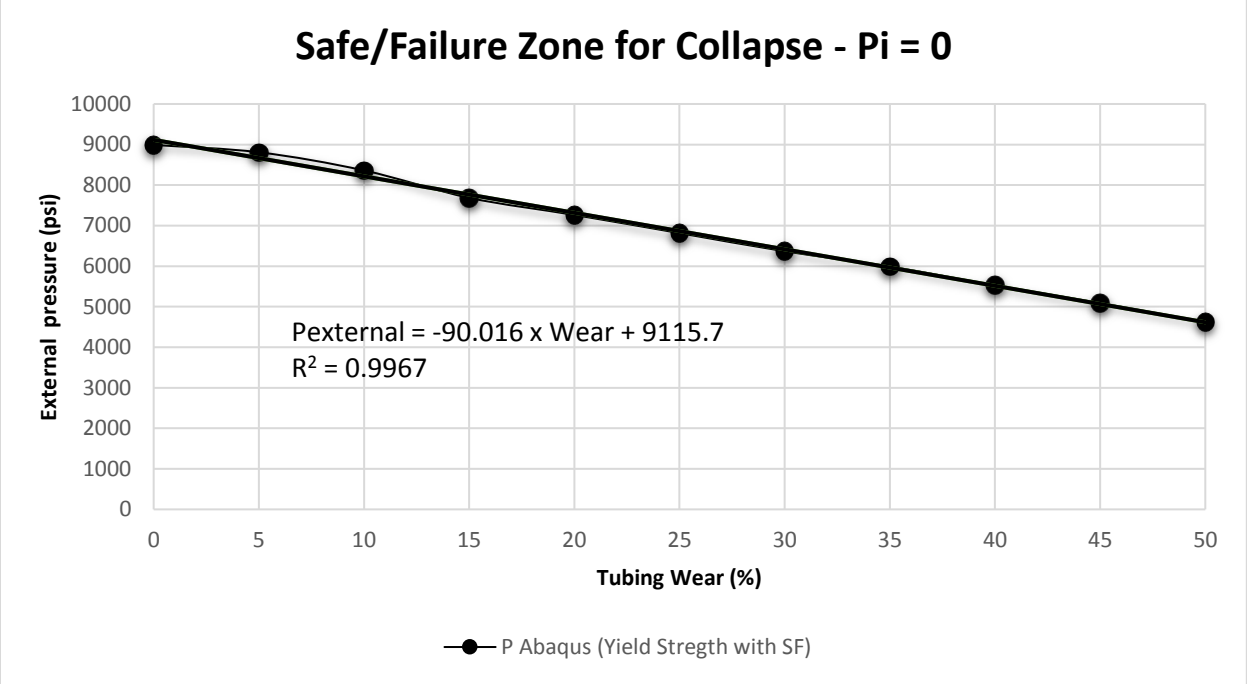

Figure 75: Safe/failure zone for varied external pressure – Pi = 0

The intersection points in this case also give the same trend compared to Case Pi ≠ 0. The linear regression is obtained and gives the collapse equation model as:

$$Pexternal = -90.016\ x\ Wear + 9115.7 \tag{4.12}$$

The $R^2 = 0.9967$ is quite high and approaches 1. This shows that the model has a high confidence when it is fitted to the regression line. The results also show that the collapse pressure when Pi = 0 is lower compared to Pi ≠ 0. This can be interpreted to mean that when there is no acting inside pressure, there is no support that can hold back the pressure acting in the outside pipe to reduce the collapse load.

Application of API Equation and Tri-axial Equation (Theoretical Equations) for Collapse Pressure

a. Case Pi ≠ 0

In this case, the simulation results will be compared to the API collapse equation and Tri-axial equation. The σ_a is set to be zero since the tubing is modeled as open ended.

Table 25: Calculation of collapse pressure vs. simulation – Pi ≠ 0

Wear (%)	Cylinder Type	D/t	Collapse Type	Collapse Pressure from Equation (psi)		Collapse Pressure from Simulation (psi)
				API	Tri-axial	Abaqus
0	Thick-Walled	17.7	Plastic Collapse	9920	12413	12531
5	Thick-Walled	18.6	Plastic Collapse	9185	12005	12353
10	Thick-Walled	19.7	Plastic Collapse	8449	11594	11916
15	Thick-Walled	20.8	Plastic Collapse	7713	11181	11259
20	Thin-Walled	22.1	Transitional Collapse	7142	10765	10846
25	Thin-Walled	23.6	Transitional Collapse	6672	10346	10409
30	Thin-Walled	25.3	Transitional Collapse	6203	9925	9972
35	Thin-Walled	27.2	Transitional Collapse	5732	9502	9604
40	Thin-Walled	29.5	Elastic Collapse	5266	9075	9153
45	Thin-Walled	32.2	Elastic Collapse	4873	8646	8724
50	Thin-Walled	35.4	Elastic Collapse	4552	8215	8269

The type of API collapse equation is used based on the slenderness ratio (D/t) of each tubing as explained in Chapter 2. In this case, since the internal pressure is not zero, it is necessary to re-arrange equations 2.29 and 2.30 to take into account the internal pressure in the API collapse equation.

Recall equations 2.29 and 2.30:

$$Collapse\ SF = \frac{P_C}{P_E} \tag{4.13}$$

$$P_E = P_O - \left[1 - \frac{(d_o - d_i)}{d_o}\right] P_i \tag{4.14}$$

Combine equations 2.29 and 2.30:

$$P_E = \frac{P_C}{Collapse\ SF} \tag{4.15}$$

$$P_O - \left[1 - \frac{(d_o - d_i)}{d_o}\right] P_i = \frac{P_C}{Collapse\ SF} \tag{4.16}$$

$$P_O = \frac{P_C}{Collapse\ SF} + \left[1 - \frac{(d_o - d_i)}{d_o}\right] P_i \tag{4.17}$$

From the simple derivation above, the external pressure where Pi ≠ 0 can be calculated using equation 4.18, the summary of the calculation is shown in Table 25. The Tri-axial is calculated using equation 2.31.

As shown in Figure 76, the Tri-axial equation acts linearly in comparison to wear percentages, while the simulation and API equation have roughly linear trends. The Tri-axial equation seems to match the simulation and satisfies the FEM simulation. The pressure calculated from the API equation seems to be lower compared to the simulation result since, in Abaqus CAE, the tubing is supported with internal pressure while the API collapse equation is derived only based on pipe geometry and does not take into account the internal pressure. For the thick-walled tubing (0 – 15% wear), the simulation and API equation show a slightly less linear trend compared to thin-walled tubing (20 – 50% wear). Comparing the safe window, the API equation gives a narrower window compared to the simulation and Tri-axial equation, meaning the API equation has the most conservative prediction of collapse strength.

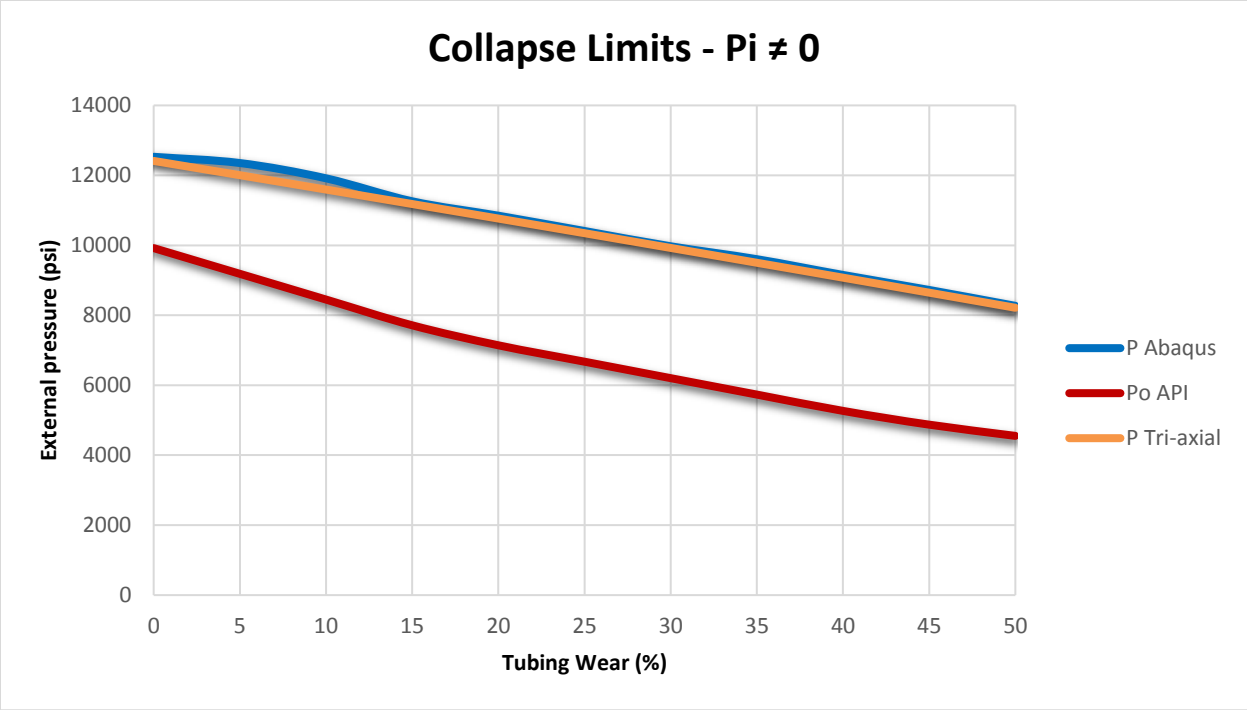

Figure 76: Simulation vs. theoretical results for Pi ≠ 0 - collapse case

b. Case Pi = 0

The purpose for this case in which the internal pressure is set to be zero is to investigate the application of the FEM simulation when there is no support pressure applied and then compare it to the theoretical equations where the same assumption is set. The summary of the calculation and simulation is presented in Appendix C.

As shown in Figure 77, the simulation gives the highest value of collapse strength. The same trend as the case Pi ≠ 0 is obtained in that the API equation gives the lowest result and presents the most conservative design. The Tri-axial equation seems to be well fitted to the simulation. Similar to the case Pi ≠ 0, the simulation and API equation for thick-walled tubing are slightly less linear than for thin-walled tubing.

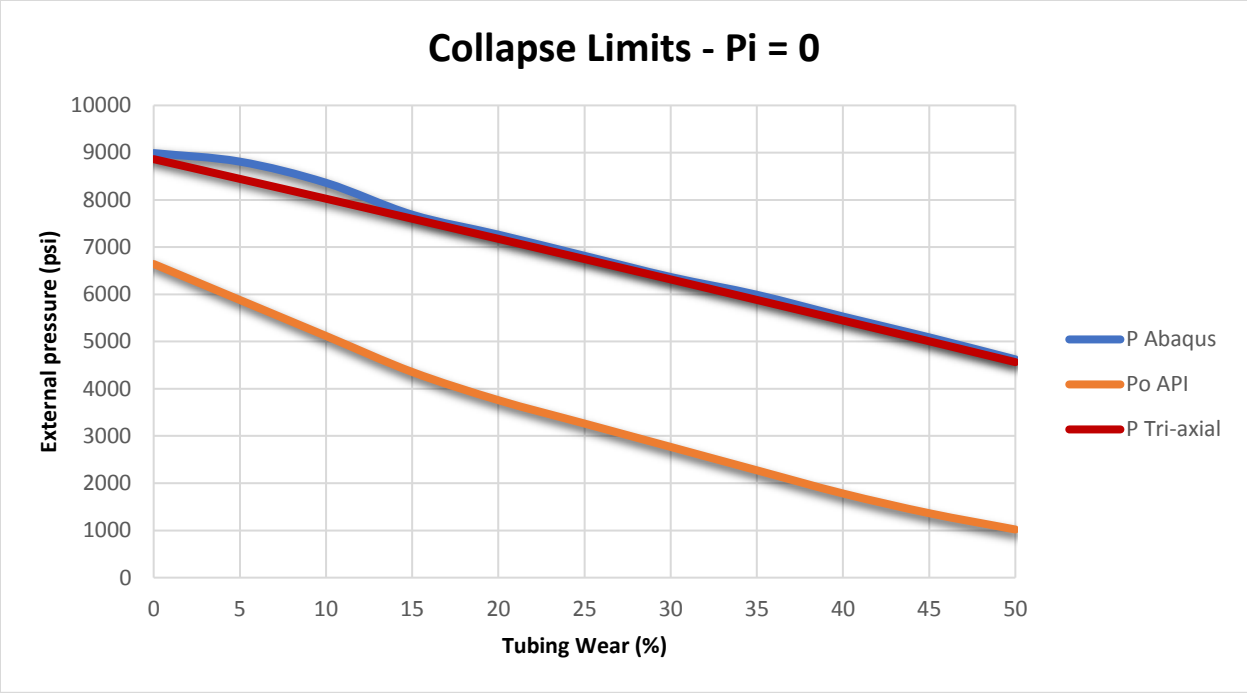

Figure 77: Simulation vs. theoretical results for Pi = 0 – collapse case

4.4.7.3 Pitting Corrosion Cases

In this section, the aim of simulating pitting corrosion is to show how the stress distribution will be different from the uniform case and to compare the pressure between the simulation and theoretical results.

In the pitting corrosion case, as the corrosion attack is formed locally, it leads to certain damage of the tubing as shown in Figure 22 in Chapter 2. In this case, the elliptical or subsurface pitting cavities will be modeled. While in uniform corrosion the tubing is reduced uniformly over the entire tubing surface, in pitting corrosion the tubing is reduced only in certain locations as shown in Figure 78.

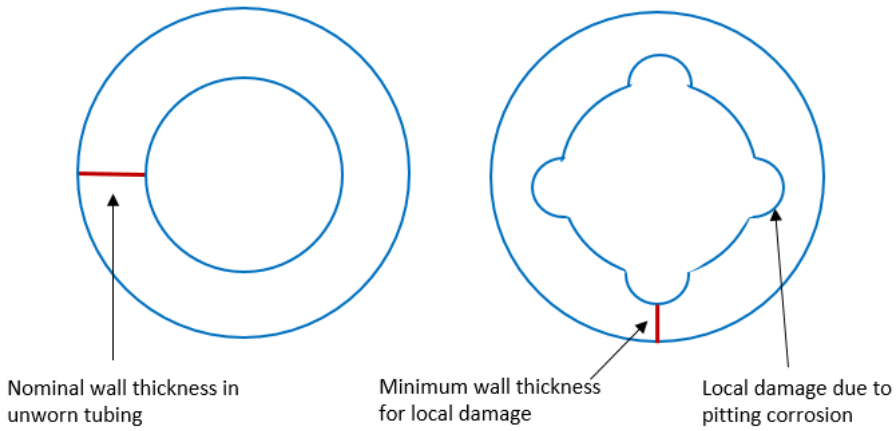

Figure 78: Tubing geometry for pitting corrosion (A) Before deration (B) After deration

Table 26 shows the data for different wear depth for tubing after it is extruded. An example of how to calculate the minimum wall thickness after the tubing is extruded is presented in Appendix A.

Table 26: Tubing data after deration due to pitting corrosion

Wear (%)	OD (in)	Thickness Reduction (in)	New Minimum Wall Thickness (in)	New ID (in)	GeometricFactor β
10	4.000	0.023	0.203	3.593	10.4
20	4.000	0.045	0.181	3.638	11.6
30	4.000	0.068	0.158	3.684	13.2
40	4.000	0.090	0.136	3.729	15.3
50	4.000	0.113	0.113	3.774	18.2

In this simulation case, the tubing models are built for five cases of wear percentages where the tubing inner diameter is extruded by 10 – 50 % wear depth. Each case is also developed for four points and eight points of local damage positions over the entire tubing surface. As shown in Figure 79, there are four positions of local damage due to pitting corrosion. For burst and collapse cases, the same internal and external pressures are applied as in the uniform corrosion scenarios.

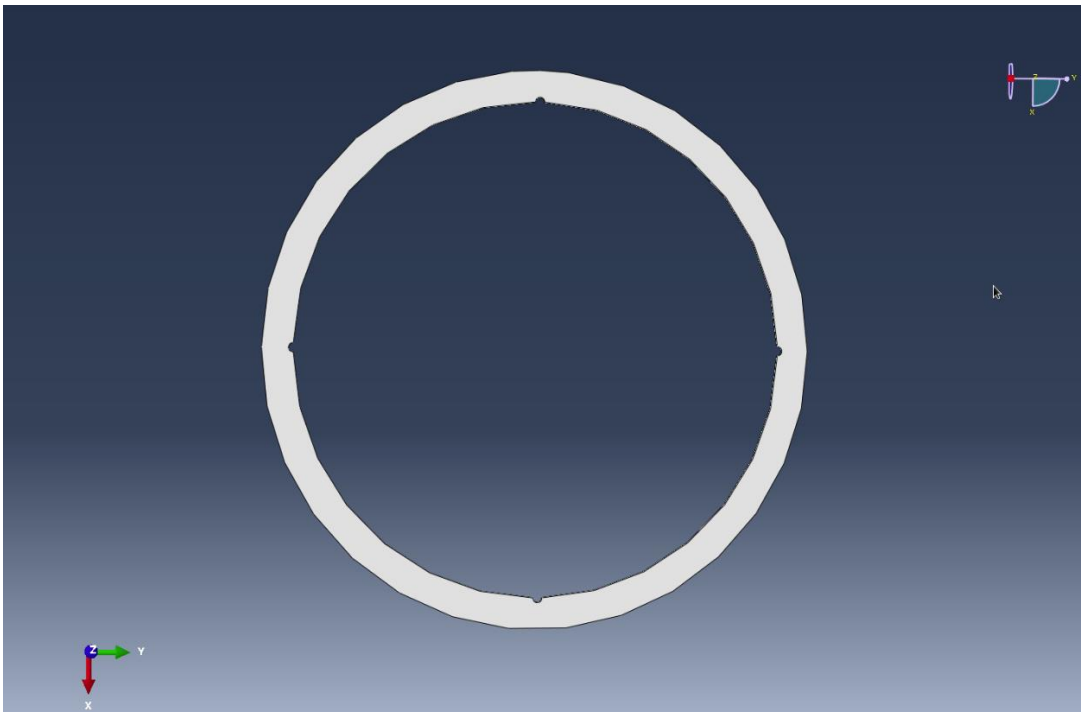

Figure 79: Tubing geometry for four points of local damage due to pitting corrosion

The length of the tubing model is set shorter compared to the uniform corrosion cases to represent the local damages where the shape of the cavity is relatively small and round. The 3D tubing model with applied pressure loadings is shown in Figure 80.

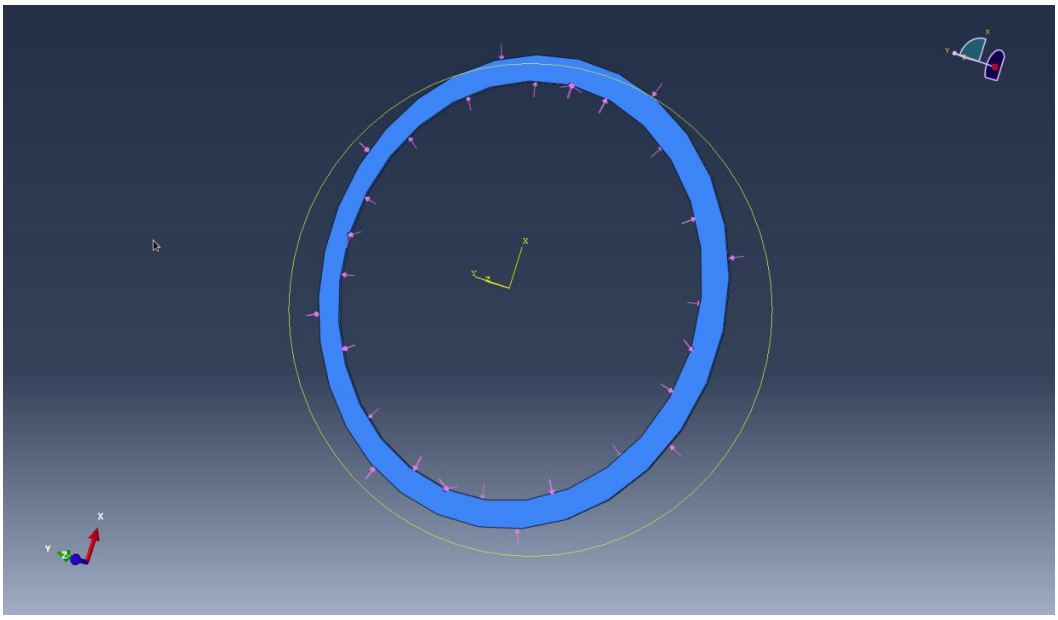

Figure 80: 3D Tubing model with applied pressure loadings – pitting corrosion

4.4.7.3.1 Case 1 – Burst

The same pressure loading as applied in the uniform case is also used in this pitting corrosion case. The burst pressure calculated with Barlow is the same for four and eight points of damage since these two cases have the same minimum nominal wall thickness after the tubing is extruded. In this case, the tubing yield strength with a safety factor (σ_y = 83,125 psi) will be set throughout the simulation.

Abaqus CAE Simulation Results

a. Case Po ≠ 0

The stress distribution result from simulation shows that the highest Von-Mises stress occurs at the point of damage. Figure 81 shows the stress distribution in tubing with 20% wear depth. It is clearly shown that the stress distribution for pitting corrosion is different compared to uniform corrosion where it is distributed uniformly.

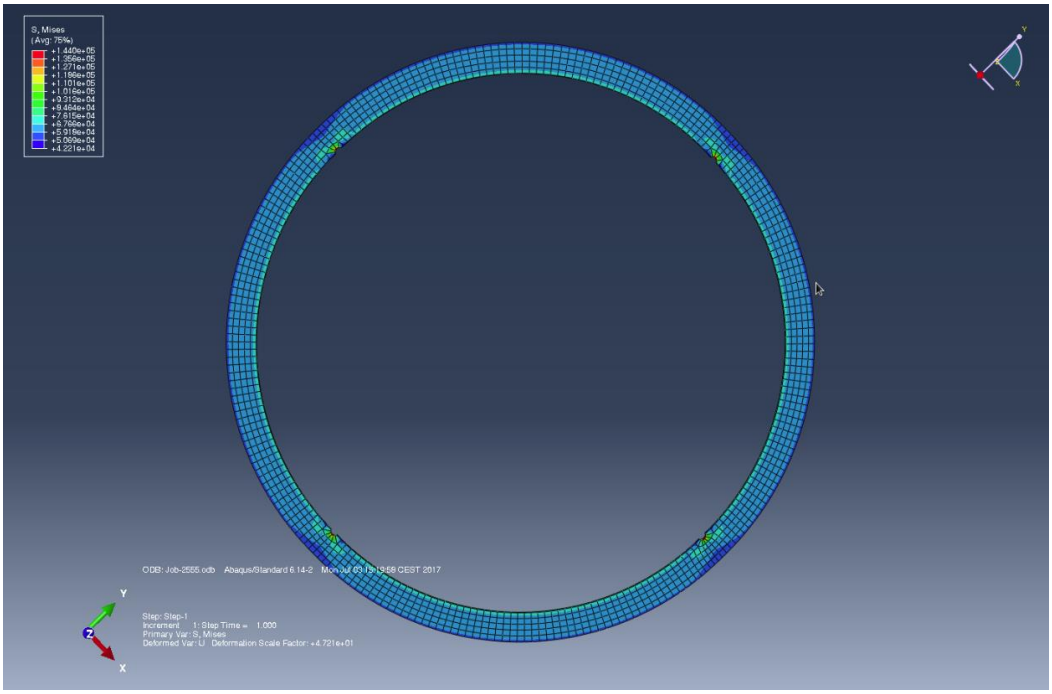

Figure 81: Stress distribution in tubing with 20% wear depth for burst case (Po ≠ 0) – pitting corrosion with 4 points of damage

The same steps used in uniform corrosion are also applied in this case where the varied internal pressure is set and the points where σ_{VME} intersect σ_y are obtained. Figure 87 and Figure 88 show the simulations for four points and eight points of damage and each wear depth shows a linear trend parallel to each other.

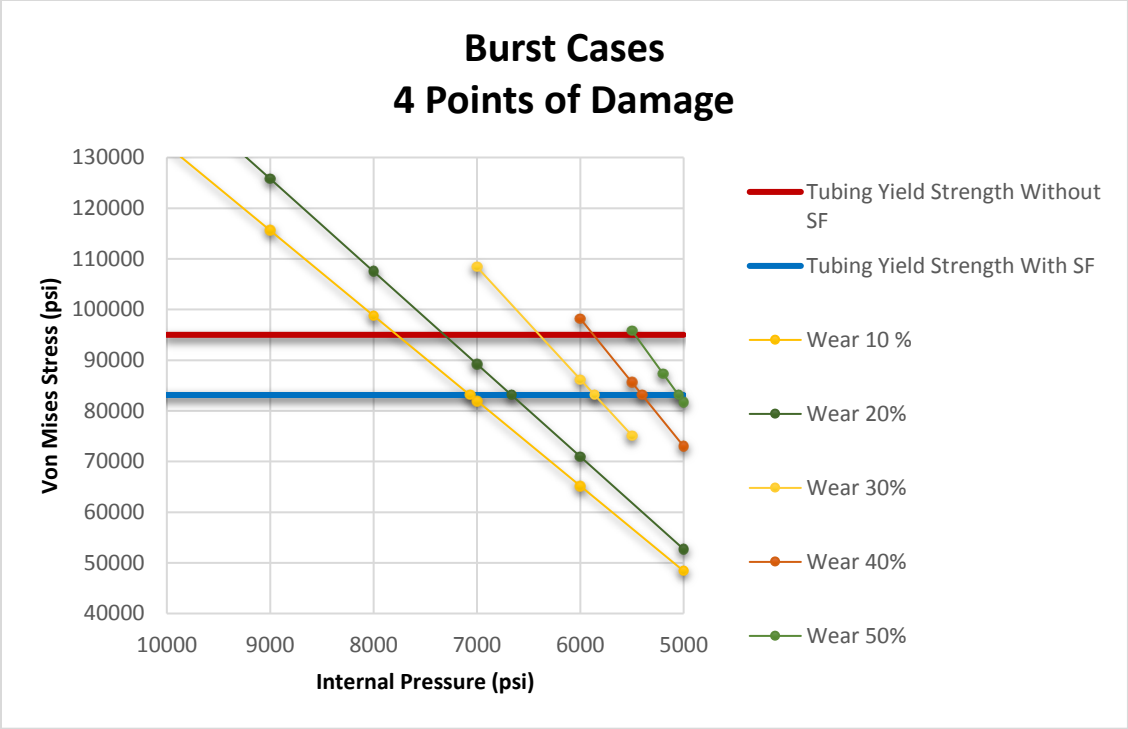

Figure 82: Burst pressure limits for 10% - 50% wear – 4 points of damage

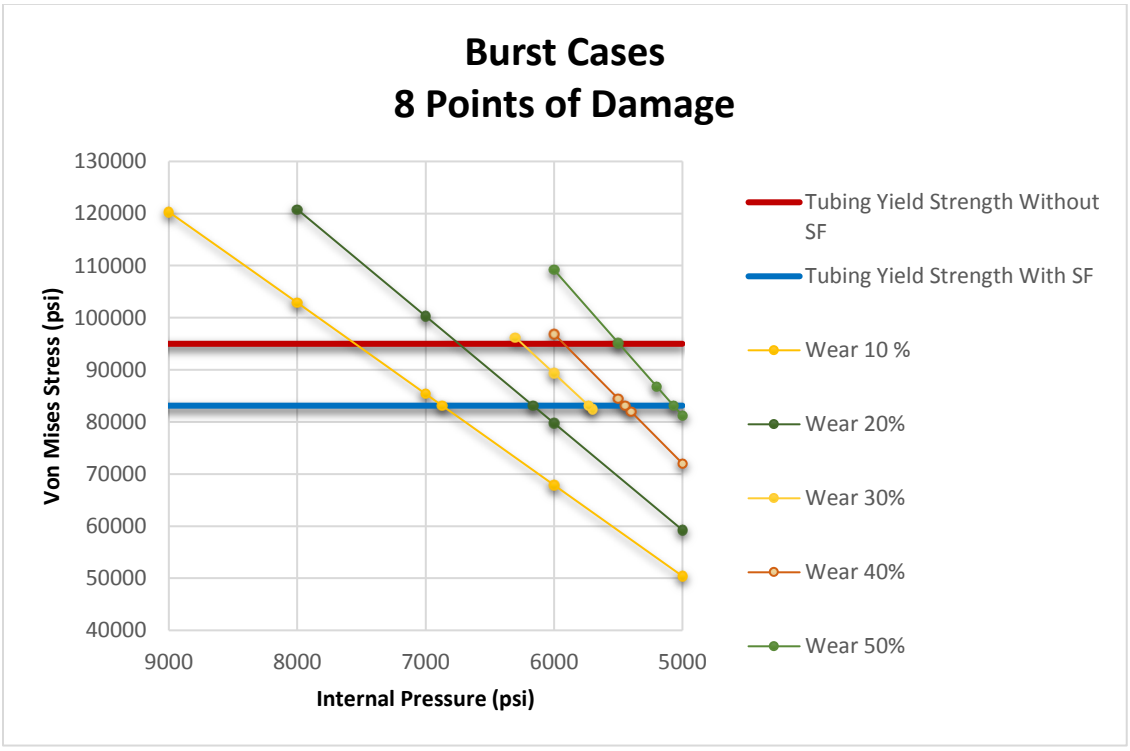

Figure 83: Burst pressure limits for 10% - 50% wear – 8 points of damage

The intersection points between σ_{VME} and σ_y are also obtained from the linear interpolation and the result is presented in Figure 84. Both cases seem to have a linear trend and in general, the eight points of damage condition shows a lower pressure limit and narrower safety window compared to four points of damage.

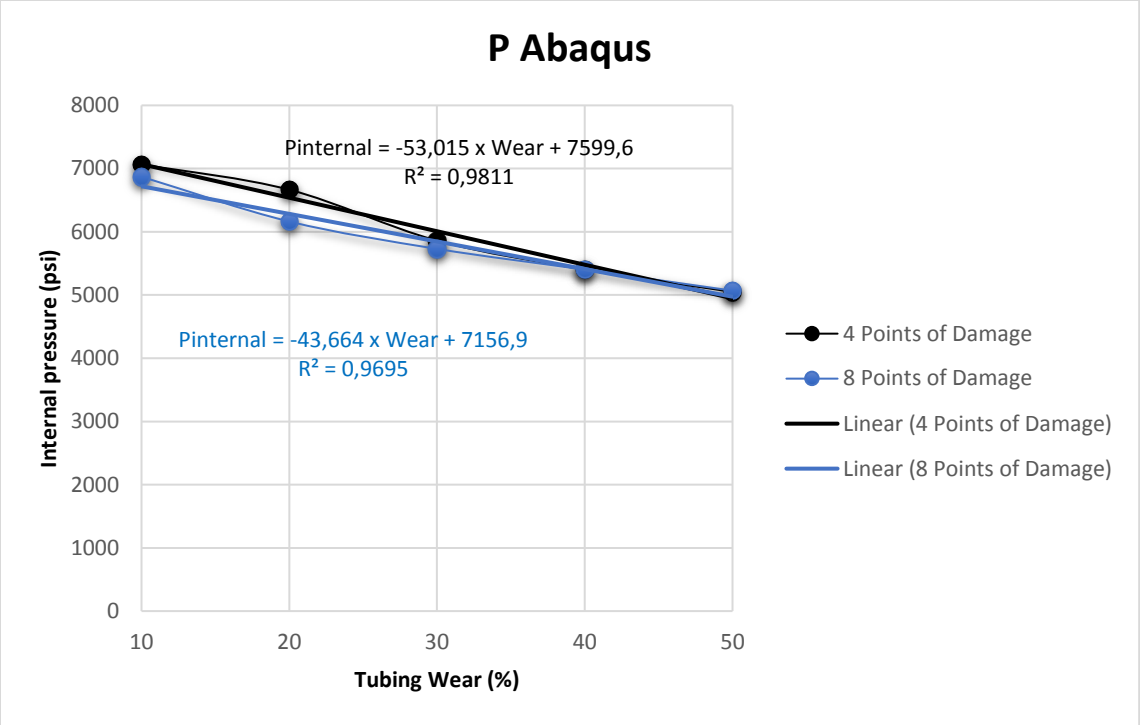

Figure 84: Burst limits for varied internal pressure – Po ≠ 0

b. Case Po = 0

Figure C4 and Figure C5 in Appendix C show the simulation results for both cases, and the intersection points are presented in Figure 85. It is clearly shown that the pressure limits for case Po = 0 are lower than case Po ≠ 0 since, in the absence of external pressure, there is no backup pressure to support the tubing when burst loading occurs.

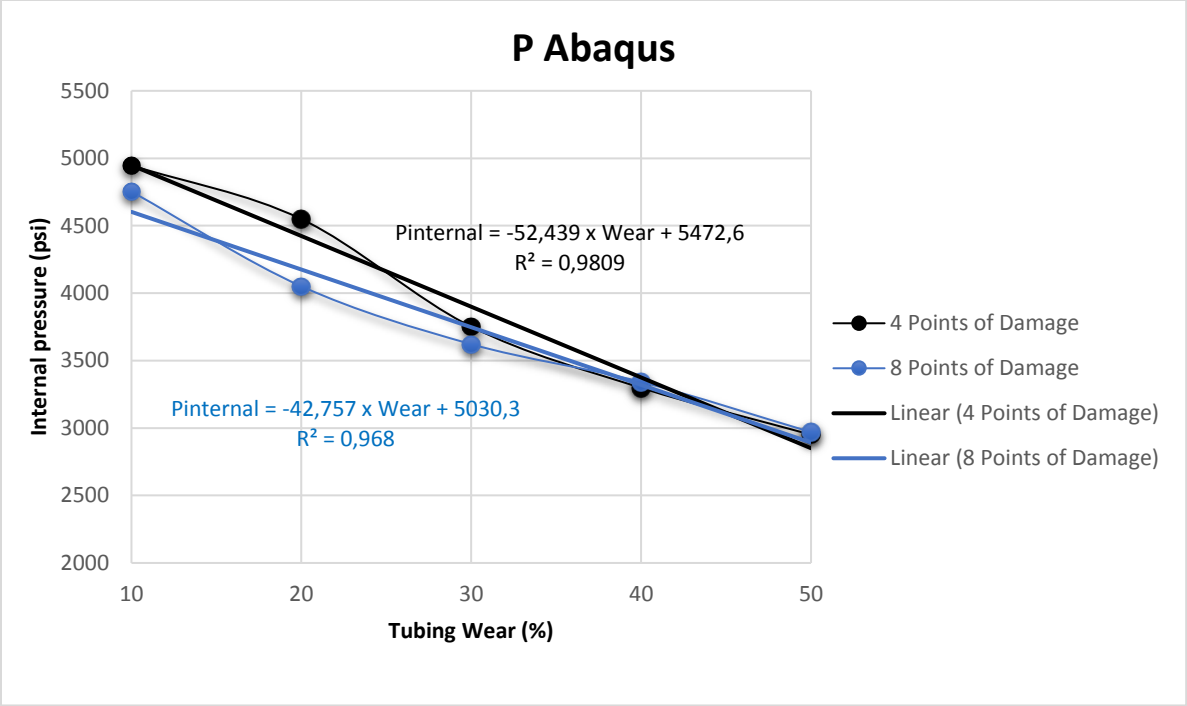

Figure 85: Burst limits for varied internal pressure – Po = 0

Application of API Equation and Tri-axial Equation (Theoretical Equations) for Burst Pressure

a. Case Po ≠ 0

As shown in Table 27 for case Po ≠ 0, the simulation has the lowest pressure rating leading to the narrowest safe window. Furthermore, in the simulation, for more points of damage in the tubing, the pressure rating is lower; the two theoretical equations cannot take into account this condition.

Table 27: Simulation vs. theoretical equations for Po ≠ 0 – burst case

Wear (%)	Cylinder Type	Pressure from Equation (psi)		Pressure from Abaqus Simulation with SF (psi)	
		Barlow	Tri-axial	4 points of damage	8 points of damage
10	Thick-walled	8454	10547	7068	6871
20	Thin-walled	7515	9616	6666	6163
30	Thin-walled	6575	8681	5861	5730
40	Thin-walled	5636	7743	5401	5401
50	Thin-walled	4697	6801	5050	5069

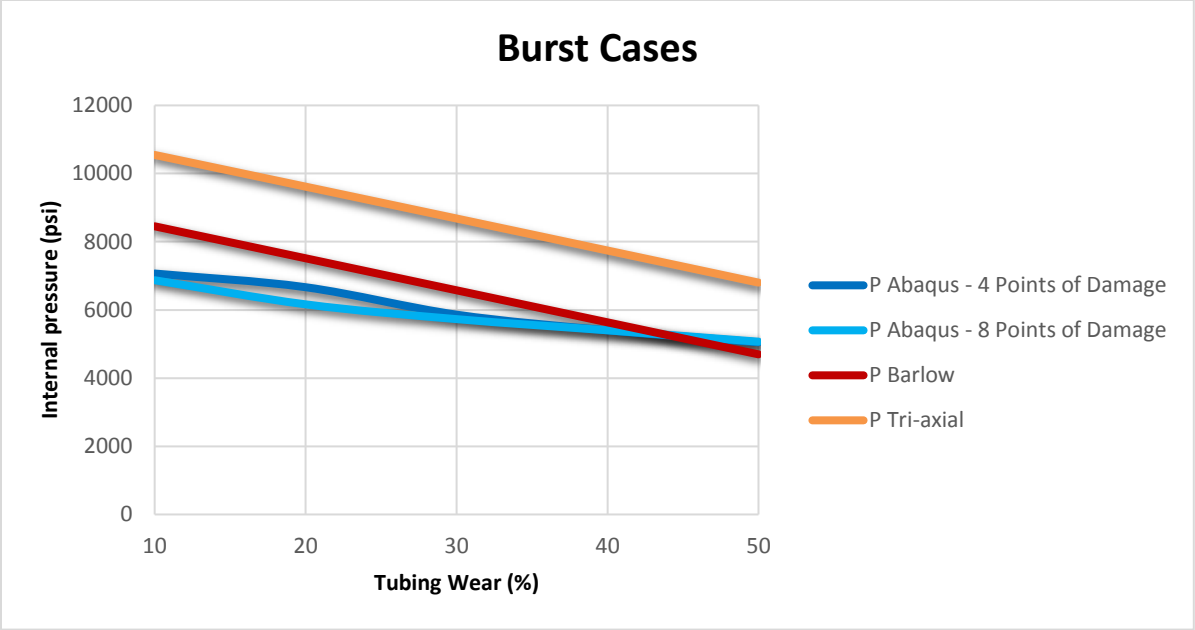

Figure 86: Simulation vs. theoretical results for Po ≠ 0 –burst case

Figure 86 shows that the simulation generally gives the lowest pressure limits, while Tri-axial has the highest values. Barlow gives pressure limits that are closer but slightly greater to the simulation results. Barlow is derived based on an assumption of Po = 0 and in this case, the simulation where the external pressure is applied still gives a lower pressure than Barlow. In the presence of external pressure, the burst limit is supposed to be higher as the external pressure functions as a support pressure. This means that theoretical equations cannot be used to estimate the burst rating when local damage occurs in the tubing.

b. Case Po = 0

Table C7 in Appendix C summarizes the simulation results for case Po = 0. It shows that with the absence of the external pressure, the burst limit is lower.

Figure 87 shows the same trend with case Po ≠ 0 where the simulation gives the lowest pressure. The pressure gap between the simulation and equations is larger compared to case Po ≠ 0 as the absence of external pressure gives lower burst limits. This case clearly shows that the Barlow and Tri-axial equations cannot be applied in the pitting corrosion case.

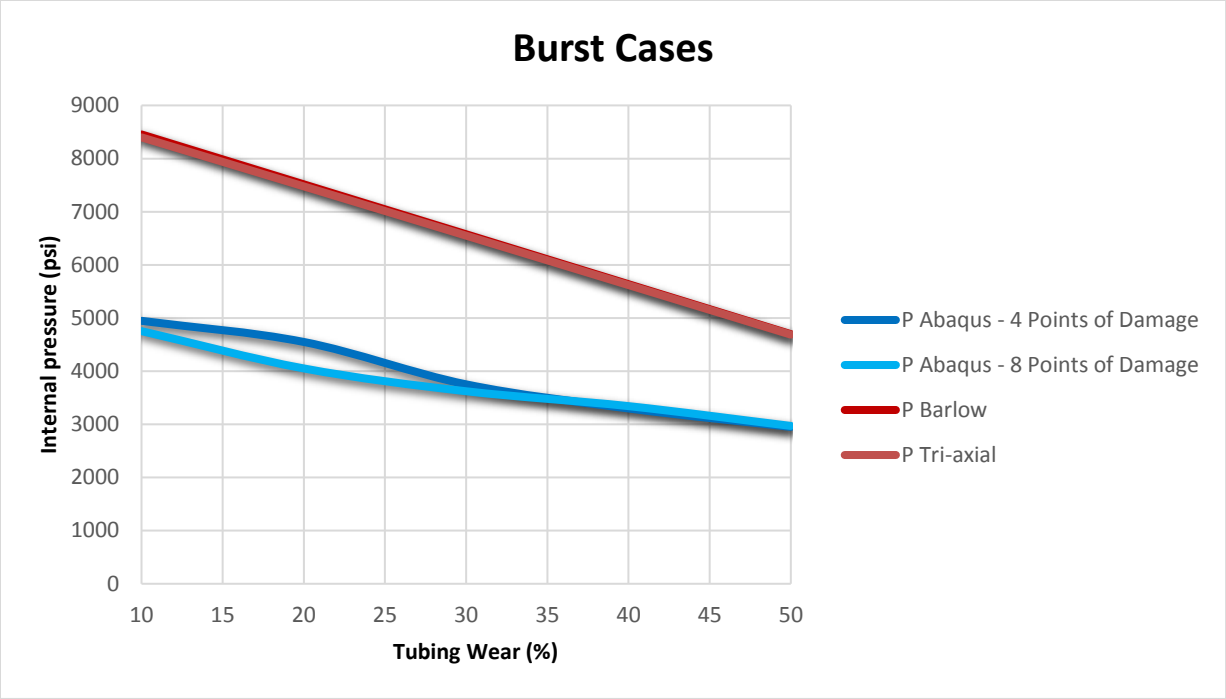

Figure 87: Simulation vs. theoretical results for Po = 0 – burst case

4.4.7.3.2 Case 2 – Collapse

Abaqus CAE Simulation Results

a. Case Pi ≠ 0

The stress distribution from the simulation in Figure 88 shows that the highest Von-Mises stress also occurs at the point of damage.

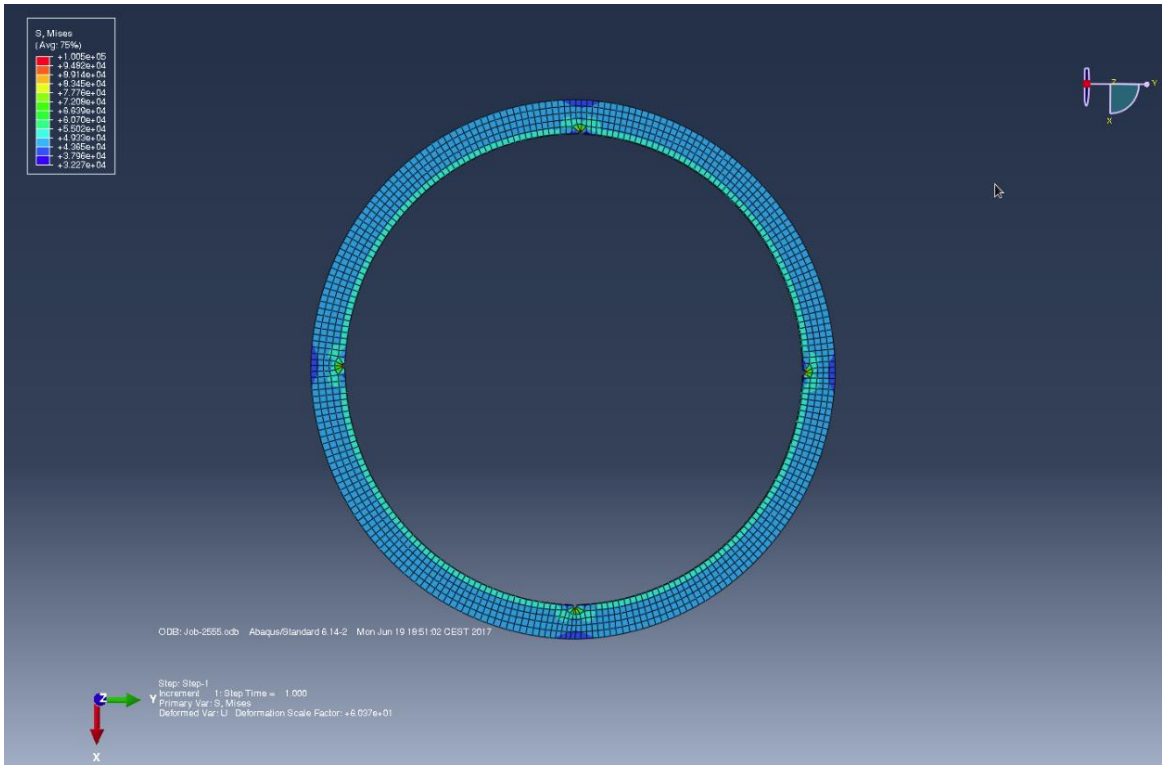

Figure 88: Stress distribution in tubing with 20% wear depth for collapse case (Pi ≠ 0) – pitting corrosion with 4 points of damage

Figure 89 shows that the intersection points for different wear depth have the same trend as the burst case in that tubing with eight points of damage generally has lower collapse limits. Hence, the more points of damage, the narrower the safe window will be.

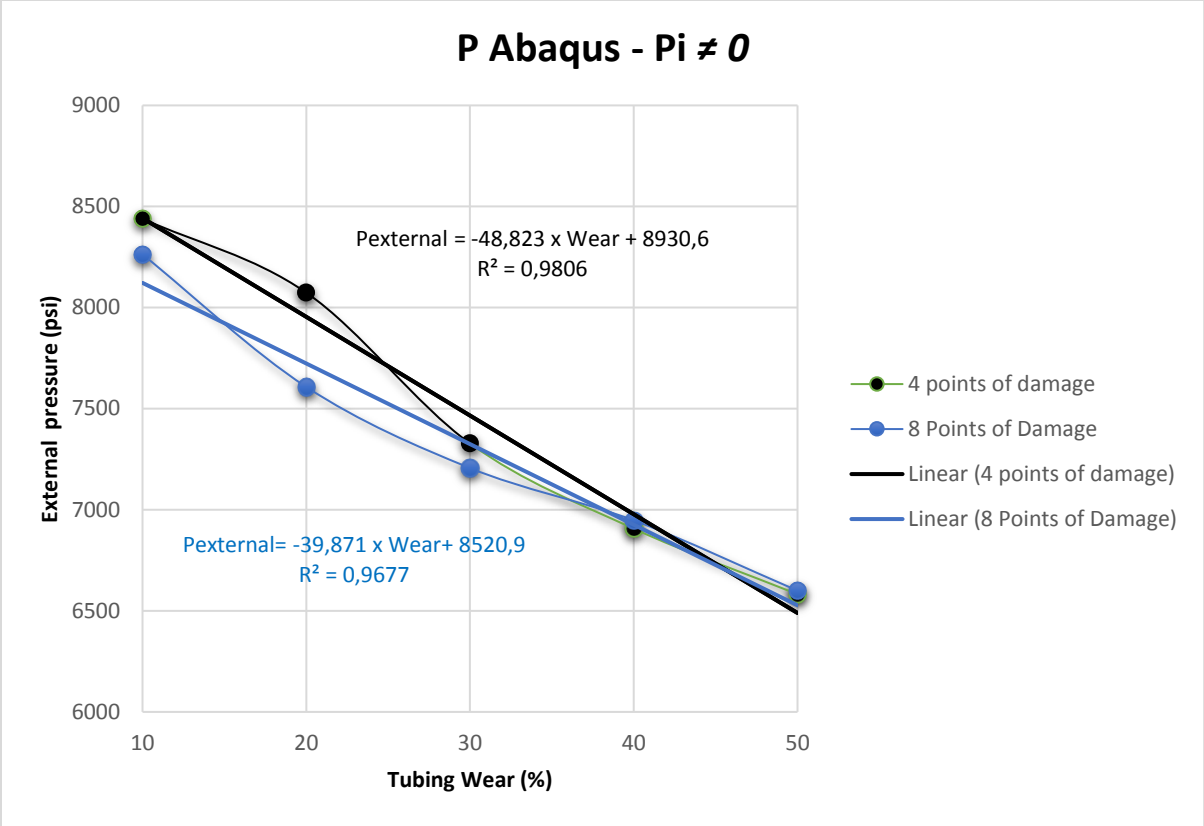

Figure 89: Collapse limits for varied external pressure – Pi ≠ 0

b. Case Pi = 0

Figure 90 shows the collapse limits for Pi = 0. In general, the safe window is narrower compared to case Pi ≠ 0 as there is no acting internal pressure as a support, resulting in lower collapse limits.

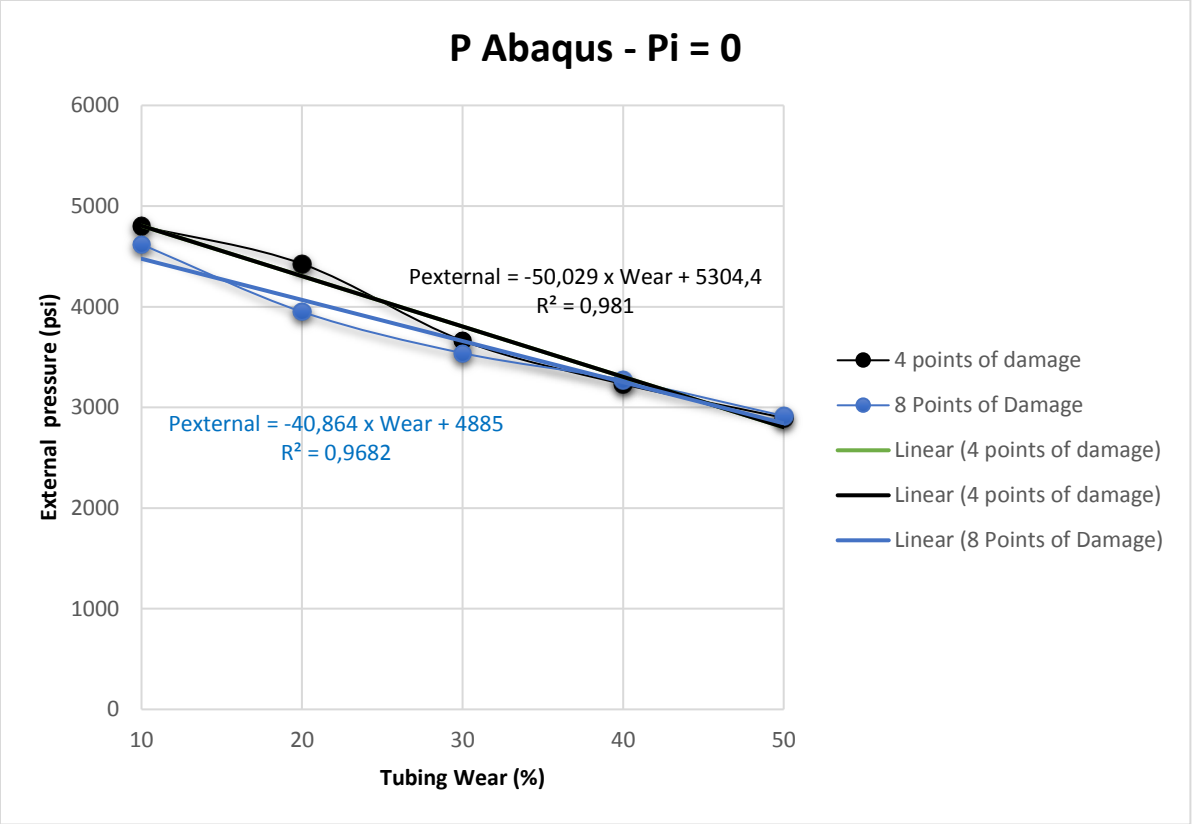

Figure 90: Collapse limits for varied external pressure – Pi = 0

Application of API Equation and Tri-axial Equation (Theoretical Equations) for Collapse Pressure

a. Case Pi ≠ 0

In the collapse case for pitting corrosion, the API equation shows the lowest collapse rating and Tri-axial shows the highest value. As shown in Figure 91, the simulation results seem to be better fitted with the API equation even though the Tri-axial equation cannot take into account the difference between these two points of damage. In this case, the API equation is the most conservative method to predict collapse rating, but the FEM simulation is more applicable since it models the real geometry of the local damage.

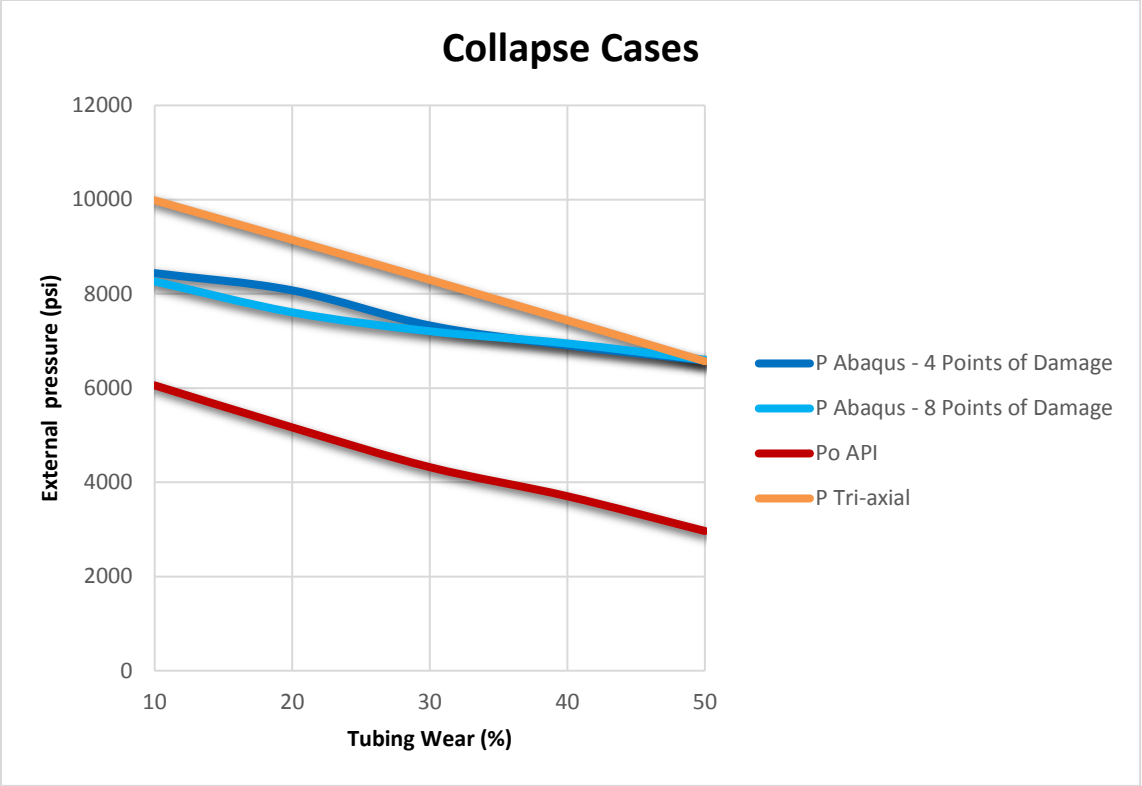

Figure 91: Simulation vs. theoretical results for Pi ≠ 0 – collapse case

b. Case Pi = 0

In the absence of internal pressure, the pressure gap between the API equation and the simulation is smaller as shown in Figure 92. The same trend as in the case Pi ≠ 0 is obtained in which the API collapse equation gives the lowest values and the Tri-axial equation presents the highest value. The FEM simulation gives the values in between.

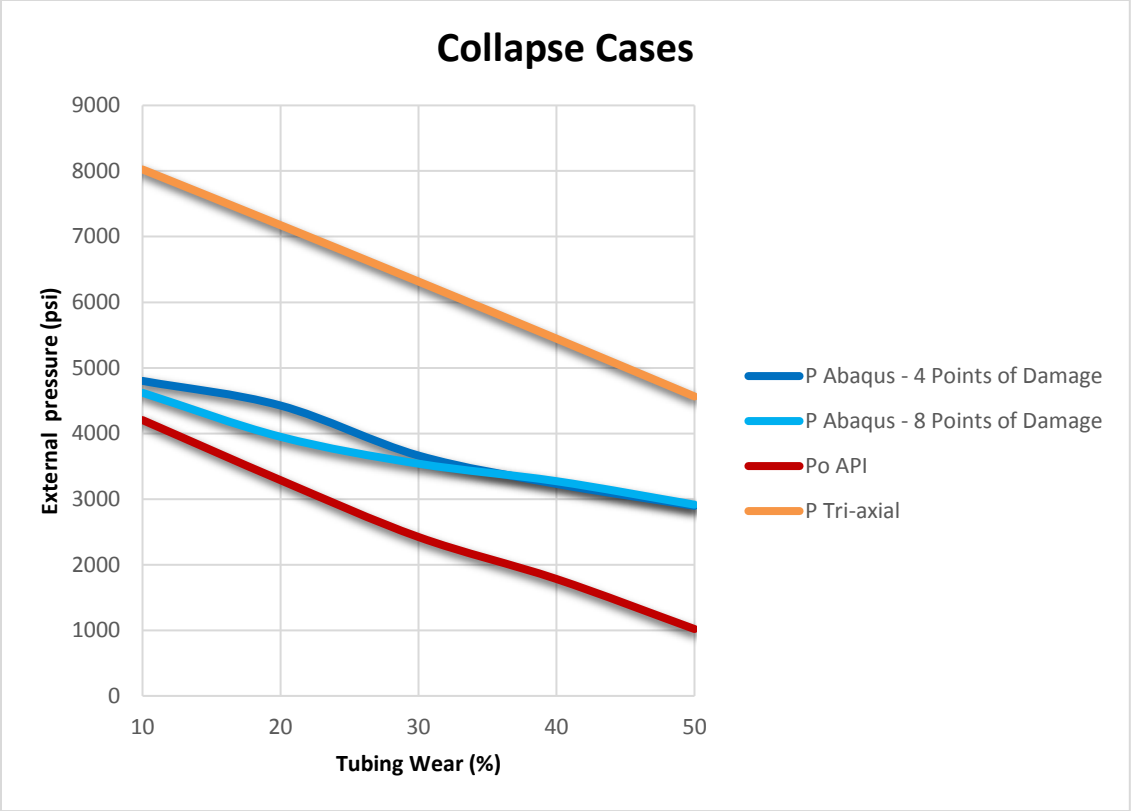

Figure 92: Simulation vs. theoretical results for Pi = 0 – collapse case

Chapter 5 Summary and Discussion

Experience has shown that corrosion causes many problems in the oil and gas industry since it leads to material failures. Corrosion attacks every component at every stage in the life cycle of a well. In their research on Norwegian offshore facilities, Aadnøy and Vignes [4] showed that the highest well integrity problem is due to production tubing failure (39%). This suggests that the industry should pay special attention to tubing design in order to save costs and reduce unnecessary expenditure due to tubing replacement

5.1 Developed Workflow

The overall attempt of this research is to develop a simplified workflow. The developed workflow is implemented in this thesis. Figure 93 shows the workflow chart.

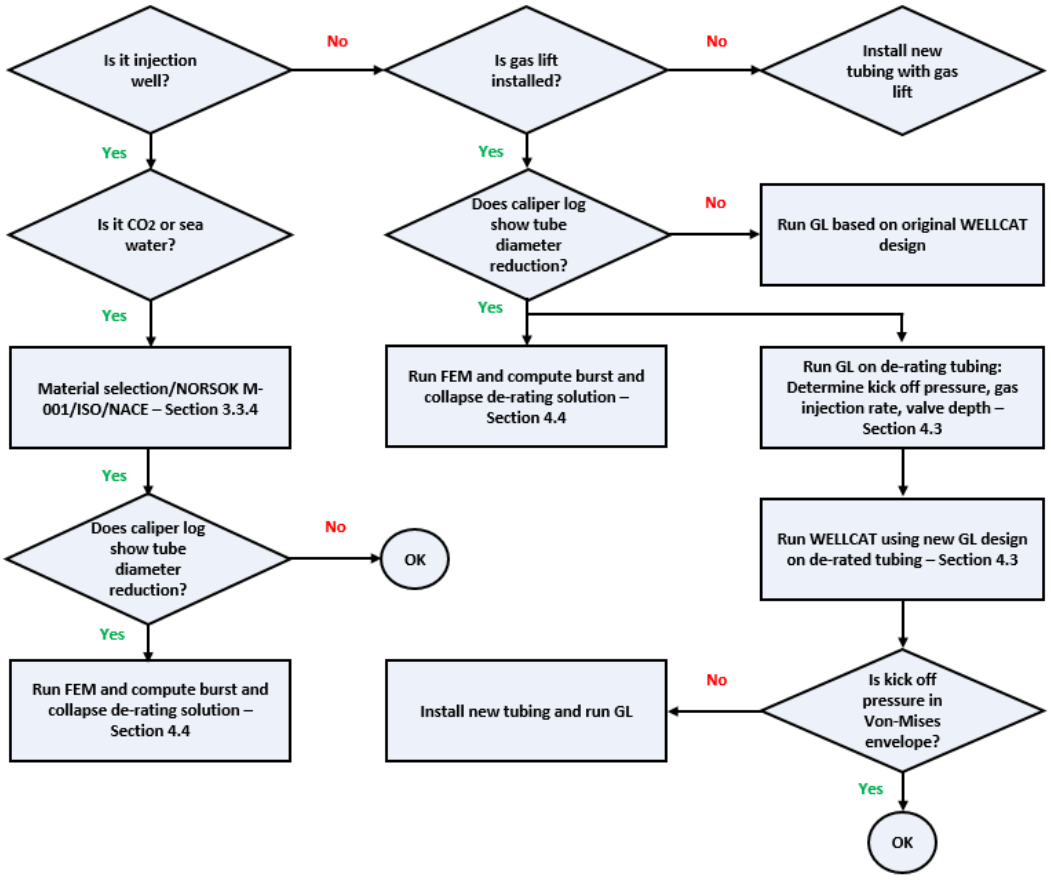

Figure 93: Illustration of the simplified workflow implemented in this thesis

5.2 Effect of Corrosion on Tubing

It is almost impossible to avoid corrosion. The most economical solution is to control the corrosion rate. Hence, a basic understanding of the corrosion process and knowledge of its main driving mechanisms is necessary. CO_2 corrosion is one of the most common types in the oil and gas industry. CO_2 can enter the well system in several ways such as CO_2 injection, sequestration, and CO_2 content in gas condensate wells. A number of different CO_2 corrosion rate prediction models have been developed and some are used as industry standards such as NORSOK M-506. A CO_2 corrosion simulation study has been performed with the objective of investigating the main sensitive parameter for the corrosion rate. In addition, the literature has documented empirical models such as DLM and DLD that are also implemented and used for the simulation study. All three models show that temperature is one of the main parameters for higher CO_2 corrosion rate. The model predictions show very similar trends below 170°F, where corrosion rate increases with temperature. However, above 170°F there is some discrepancy in the trend of the corrosion rate; it is primarily influenced by the implementation of a protective iron carbonate ($FeCO_3$) film that reduces corrosion in each model. This protective film effect is larger in the NORSOK model than in the DLM and DLD models. The NORSOK model shows that pH is the sensitive parameter for CO_2 corrosion as a slight change of pH affects the corrosion rate and the corrosion rate decreases when the pH increases. Hence, the application of pH control such as acid neutralizer products is essential to control the corrosion rate. CO_2 fugacity also plays a major role in CO_2 corrosion. In addition, CO_2 fugacity is directly proportional to CO_2 corrosion rate and thus highly influential. . CO_2 fugacity is mainly influenced by the mole percentage of CO_2, pressure, and temperature. CO_2 injection, especially when a relatively high concentration of CO_2 is used, leads to large fugacity resulting in a high corrosion rate. The NORSOK model shows that the use of an inhibitor is important to control the corrosion as it directly reduces the predicted corrosion rate.

Some important methods to control corrosion are summarized as follows:

- The use of corrosion inhibitor to control the corrosion rate
- The use of corrosion protection in the tubing by using impressed and passive currents
- The use of acid neutralizer to control pH
- An appropriate tubing design and material selection

5.3 Damaged and Undamaged Production Tubing Design with WELLCAT

The tubing design simulation using WELLCAT shows that when the tubing is damaged due to corrosion attack, it is de-rated as the nominal wall thickness decreases. The simulation results for some loadings applied show that the size of the Von-Mises envelope has a narrower window due to the lower tubing strength. It is also shown that some loadings are more sensitive with regard to the modified narrow design limits such as bullheading, pressure test tubing, and pump kill fluid. By applying a slight reduction of the tubing thickness, these loadings move relatively closer to the Von-Mises limit compared to other loadings. Hence, it is always important to check out the tubing strength limits during the production lifetime since the Von-Mises envelope changes as the tubing is de-rated. It is also necessary to continually evaluate and verify that the operational loads do not exceed the Von-Mises envelope and to adjust the new operational loads to prevent tubing failure.

5.4 Gas Lift Design for Damaged and Undamaged Production Tubing

During the production time, reservoir pressure will be depleted as the reservoir fluids are produced to the surface. The lack of natural energy in the reservoir formation has to be compensated with the artificial lift system. In this study, gas lift is designed to modify the flowing system so that the fluid can flow to the surface with a given bottom hole pressure. The design is set in unworn tubing, meaning that the gas lift is initially installed in unworn tubing that still has 100% of tubing yield strength. The same gas lift design is set in tubing with 40% wear depth based on the assumption that a corrosion attack has reduced the wear depth to 40% at the time when the pressure drop in the reservoir is too large and an artificial lift installation is needed to support the pressure. In unworn tubing, the gas lift injection pressure is set at 3500 psi with gas injection rate = 4.9 MMscf/day and the operating valve is set at 9000 ft MD. Gas lift design simulation using PROSPER shows that this initial design is within the Von-Mises envelope. When the same design is applied in tubing with 40% wear depth, WELLCAT simulation reveals that the gas lift load exceeds the Von-Mises envelope. Hence, the same injection pressure to open the gas lift operating valve in unworn tubing cannot be implemented in tubing with 40% wear depth since the de-rated tubing has lower material strength and causes tubing failure. The gas lift must be re-designed and the gas injection pressure adjusted in order to stay within the safe zone, but the production can still be optimized. In this case, the gas injection pressure is reduced to 3000 psi for tubing with 40%

wear depth. To compensate for the lower injection pressure, the gas injection rate is reduced to 3.9 MMscf/day and the operating valve is set shallower to 8000 ft. The WELLCAT simulation proves that this new gas lift design stays within the safe window. The liquid production forecast is reduced from 5179 STB/day to 4845 STB/day. This simulation study reveals how important it is to always check out tubing strength when damage such as corrosion occurs and reduces the nominal thickness of the wall. A new design of artificial lift is needed to adjust the new Von-Mises limits as the tubing strength would be lower.

5.5 FEM Damaged and Undamaged Production Tubing Modeling

The objectives of the FEM simulation study are to define at which pressure the tubing starts to yield at a given pressure loading as the tubing deteriorates for a given wear depth, to compare the tubing strength (burst and collapse) calculated by theoretical equations with the FEM simulation, and to verify if these equations can be implemented when tubing is damaged in different geometries. Two main cases are set in this simulation study: uniform corrosion and pitting corrosion. Burst and collapse are then observed for each case. In the uniform case, the wear depth is distributed consistently in the inner tubing as the corrosion attack is developed over the entire tubing surface, while in the pitting case, as the corrosion attack occurs locally, the tubing is reduced only at certain locations in the inner tubing surface.

5.5.1 Burst Case Scenario

The burst case scenario is developed based on real-world field operations such as well stimulation, fracturing, and bullheading, which forcibly apply pressure in the pipe into the formation. The constant external pressure of 2062 psi was applied to represent the hydrostatic column of completion fluid in the annulus with SG = 1.05 while the internal pressure varied. The case where Po = 0 is also simulated to get the same assumption as Barlow, which is initially derived based on an assumption of Po = 0. The loadings applied on both the inner and outer pipe are taken from the pressure at the depth where the dogleg severity is at maximum since it has been showed from some real-world cases [6] that the severest damage occurs at the maximum dogleg severity.

5.5.1.1 Summary of Uniform Corrosion Damage in the Case of Burst

- The Von-Mises stress after tubing deformation is uniformly distributed.
- Barlow gives the lowest pressure limits when external pressure is applied.
- To investigate the application of Barlow to the de-rated tubing, the same external pressure applied in Abaqus is added to Barlow (P Barlow + Po) and this new equation is well fitted to the FEM simulation.
- The Tri-axial equation is well fitted with the simulation since it takes the external pressure into account.
- In the case where Po = 0, the simulation and the equations have broadly similar trends and values in pressure.
- The FEM-based model satisfies Barlow and Tri-axial equations and these equations can be used in the uniform corrosion case.
- Figure 94 presents the burst pressure difference between the Barlow model and the FEM-based model. As wear increases from 0% to 50%, the burst pressure prediction of Barlow deviates between cases $Po \neq 0$ and $Po = 0$, and the FEM-based models increase from 2207 psi to 2520 psi and 36 psi to 359 psi, respectively. Further, the pressure differences presented in Figure 94 are converted to deviation percentages. Figure 95 shows the percentage of the burst pressure difference (deviation) between the API model and the FEM-based model. As wear increases from 0% to 50%, the deviation percentage of API Barlow differs between cases $Po \neq 0$ and $Po = 0$, such that the FEM-based model increases from 24% to 46% and 0.6% to 4%, respectively.

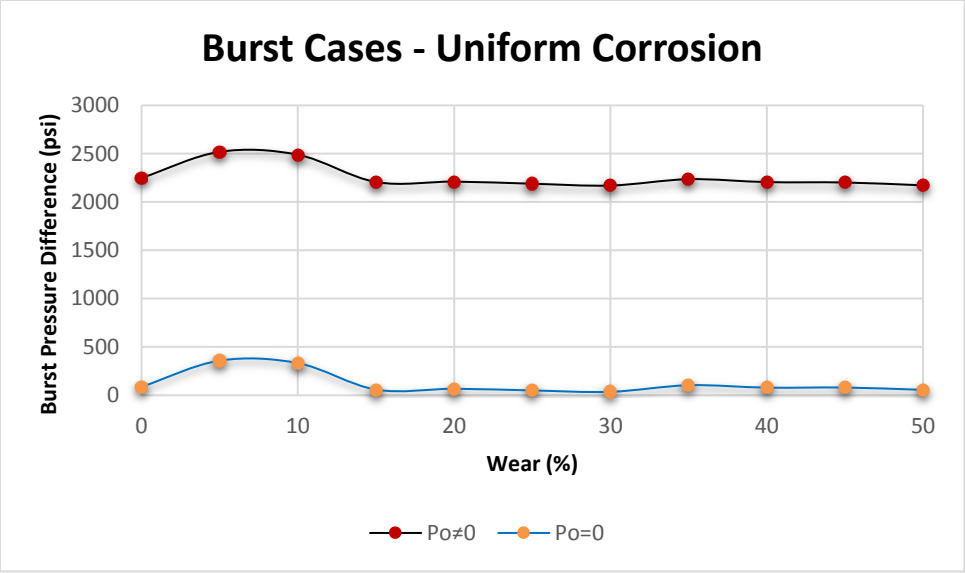

Figure 94: Burst pressure difference between Barlow model prediction and FEM based model – uniform corrosion

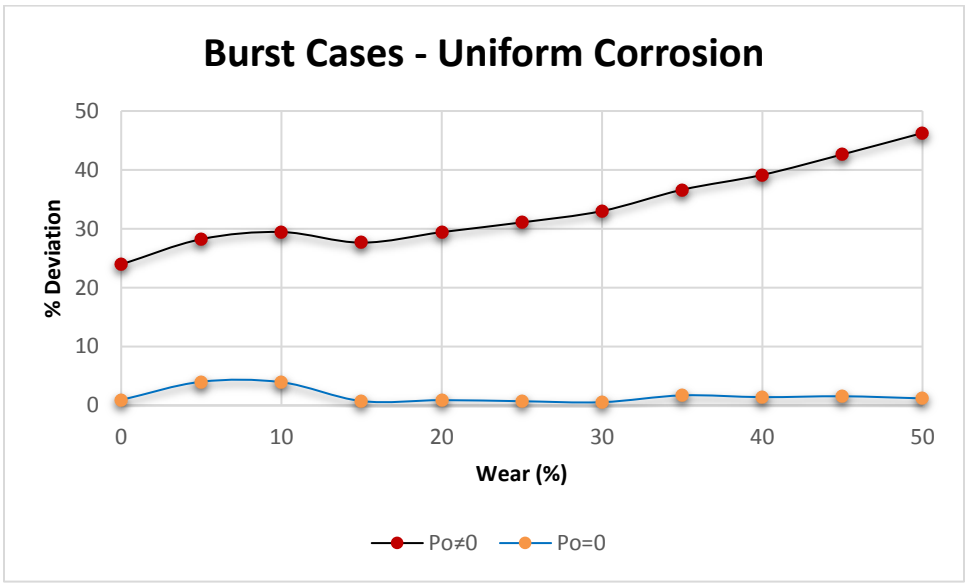

Figure 95: Deviation percentage between Barlow and FEM simulation – uniform corrosion

5.5.1.2 Summary of Pitting Corrosion Damage in the Case of Burst

- The Von-Mises stress after tubing deformation is not uniformly distributed, and the higher stress is concentrated on the specific area of local damage.

- The FEM simulation gives almost indistinguishable curves between four and eight points of damage at high wear depth (40% to 50%). At wear depth 10% to 30%, the burst limits for four points of damage are generally lower compared to eight points of damage.
- In general, the FEM-based model gives the lowest burst pressure limit. At wear depth of 50%, Barlow gives the pressure limits that are closer to the simulation results, with slightly lower values.
- In the presence of external pressure, the FEM-based model gives lower pressure than Barlow and Tri-axial. In this case, the burst limit from FEM is expected to be higher as the external pressure functions as a support pressure.
- The theoretical equations (Barlow and Tri-axial) cannot be used to estimate the burst rating when local damage occurs in the tubing.
- The FEM-based model is more applicable to predict burst limits in the pitting corrosion case since it models the real local damage geometry in the tubing.
- Figure 96 presents the burst pressure difference between the Barlow model and the FEM-based model. As wear depth increases from 10% to 50%, the burst pressure prediction of Barlow for 4 points of damage deviates between cases $Po \neq 0$ and $Po = 0$, and the FEM models increase from 234 psi to 1386 psi and 1727 psi to 3507 psi, respectively. Further, the pressure differences presented in Figure 96 are converted to deviation percentages. Figure 97 shows the percentage of the burst pressure difference (deviation) between the API model and the FEM-based model. As wear increases from 0% to 50%, the deviation percentage of API Barlow for 4 points of damage differs between cases $Po \neq 0$ and $Po = 0$, such that the FEM-based model increases from 4% to 16% and 37% to 43%, respectively. A similar trend is shown in the case of 8 points of damage, with some discrepancy at 20% wear depth.

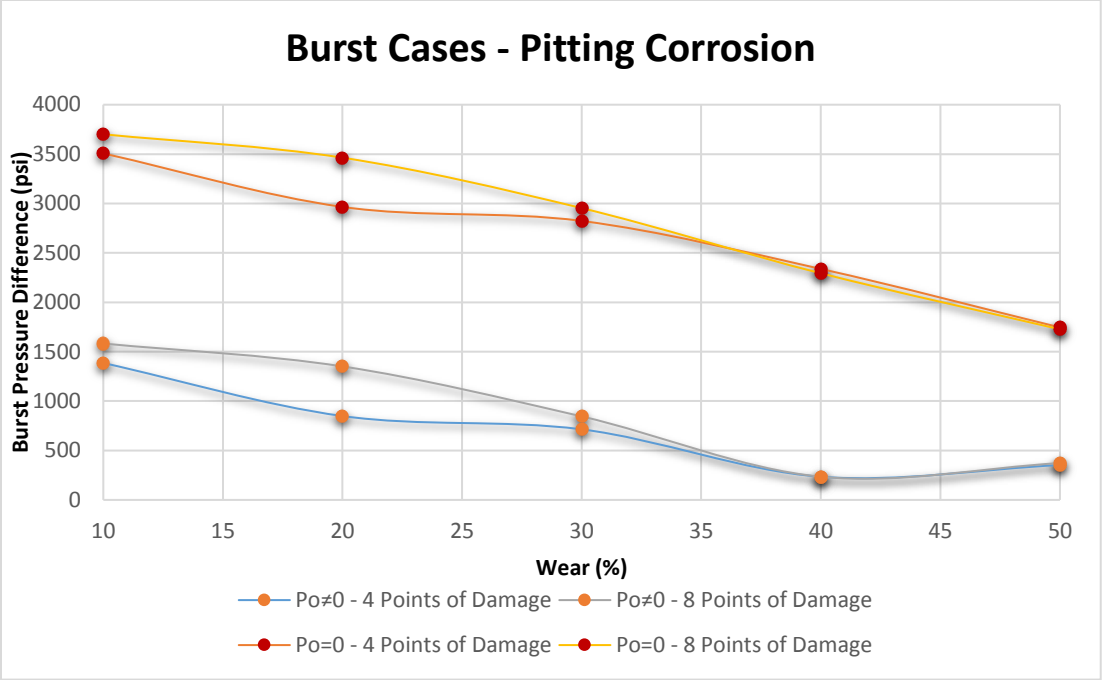

Figure 96: Burst pressure difference between Barlow model prediction and FEM-based model – pitting corrosion

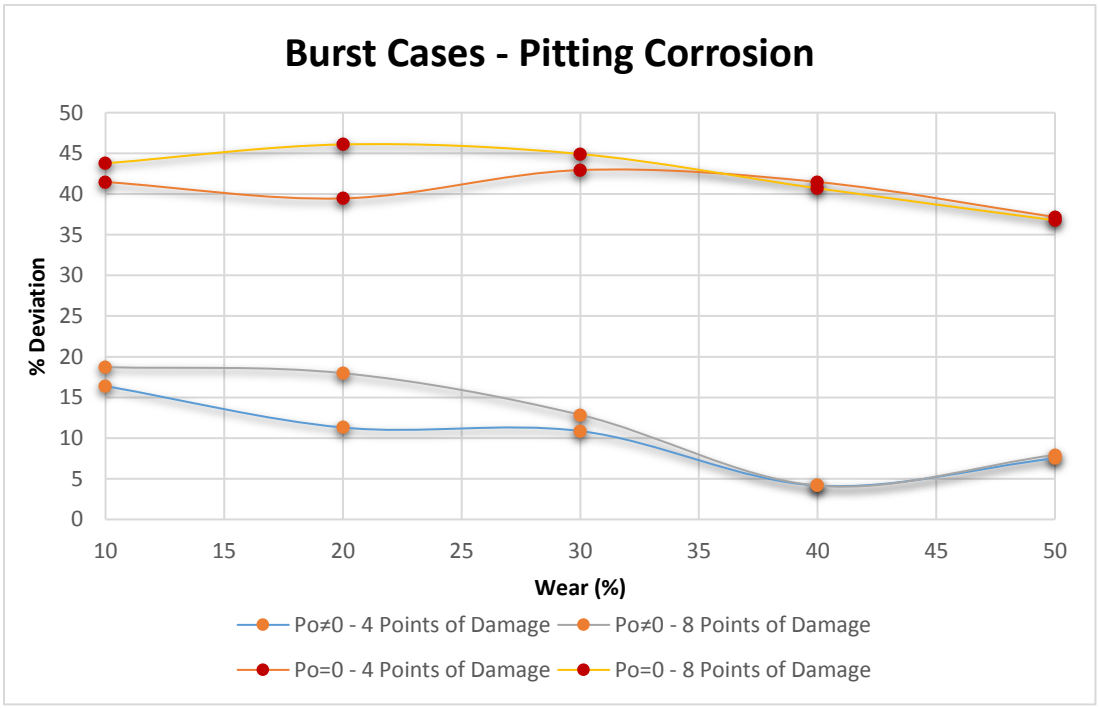

Figure 97: Deviation percentage between Barlow and FEM simulation – pitting corrosion

5.5.2 Collapse Case Scenario

The collapse case is developed based on a well that is produced with gas lift. To open the operating valve, the pump pressure has to be applied from the surface and it may develop pressure build-up in annulus-A. In the unloading gas lift process, pump pressure is also needed to evacuate the completion fluid before the gas lift can be operated. In this case, a constant internal pressure of 3758 psi is applied to represent the pressure inside the tubing filled with oil column with gradient of 0.3 psi/ft while the external pressure is varied. The case where Pi = 0 was also set to observe the worst collapse case that might happen in the well such as when it is completed with the sand screen and experiences sand face blockage during the production time. The tubing is full of gas and the wellhead is opened to atmospheric pressure, resulting in very low tubing pressure.

5.5.2.1 Summary of Uniform Corrosion Damage in the Case of Collapse

- The case where Pi = 0 is set to represent the worst collapse case that might happen in the well when the sand face blockage is occurred and the tubing is full of gas.
- The constant internal pressure of 3758 psi is exerted from the oil column with a gradient of 0.3 psi/ft.
- The Von-Mises stress after tubing deformation is uniformly distributed.
- The FEM-based model gives higher pressure limits compared to the API collapse equation.
- The Tri-axial equation is better fitted to the FEM simulation since it takes the internal pressure into account.
- In the case where Pi $\neq$ 0, the gap between the API collapse equation and the FEM simulation is larger since there is no internal pressure as a support pressure.
- The API equation gives the lowest burst pressure limits and narrowest safety window.
- The FEM simulation-based model seems to be more realistic since it takes into account both external and internal pressure, while the API collapse equation is only based on tubing geometry.
- In the real world, FEM simulation is more applicable since it takes into account both internal and external loadings.

- Figure 98 presents the collapse pressure difference between the API model and the FEM-based model. As wear increases from 0% to 50%, the collapse pressure predictions of API deviate between cases Pi ≠ 0 and Pi = 0, such that the FEM models increase from 2610 psi to 3877 psi and 2349 psi to 3747 psi, respectively. Further, the pressure differences presented in Figure 98 are converted to deviation percentages. Figure 99 shows the percentage of the collapse pressure difference (deviation) between the API model and the FEM-based model. As wear increases from 0% to 50%, the deviation percentage of API differs between cases Pi ≠ 0 and Pi = 0, such that the FEM-based model increases from 35% to 82% and 35% to 354%, respectively.

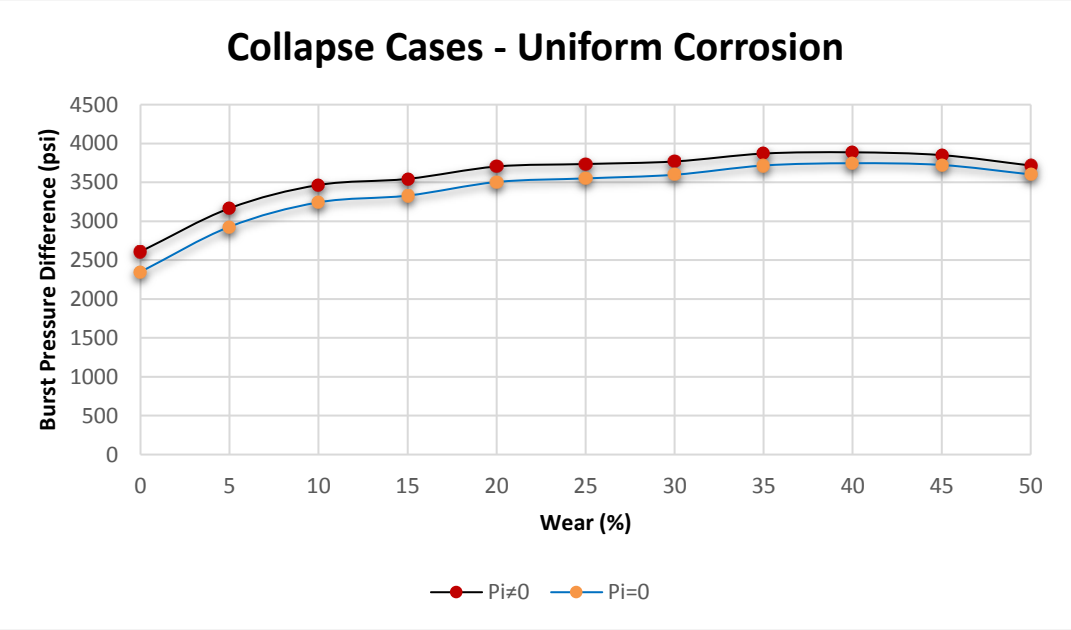

Figure 98: Collapse pressure difference between API model prediction and FEM-based model – uniform corrosion

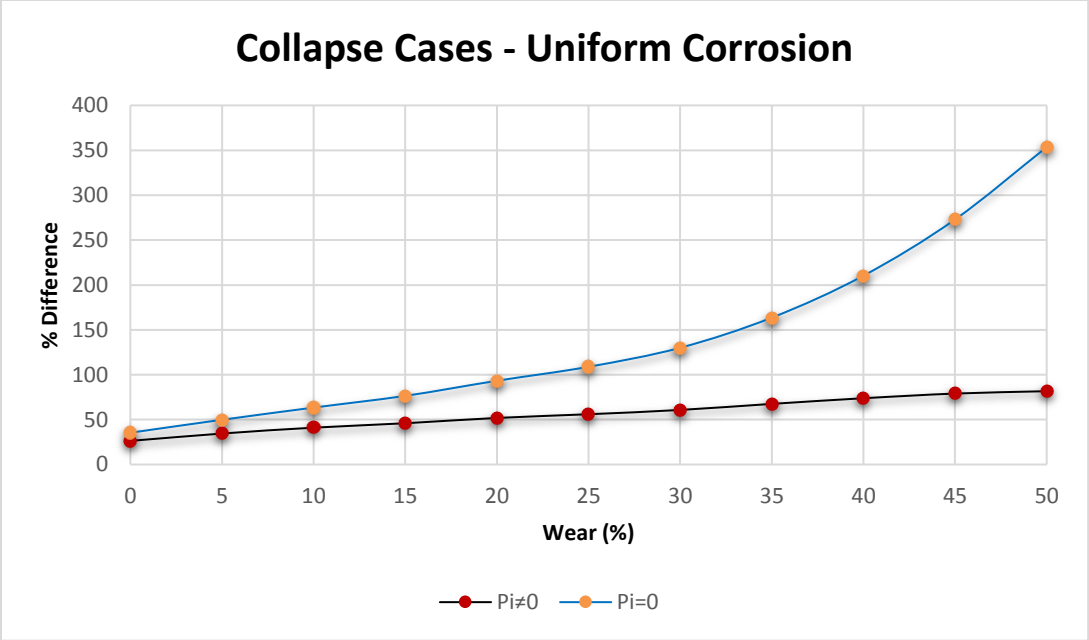

Figure 99: Deviation percentage between API model and FEM simulation – uniform corrosion

5.5.2.2 Summary of Pitting Corrosion Damage in the Case of Collapse

- The Von-Mises stress after tubing damage is not uniformly distributed, and the higher stress is concentrated in the specific area of local damage.
- The API equation shows the lowest burst rating, while Tri-axial shows the highest value.
- The theoretical equations (API collapse and Tri-axial equations) cannot be used to estimate the collapse rating when local damage has occurred in the tubing.
- The FEM-based model is more applicable to predict collapse limits in the case of pitting corrosion since it models the real local damage in the tubing.
- Figure 100 presents the burst pressure difference between the API model and the FEM-based model. As wear increases from 10% to 50%, the burst pressure predictions of API for the 4 points of damage deviate between cases Pi ≠ 0 and Pi = 0, and the FEM models increase from 2383 psi to 3635 psi and 597 psi to 1896 psi, respectively. Further, the pressure differences presented in Figure 100 are converted to deviation percentages. Figure 101 shows the percentage of the collapse pressure difference (deviation) between the API model and the FEM-based model. As wear increases from 0% to 50%, the deviation percentage of API for the 4 points of damage differs from case Pi ≠ 0 and Pi= 0, such that

the FEM-based model increases from 36% to 123% and 10% to 186%, respectively. A similar trend is shown in the case of 8 points of damage, with some discrepancy at 20% wear depth.

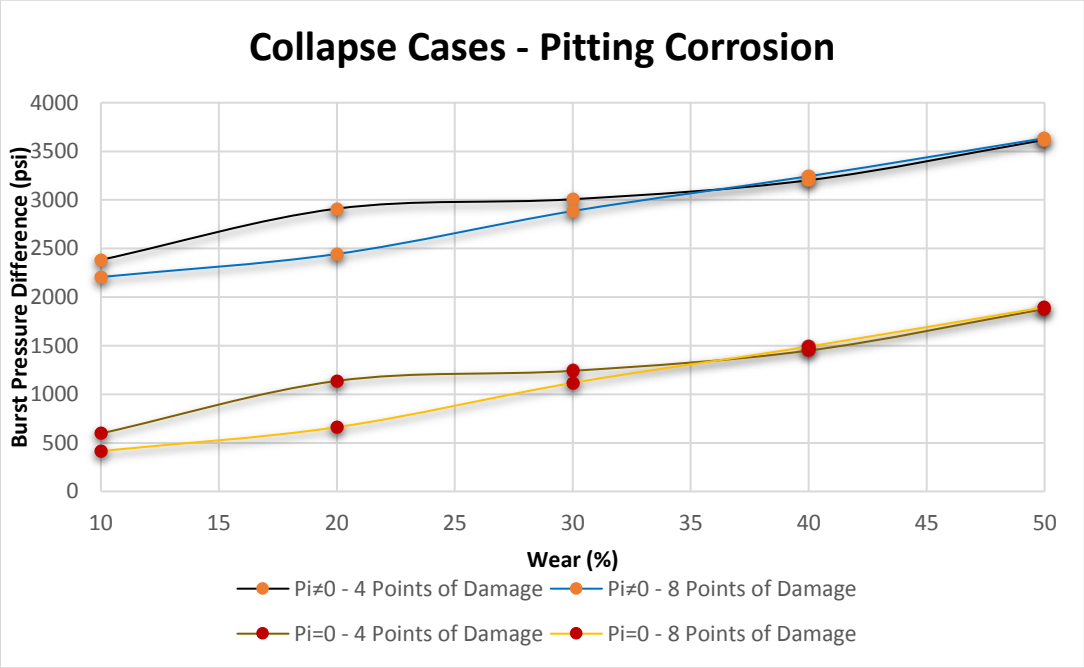

Figure 100: Collapse pressure difference between API model prediction and FEM based model – pitting corrosion

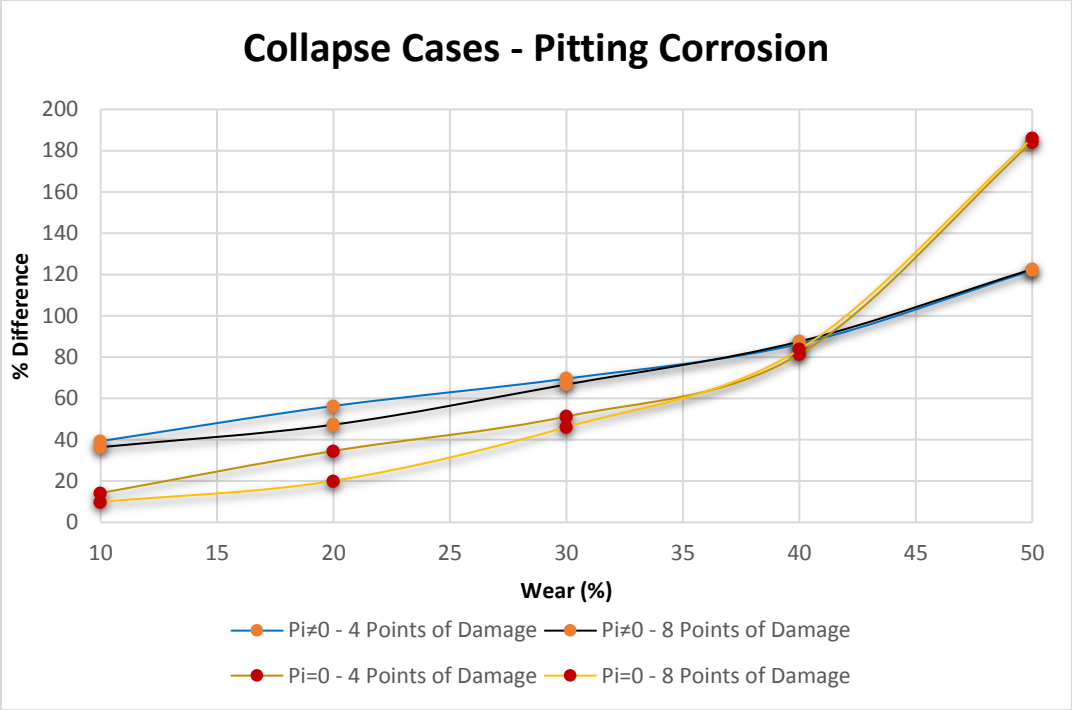

Figure 101: Deviation percentage between API model and FEM simulation – pitting corrosion

Conclusion

Since corrosion can cause significant damage to the tubing material, it is important to have a basic understanding of the main parameters that enhance corrosion. Preventative actions need to be applied to control the corrosion rates in order to minimize the operating cost. Some empirical models have been developed to predict CO_2 corrosion that can help the industry to estimate and control the corrosion rates.

Corrosion damage can lead to the deterioration of tubing. A WELLCAT simulation shows that in de-rated tubing, the Von-Mises envelope changes, resulting in lower material strength. These changes in tubing strength must be checked regularly, especially when some operational loadings are applied and the artificial lift method is installed since the tubing strength is lowered. The artificial lift must be re-designed to adjust to the loading parameters and stay within the Von-Mises envelope.

FEM simulation results show a good method to model any arbitrarily shaped damage and predict the de-rated burst/collapse load carry capacity of the tubing.

Based on the overall simulation studies that have been carried out, that the following conclusions are presented:

1. The main parameters that control CO_2 corrosion rate are temperature, pH, and CO_2 fugacity. It is observed that that the critical temperature point associated with the higher corrosion rate is at 170°F. Above this point, a protective film of iron carbonate is formed and reduces the corrosion.
2. The highest corrosion expense by activity in the oil production field comes from inhibitor treatment, which requires more than 70% of costs. The simulation results illustrate that the addition of sufficient inhibitor reduced the corrosion rate by forming a temporary protective layer on the damaged part of the tubing.
3. Inspection of tubing condition [6] shows that during the life of the production, tubing will be damaged by mechanical means or corrosion. This will reduce the tubing strength. It is therefore

important to re-simulate the tubing based on the damage and determine the de-rated loadings which would be within the newly modified allowable Von-Mises envelope.

4. When tubing is de-rated in a gas lift well, the gas lift must be re-designed and the new injection pressure set within the updated Von-Mises envelope.
5. Uniform corrosion and pitting corrosion reduce the strength of tubing material. The stress distributions in the FEM-based model show different results as follows:
    a. In *uniform corrosion damage*, the stress is distributed uniformly.
    b. In *pitting corrosion damage*, the stress is not distributed uniformly, with the highest stress concentration localized at the damaged part of the tubing.
6. When the external pressure is zero (Po = 0), the application of API Barlow equation for uniform corrosion is validated by FEM simulation. Therefore, the API burst model works only if the inner size of the tube is uniformly reduced and continuum mechanics can be applied.
7. On the other hand, in the presence of external pressure, the FEM-based burst pressure load equals the burst pressure determined by API Barlow pressure plus external pressure (P Barlow + Po).
8. In the collapse case, the API collapse equation shows a lower collapse pressure prediction than the FEM model. This result does not match the FEM-based model result in the presence of internal pressure. In the absence of internal pressure, there is a big deviation.
9. The Tri-axial analytical solution in the case of uniform corrosion is valid for both burst and collapse cases and is verified by the FEM-based model.
10. The Barlow and Tri-axial equations cannot be applied to predict burst pressure in the pitting corrosion case. The main reason for this is that these models are derived from continuum mechanics and pitting corrosion damage is more relevant to fracture mechanics. However, at this time, the author was unable to find any documentation of an analytical model being used to predict de-rating loading in pitting damage. From this thesis research work, the author believes that FEM modeling is a very reliable method for any types of damage.
11. Likewise, the API model and the Tri-axial equation cannot be applied to predict collapse pressure in the case of pitting corrosion.

References

1. NORSOK Standard D-010. 2013. *Well Integrity in Drilling and Well Operations*. Rev 3. Standards Norway, Norway, 221 pp.
2. Agonafir, M, B. 2016. *Corrosion and Prevention (Control) Methods*. Unpublished Internal Document, University of Stavanger, Norway, 35 pp.
3. Gerhardus, H., Brongers, M, P, H., Koch, P, J, H., Thompson, N, G., and Virmani, Y, P. 2002. *Corrosion Costs and Preventive Strategies in The United States*. National Association of Corrosion Engineers International Series. Houston, Texas, 12 pp. Available from: https://www.nace.org/uploadedFiles/Publications/ccsupp.pdf, 01.05.2017.
4. Vignes, B., and Aadnøy, B, S. 2010. *Well-Integrity Issues Offshore Norway*. SPE Production and Operations. Society of Petroleum Engineers, pp. 145-150.
5. Vu, T. 2015. *Finite Element Method Simulation and Modeling of Tubing Wear*. Master Thesis, University of Stavanger, Stavanger.
6. ConocoPhillips A. *Pressefoto*. Available from: http://www.conocophillips.no/NO/newsroom/Sider/press-photos.aspx, 20.04.2015.
7. Agonafir, M, B. 2016. *Grading, Tube Stress, and Failure Analysis*. Unpublished Internal Document, University of Stavanger, Norway, 77 pp.
8. Labossiere, P, E. 2017. *Thin-walled Pressure Vessels*. University of Washington, Washington. Available from: http://courses.washington.edu/me354a/Thin%20Walled%20Pressure%20vessels.pdf, 10.07.2017.
9. Bellarby, J. 2009. *Well Completion Design*. Elsevier. Amsterdam.
10. Aadnoy, B, S. 2010. *Modern Well Design*. CRC Press. Norway.
11. API Bulletin 5C3. 1994. *Bulletin on Formulas and Calculations for Casing, Tubing, Drill Pipe, and Line Pipe Properties.* 6th edition American Petroleum Institute, Washington, USA.
12. De Weck, O., and Kim, I, Y. 2004. *Finite Element Method*. Massachusetts Institute of Technology. 26 pp. Available from:

http://web.mit.edu/16.810/www/16.810_L4_CAE.pdf, 10.05.2017.

13. Felippa, C, A. 2014. *Chapter 6 - Finite Element Modeling: Introduction*. Available from: http://www.colorado.edu/engineering/CAS/courses.d/IFEM.d/, 06.05.2017.
14. COMSOL. 2017. Available from: https://www.comsol.no/multiphysics/finite-element-method, 15.06.2016.
15. Tawfik, Mohammad. 2010. *Introduction to The Finite Element Method*. Available from: https://www.slideshare.net/mohammadtawfik/an-introduction-to-the-finite-element-method, 29.05.2017.
16. Cook, R, D., Malkus, D, S., Plesha, M, E., and Witt, R, J. 2007. *Concepts and Applications of Finite Element Analysis*: John Wiley & Sons. United States.
17. Holm, Haavard. 2017. *The Finite Element Method – Theory*. Norwegian University of Science and Technology. Available from: http://illustrations.marin.ntnu.no/structures/analysis/FEM/theory/index.html, 05.06.2017.
18. Corrosion College. *Electrical Conduit Corrosion*. Available from: https://corrosioncollege.com/white-paper.cfm, 15.05.2017.
19. Baxter, R., and Britton, J. 2013. *Offshore Cathodic Protection 101: What It Is and How It Works*. Deepwater Corrosion Services. Available from: http://www.cathodicprotection101.com/, 12.05.2017.
20. NORSOK Standard M-001. 2004. *Materials Selection*. Rev 4. Standards Norway, Norway, 30 pp.
21. Agonafir, M, B. 2016. *Materials and Material Selection*. Unpublished Internal Document, University of Stavanger, Norway, 35 pp.
22. Corrosion Consulting Services. *Different Types of Corrosion*. Available from: http://www.corrosionclinic.com/types_of_corrosion/uniform_corrosion.htm, 20.04.2017.
23. Rothwell, N., and Tullmin, M. 2000. *The Corrosion Monitoring Handbook*. Coxmoor Publ. Co. Oxford, 180 pp.
24. NACE International. 2017. *Pitting Corrosion*. Available from: https://www.nace.org/Pitting-Corrosion/, 04.05.2017.
25. Ogden, B, L. 2005. *Sulfide Stress Cracking-Practical Application to the Oil and Gas Industry*. Texas Tech University, 34 pp.
26. Total Materia. 2014. *Hydrogen Sulfide Corrosion*. Available from:

http://www.totalmateria.com/page.aspx?ID=CheckArticle&site=kts&NM=424, 01.05.2017.

27. Kermani, M, B., and Morshed, A. 2003. *Carbon Dioxide Corrosion in Oil and Gas Production - A Compendium*. Corrosion – The Journal of Science and Engineering. Vol. 59, No. 8, pp. 659-683. DOI: 10.5006/1.3277596
28. Iannuzzi, M. 2014. *Carbon Dioxide – Definition. About Corrosion*. Available from: https://www.aboutcorrosion.com/2014/11/12/carbon-dioxide-corrosion-definition/, 02.05.2017.
29. Murray, A, S., and Holman, W, E. 1967. *Drilling String Corrosion - A Major Drilling Problem*. Journal of Canadian Petroleum Technology. Petroleum Society of Canada. DOI: 10.2118/67-02-01
30. Petrowiki. 2017. *Nanotechnology in Hydrogen Sulfide Detection*. Available from: http://petrowiki.org/Nanotechnology_in_hydrogen_sulfide_detection, 18.04.2017.
31. Goodnight, R, H., and Barret, J, P. 1956. *Oil-Well Casing Corrosion*. Drilling and Production Practice. American Petroleum Institute. New York.
32. Poetker, R, H., and Stone, J, D. 1956. *Corrosion Control of Gas-Lift Wells*. Drilling and Production Practice. American Petroleum Institute. New York, pp. 414-423.
33. Weatherford. 2016. *Basic Concepts of Sucker Rod Corrosion*. Available from: http://www.weatherford.com/doc/wft306981, 08.06.2017.
34. NORSOK Standard M-506. 2005. *CO_2 Corrosion Rate Calculation Model*. Standards Norway, Norway, 15 pp.
35. Woollam, R, C., and Hernandez, S. 2006. *Assessment and Comparison of CO_2 Corrosion Predicition Models*. SPE International Oilfield Corrosion Symposium. Society of Petroleum Engineers, 9 pp. DOI: 10.2118/100673-MS
36. Olsen, S. 2003. *CO_2 Corrosion Prediction by Use of the NORSOK M-506 Model - Guidelines and Limitations*. National Association of Corrosion Engineers International Series. Houston, Texas, 12 pp.
37. De Waard, C, and Milliams, D. 1975. *Prediction of Carbonic Acid Corrosion in Natural Gas Pipelines.* First International Conference on The Internal and External Protection of Pipes, pp. 24-26.

38. De Waard, C., Lotz, U., and Milliams, D. 1991. *Predictive Model for CO2 Corrosion Engineering in Wet Natural Gas Pipelines*. Volume 47, Issue 12, pp. 976-985.
39. Hansen, D. 1996. *Materials Selection for Hydrocarbon and Chemical Plants*. Marcel Dekker, Inc. New York.
40. De Waard, C., and Lotz, U. 1993. *Prediction of CO_2 Corrosion of Carbon Steel.* National Association of Corrosion Engineers International Series. Houston, Texas.
41. De Waard, C., Lotz, U., and Dugstad, A. 1995. *Influence of Liquid Velocity on CO_2 Corrosion*: *A Semi-Empirical Model*. National Association of Corrosion Engineers International Series. Houston, Texas.
42. Nyborg, R. 2010. *CO_2 Corrosion Models For Oil And Gas Production Systems*. National Association of Corrosion Engineers International Series. Houston, Texas, 20 pp.
43. Sun, W., Chokshi, K., Nesic, S., and Gulino, D, A. 2004. *A Study of Protective Iron Carbonate Scale Formation in CO_2 Corrosion*. *AIChE, Austin, Texas*. Unpublished Internal Document, Ohio University, Athens.
44. Nyborg, R. 2002. *Overview of CO_2 Corrosion Models for Wells and Pipelines.* National Association of Corrosion Engineers International Series. Houston, Texas, 16 pp.
45. Shreir, L, L., Jarman, R, A., and Burstein, G, T. 1978. *Metal, Environment Reactions*. Newnes-Butterworths. London.
46. Economides, M, J., Hill, A, D., Ehlig-Economides, C., and Zhu, D. 2012. *Petroleum Production Systems*. Pearson Education. United States.

Appendix A – Well Data and Collapse Pressure Data

Well Data

Table A1: Well Survey Data

Date-Entry Mode	MD (ft)	INC (^{0})	AZ (^{0})	TVD (ft)	DLS (^{0}/100 ft)	Max DLS (^{0}/100 ft)	V Section (ft)	Departure (ft)
MD-INC-AZ	0	0	0	0			0	0
MD-INC-AZ	2500	0	0	2500	0	0	0	0
INC-AZ-DLS	4750	45	0	4525.7	2	2	839.1	839.1
MD-INC-AZ	13000	45	0	10359.3	0	0	6672.7	6672.7

Collapse Pressure Based on API 5C3 Equation

Table A2 : Collapse model [9]

Grade (ksi)	Elastic Collapse (D/t)	Transitional Collapse (D/t)	Plastic Collapse (D/t)	Yield Collapse (D/t)
40	> 42.64	27.01 - 42.64	16.40 - 27.01	< 16.40
55	> 37.21	25.01 - 37.21	14.81 - 25.01	< 14.81
80	> 31.02	22.47 - 31.02	13.38 - 22.47	< 13.38
90	> 29.18	21.69 - 29.18	13.01 - 21.69	< 13.01
95	> 28.36	21.33 - 28.36	12.85 - 21.33	< 12.85
110	> 26.22	20.41 - 26.22	12.44 - 20.41	< 12.44
125	> 24.46	19.63 - 24.46	12.11 - 19.63	< 12.11
140	> 22.98	18.97 - 22.98	11.84 - 18.97	< 11.84
155	> 21.70	18.37 - 21.70	11.59 - 18.37	< 11.59

Table A3: Plastic collapse factors [9]

Grade (ksi)	A	B	C
40	2.95	0.0465	754
55	2.991	0.0541	1206
80	3.071	0.0667	1955
90	3.106	0.0718	2254
95	3.124	0.0743	2404
110	3.181	0.0819	2852
125	3.239	0.0895	3301
140	3.297	0.0971	3751
155	3.356	0.1047	4204

Table A4: Transitional collapse factors [9]

Grade (ksi)	F	G
40	2.063	0.0325
55	1.989	0.036
80	1.998	0.0434
90	2.017	0.0466
95	2.029	0.0482
110	2.053	0.0515
125	2.106	0.0582
140	2.146	0.0632
155	2.188	0.0683

Appendix B – Pitting Corrosion Model

Example: Calculation of minimum wall thickness after tubing is extruded in the case of pitting corrosion.

Find the minimum wall thickness for tubing with 10% wear depth with four points of damage.

Before building the local damage due to pitting corrosion in Abaqus CAE, X and Y coordinates for points of damage have to be defined. The calculation of coordinate positions is summarized as follows:

Unworn tubing data:
OD tubing = 4.000 in
ID tubing = 3.548 in
Nominal wall thickness = 0.226 in

Coordinate positions in Abaqus CAE:
Unworn tubing coordinates:

	X	Y
Center	0	0
OD tubing	0	4.000
ID tubing	0	3.548

Pitting damage coordinates:

	X	Y
Pitting damage position 1	3.548	0
	(3.548+0.226) = 3.571	0
Pitting damage position 2	0	-3.548
	0	-3.571
Pitting damage position 3	-3.548	0
	-3.571	0
Pitting damage position 4	0	3.548
	0	3.571

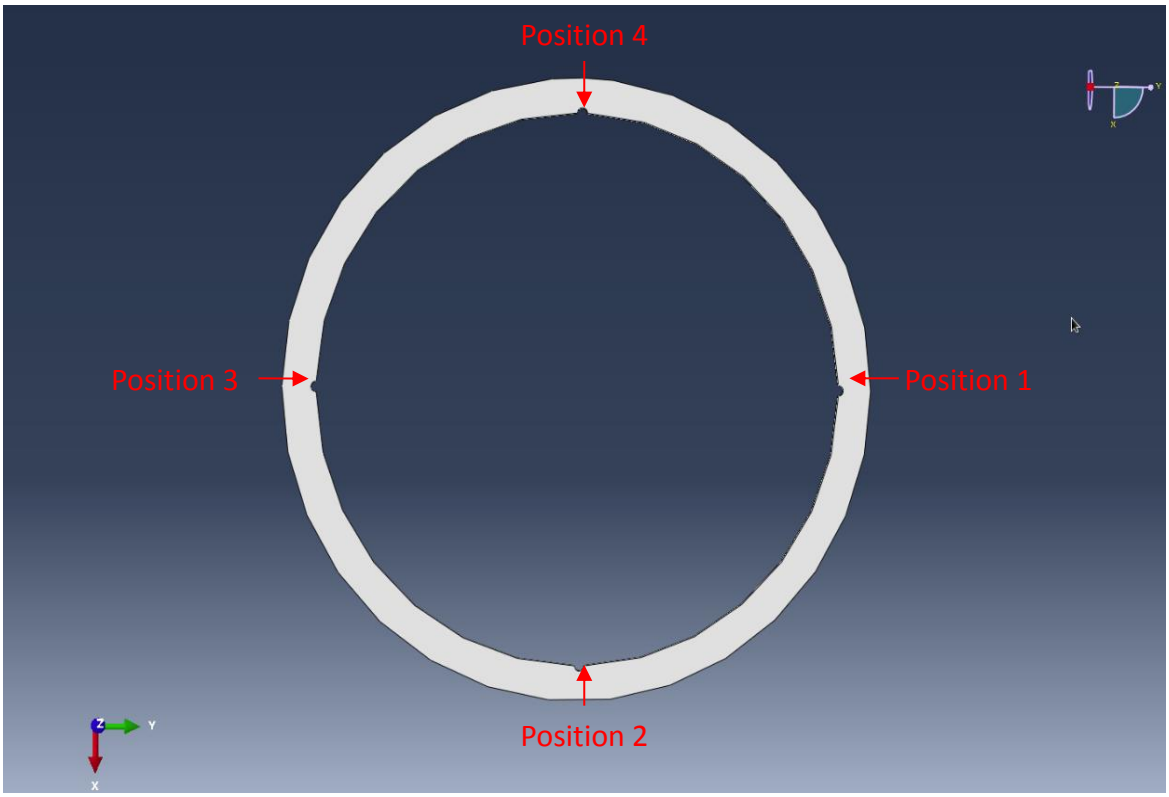

Figure B1: Tubing geometry modeling for pitting corrosion

Thickness reduction of 10% wear depth = 10% x 0.226 in = 0.0226 in

Minimum wall thickness for local damage = 0.226 in – 0.0226 in = 0.2034 in

Minimum ID tubing for local damage = 4 in – (2 x 0.2034 in) = 3.593 in

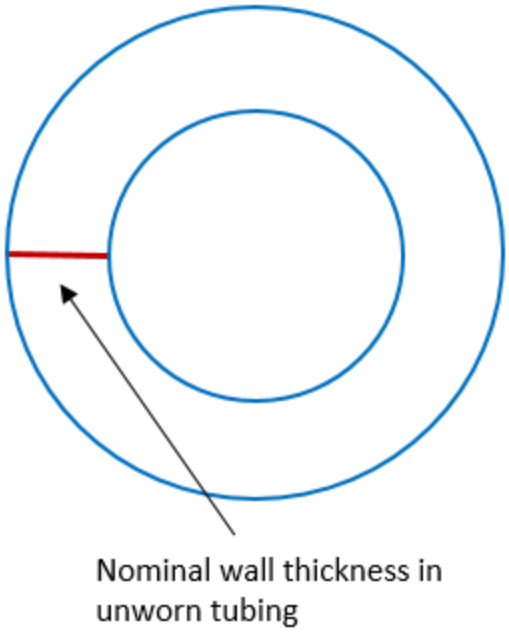

Figure B2: Nominal wall thickness in unworn tubing

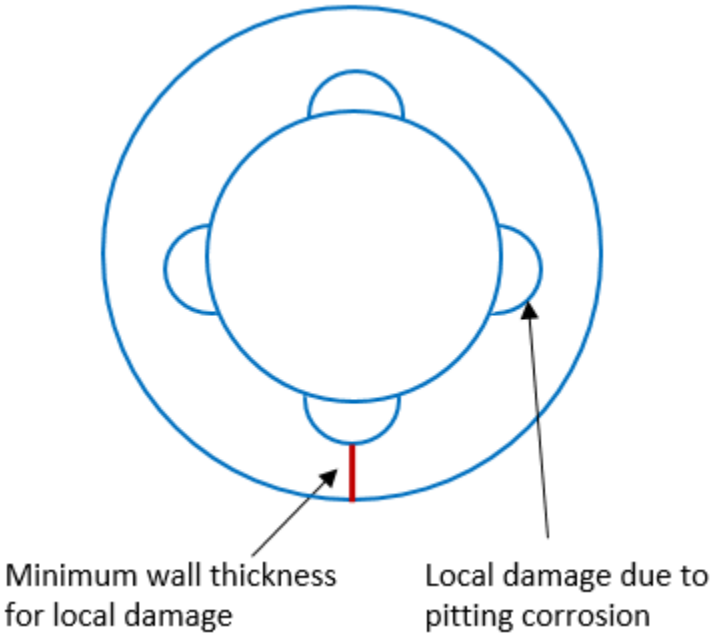

Figure B3: Minimum wall thickness in pitting corrosion

Appendix C - FEM Simulation Results (Graphs and Tables)

Uniform Corrosion – Burst Case (Po = 0)

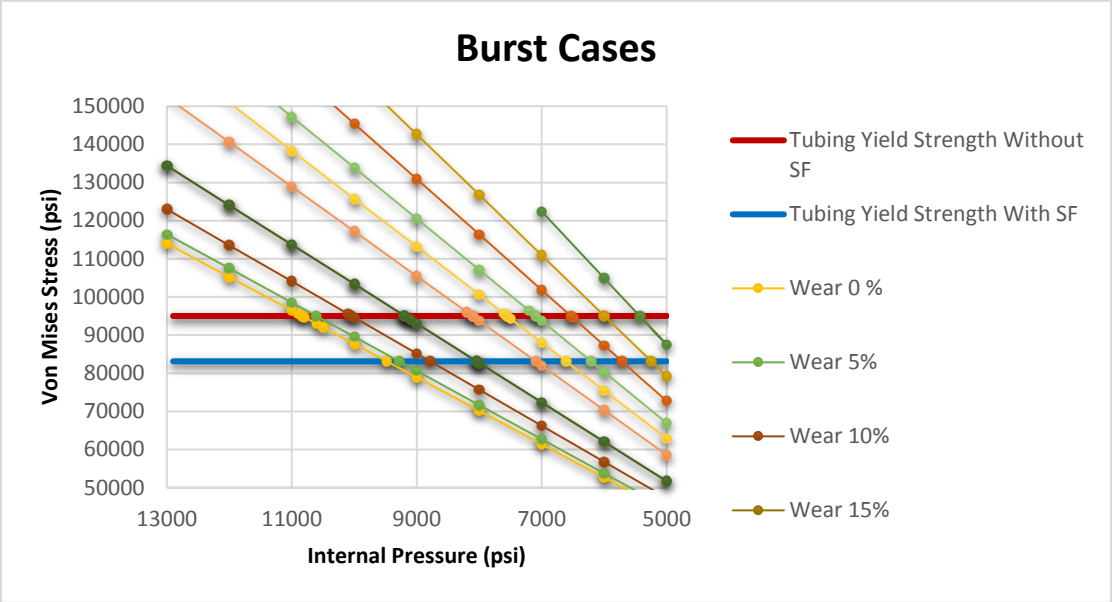

Figure C1: Burst pressure limits for 0-50% wear depth – Po = 0

Table C1: The intersection points between σ_{VME} and σy for 0-50% wear at Po = 0

Wear (%)	Von Mises Stress from Abaqus CAE Simulation (psi)	
	σy=95000 psi	σy=83125 psi
0	10834	9481
5	10606	9282
10	10043	8787
15	9192	8043
20	8665	7582
25	8109	7095
30	7556	6611
35	7097	6210
40	6532	5715
45	5996	5247
50	5432	4753

Table C2: Calculation of burst pressure vs. simulation for Po = 0

Wear (%)	Remarks	Burst Pressure from Equation (psi)		Burst Pressure from Simulation (psi)
		Barlow	Tri-axial	Abaqus
0	Thick-walled	9393	9317	9481
5	Thick-walled	8923	8858	9282
10	Thick-walled	8454	8399	8787
15	Thick-walled	7984	7938	8043
20	Thin-walled	7515	7476	7582
25	Thin-walled	7045	7013	7095
30	Thin-walled	6575	6549	6611
35	Thin-walled	6106	6085	6210
40	Thin-walled	5636	5620	5715
45	Thin-walled	5166	5154	5247
50	Thin-walled	4697	4687	4753

Uniform Corrosion – Collapse Case (Pi ≠ 0)

Table C3: Abaqus CAE simulation results for unworn tubing – collapse case

Internal Pressure (psi)	External Pressure (psi)	Von Mises Stress (psi)
3758	5000	13810
3758	6000	22910
3758	7000	32090
3758	8000	41300
3758	9000	50520
3758	10000	59750
3758	11000	68980
3758	12000	78220
3758	**12531**	**83125**
3758	13000	87460
3758	**13816**	**95000**
3758	14000	96700
3758	15000	105900

Table C4: Abaqus CAE simulation results for 5% wear – collapse case

Internal Pressure (psi)	External Pressure (psi)	Von Mises Stress (psi)
3758	5000	14050
3758	6000	23340
3758	7000	32710
3758	8000	42110
3758	9000	51530
3758	10000	60950
3758	11000	70380
3758	12000	79800
3758	**12353**	**83125**
3758	13000	89230
3758	**13612**	**95000**
3758	14000	98660
3758	15000	108100

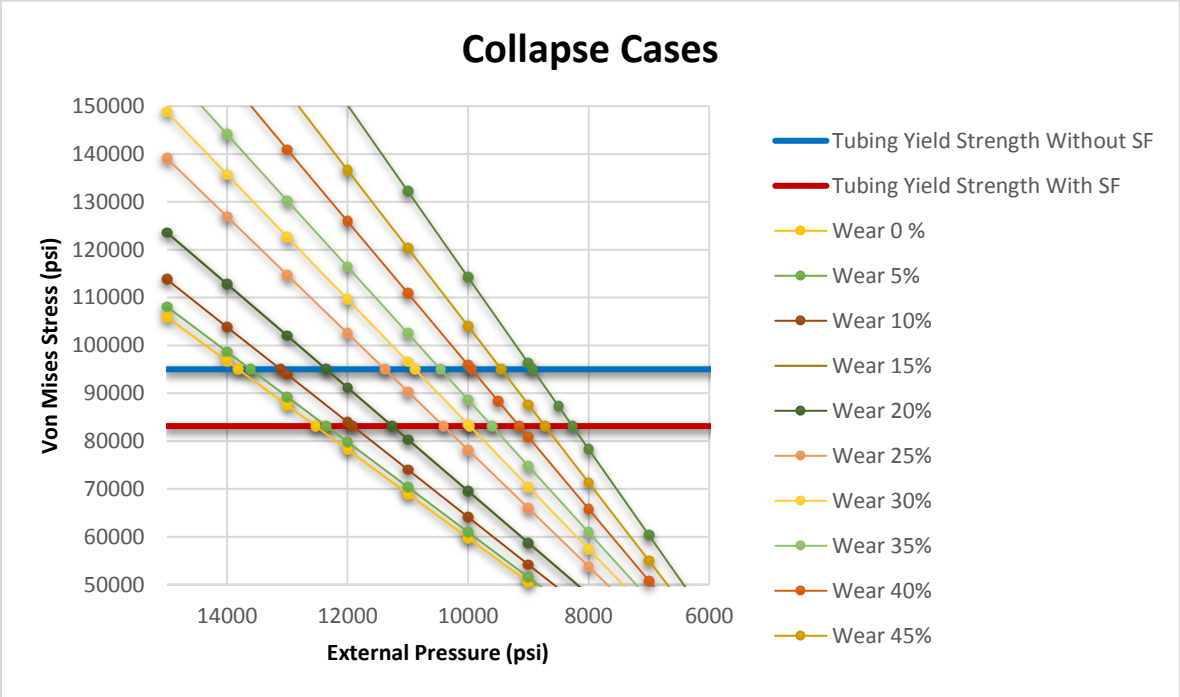

Figure C2: Collapse pressure limits for 0-50%Wear at Pi ≠ 0 – collapse case

Table C5: The intersection points between σ_{VME} and σy for 0-50%w at Pi ≠ 0 – collapse case

Wear (%)	Von Mises Stress from Abaqus CAE Simulation (psi)	
	σ_y = 95000 psi	σ_y = 83125 psi
0	13816	12531
5	13612	12353
10	13111	11916
15	12355	11259
20	11885	10846
25	11384	10409
30	10882	9972
35	10460	9604
40	9943	9153
45	9450	8724
50	8930	8269

Uniform Corrosion – Collapse Case (Pi = 0)

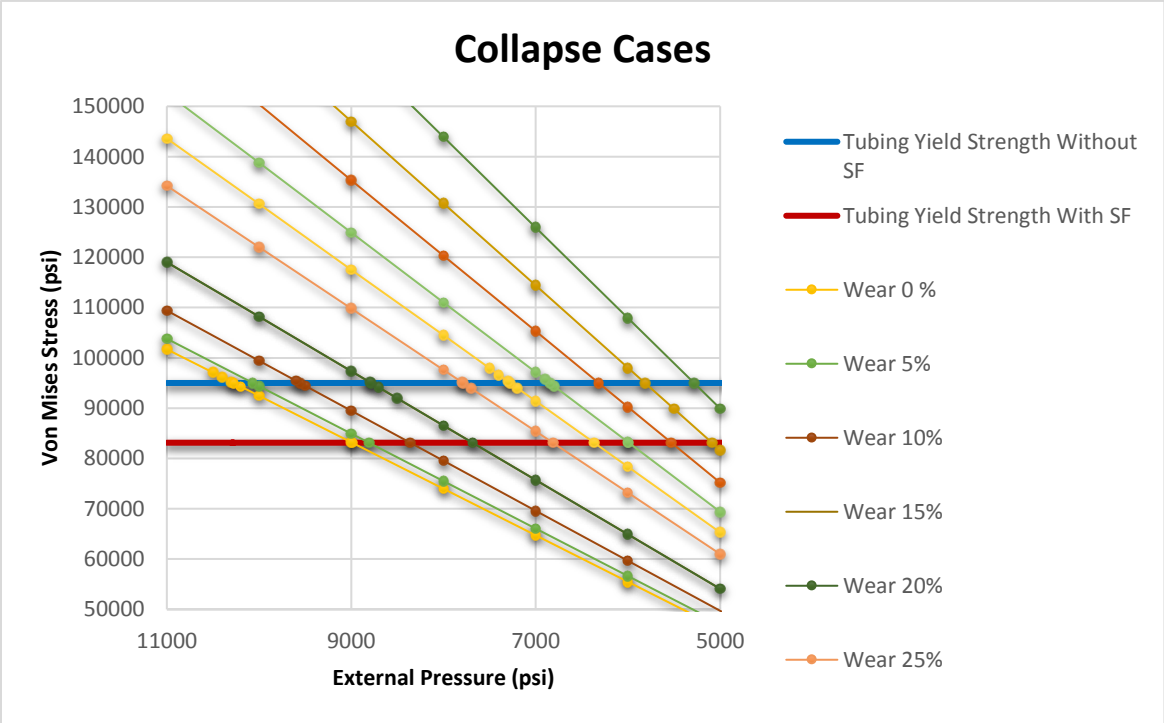

Figure C3: Collapse pressure limits for 0-50% wear – Pi = 0

Table C6: The intersection points between σ_{VME} and σy for 0-50% wear at Pi = 0

Wear (%)	Von Mises Stress from Abaqus CAE Simulation (psi)	
	σ_y = 95000 psi	σ_y = 83125 psi
0	13816	8991
5	13612	8809
10	13111	8361
15	12355	7685
20	11885	7263
25	11384	6814
30	10882	6366
35	10460	5990
40	9943	5528
45	9450	5088
50	8930	4622

Table C7: Calculation of collapse pressure vs. simulation – Pi = 0

Wear (%)	Cylinder Type	D/t	Collapse Type	Collapse Pressure from Equation (psi)		Collapse Pressure from Simulation (psi)
				API	Tri-axial	Abaqus
0	Thick-walled	17.7	Plastic Collapse	6641	8862	8991
5	Thick-walled	18.6	Plastic Collapse	5879	8445	8809
10	Thick-walled	19.7	Plastic Collapse	5117	8024	8361
15	Thick-walled	20.8	Plastic Collapse	4355	7601	7685
20	Thin-walled	22.1	Transitional Collapse	3758	7175	7263
25	Thin-walled	23.6	Transitional Collapse	3263	6746	6814
30	Thin-walled	25.3	Transitional Collapse	2768	6315	6366
35	Thin-walled	27.2	Transitional Collapse	2273	5881	5990
40	Thin-walled	29.5	Elastic Collapse	1782	5445	5528
45	Thin-walled	32.2	Elastic Collapse	1364	5006	5088
50	Thin-walled	35.4	Elastic Collapse	1019	4564	4622

Pitting Corrosion – Burst Case (Po = 0)

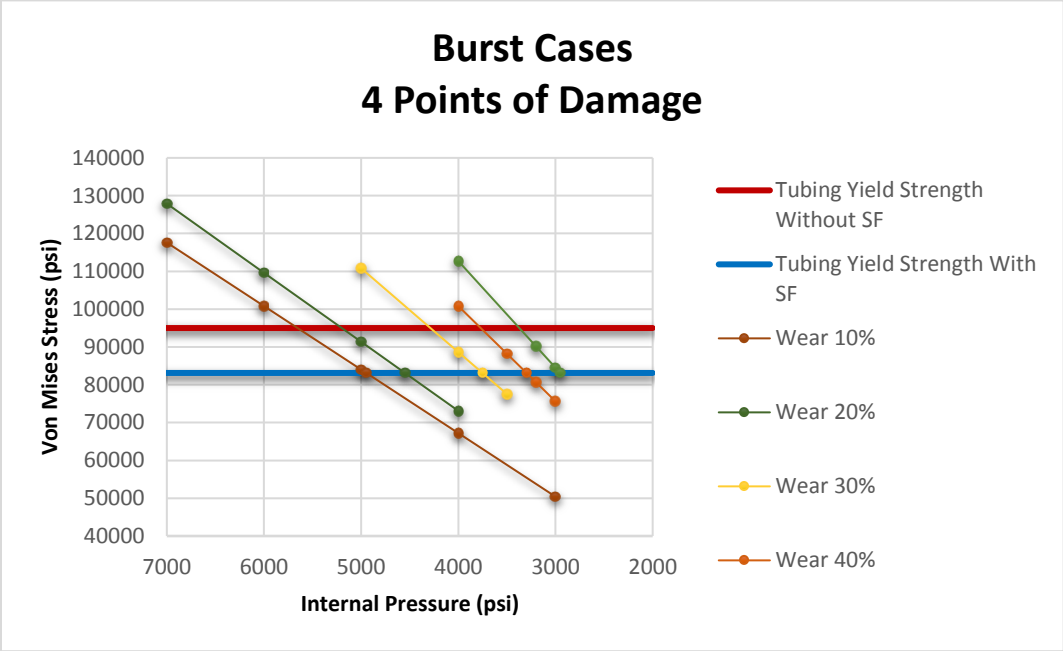

Figure C4: Collapse pressure limits for 10-50% wear – 4 points of damage

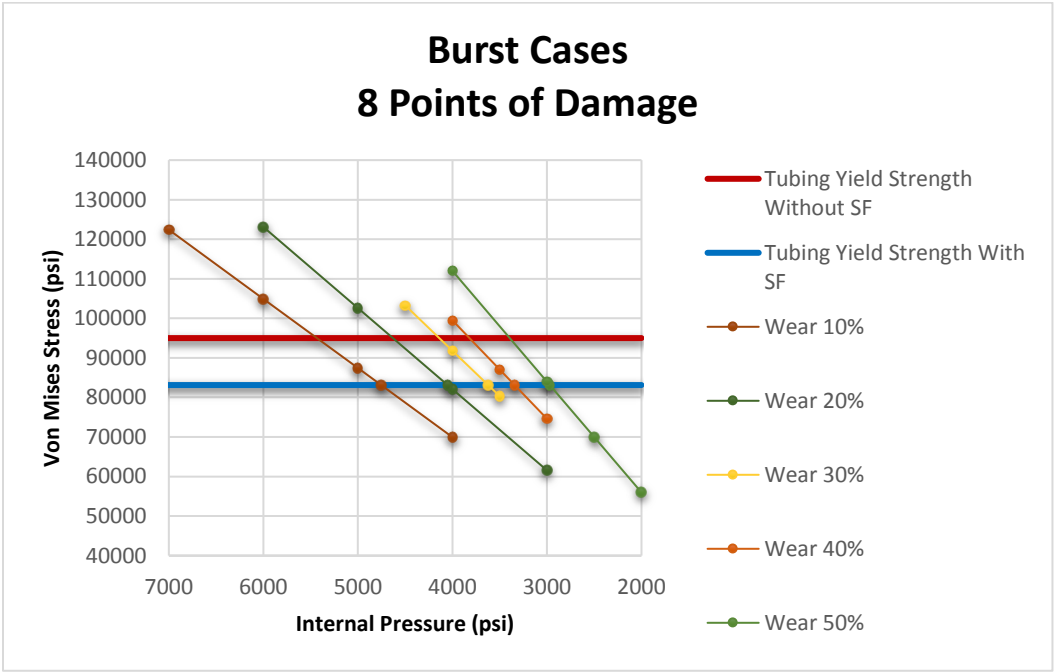

Figure C5: Collapse pressure limits for 10-50% wear – 8 points of damage

Table C8: Simulation vs. theoretical equations for Po = 0 – burst case

Wear (%)	Cylinder Type	Pressure from Equation (psi)		Pressure from Abaqus Simulation (psi)	
		Barlow	Tri-axial	4 Points of damage	8 Points of damage
10	Thick-walled	8454	8399	4947	4753
20	Thin-walled	7515	7476	4549	4051
30	Thin-walled	6575	6549	3752	3622
40	Thin-walled	5636	5620	3298	3342
50	Thin-walled	4697	4687	2951	2970

Pitting Corrosion – Collapse Case (Pi ≠ 0)

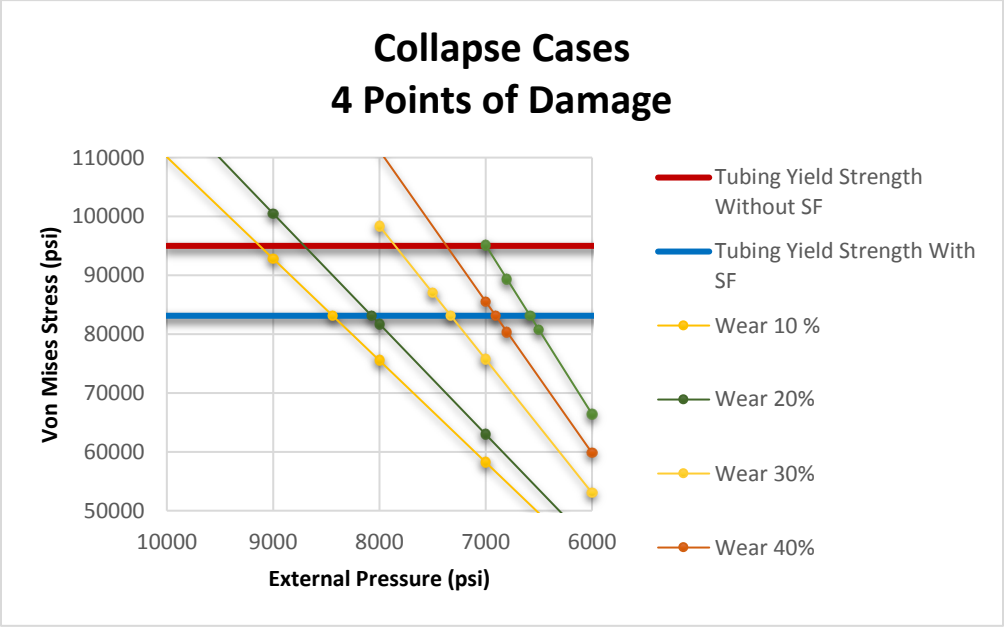

Figure C6: Collapse pressure limits for 10-50% wear – 4 points of damage

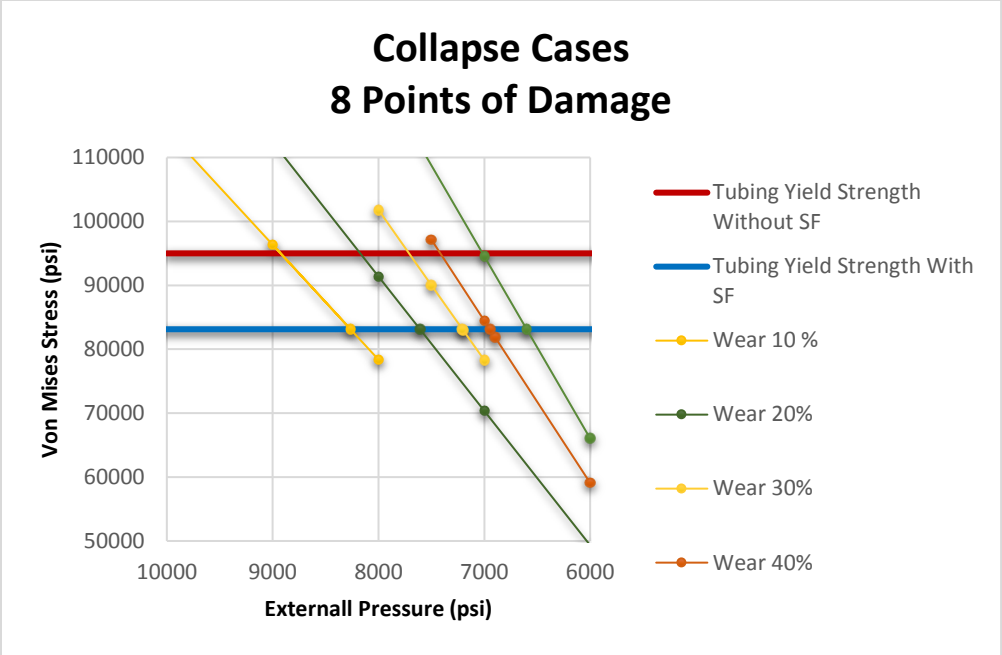

Figure C7: Collapse pressure limits for 10-50% wear – 8 points of damage

Table C9: Simulation vs. theoretical results for Pi ≠ 0 – collapse case

Wear (%)	Cylinder Type	Collapse Equation	D/t	Collapse Pressure from Equation (psi)		Pressure from Abaqus Simulation (psi)	
				Po API	Tri-axial	4 points of damage	8 points of damage
10	Thick-walled	Plastic Collapse	19,7	6057	9985	8440	8263
20	Thin-walled	Transitional Collapse	22,1	5164	9146	8074	7607
30	Thin-walled	Transitional Collapse	25,3	4321	8298	7328	7206
40	Thin-walled	Elastic Collapse	29,5	3704	7438	6906	6947
50	Thin-walled	Elastic Collapse	35,4	2965	6568	6582	6600

Pitting Corrosion – Collapse Case (Pi = 0)

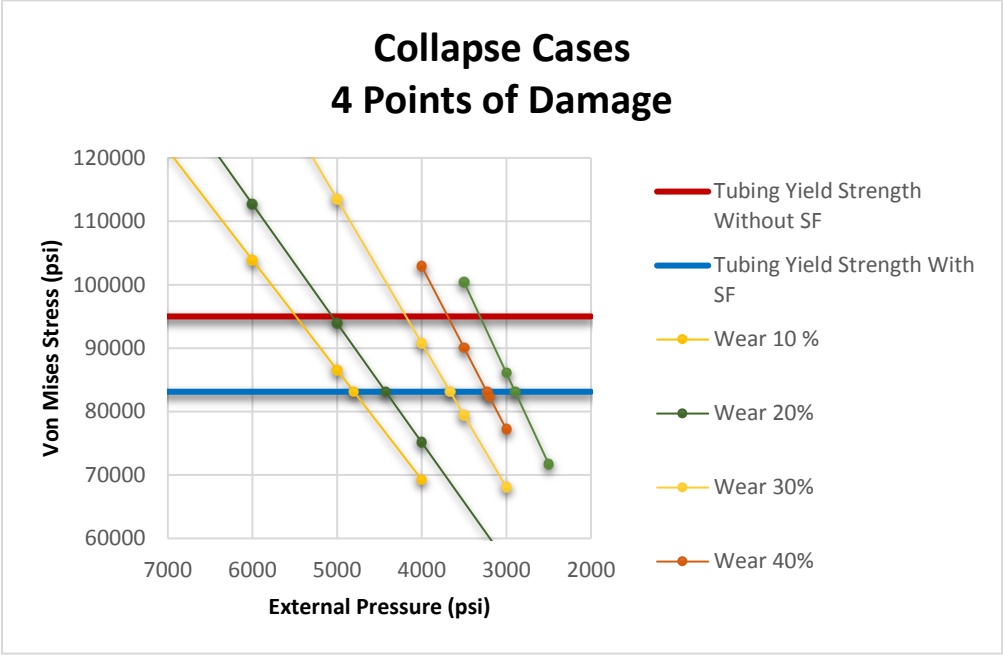

Figure C8: Collapse pressure limits for 10-50% wear – 4 points of damage

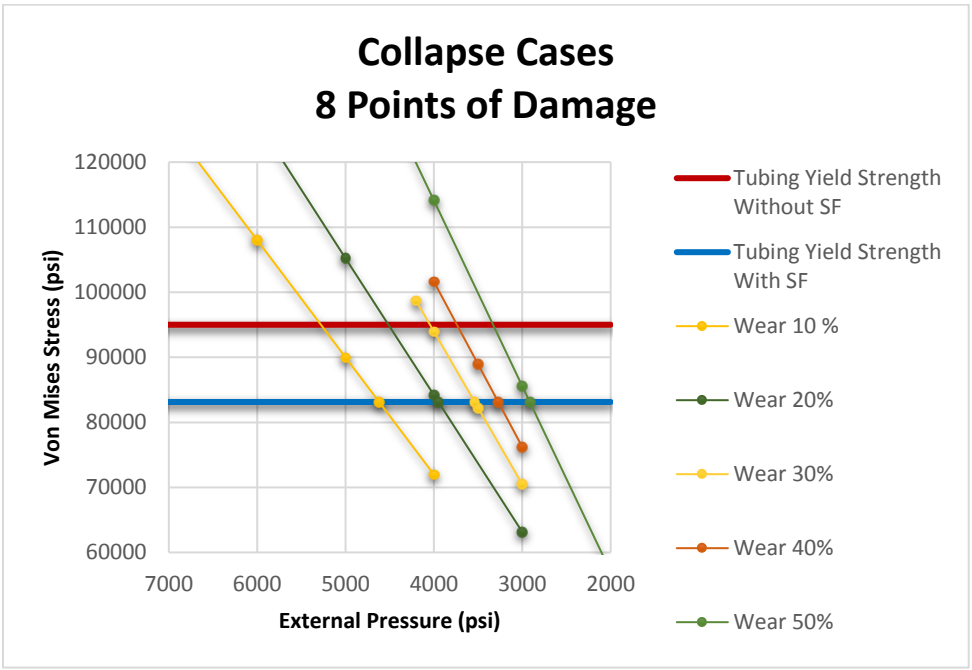

Figure C9: Collapse pressure limits for 10-50% wear – 4 points of damage

Table C10: Simulation vs. theoretical results for Pi = 0 – collapse case

Wear (%)	Remarks	Collapse Equation	D/t	Collapse Pressure from Equation (psi)		Pressure from Abaqus Simulation (psi)	
				Po API	Tri-axial	4 points of damage	8 points of damage
10	Thick-walled	Plastic Collapse	20	4204	8024	4801	4620
20	Thin-walled	Transitional Collapse	22,1	3288	7175	4425	3949
30	Thin-walled	Transitional Collapse	25,3	2422	6315	3663	3539
40	Thin-walled	Elastic Collapse	29,5	1782	5445	3231	3272
50	Thin-walled	Elastic Collapse	35,4	1019	4564	2897	2915

Appendix D - FEM Simulation Results (Visualization)

Uniform Corrosion Cases (Unworn Tubing)

Case 1 – Burst (Po ≠ 0)

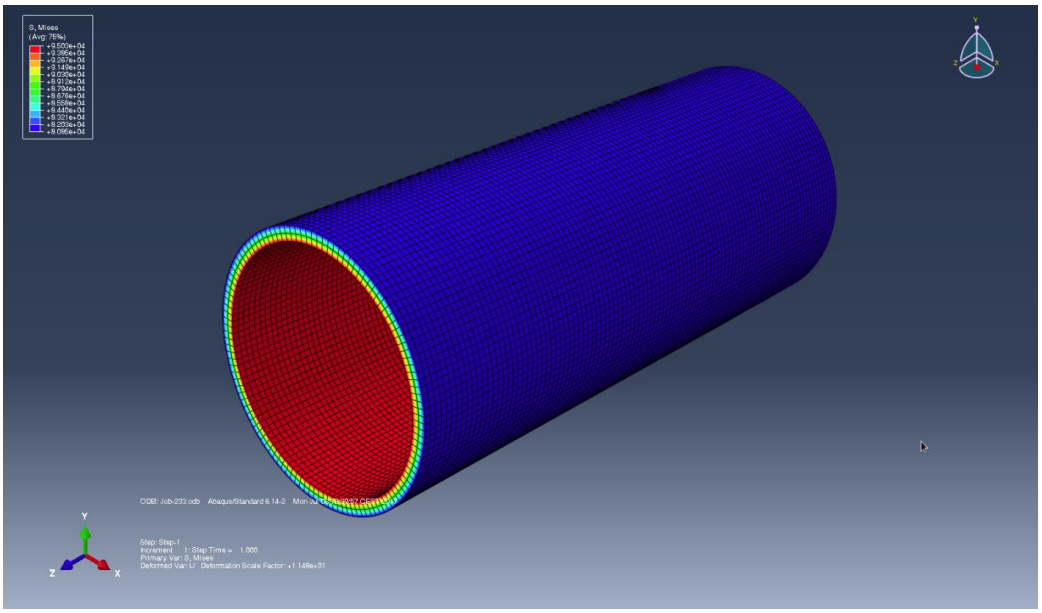

Figure D1: Stress distribution in unworn tubing for burst case (Po ≠ 0) – uniform corrosion

Case 1 – Burst (Po = 0)

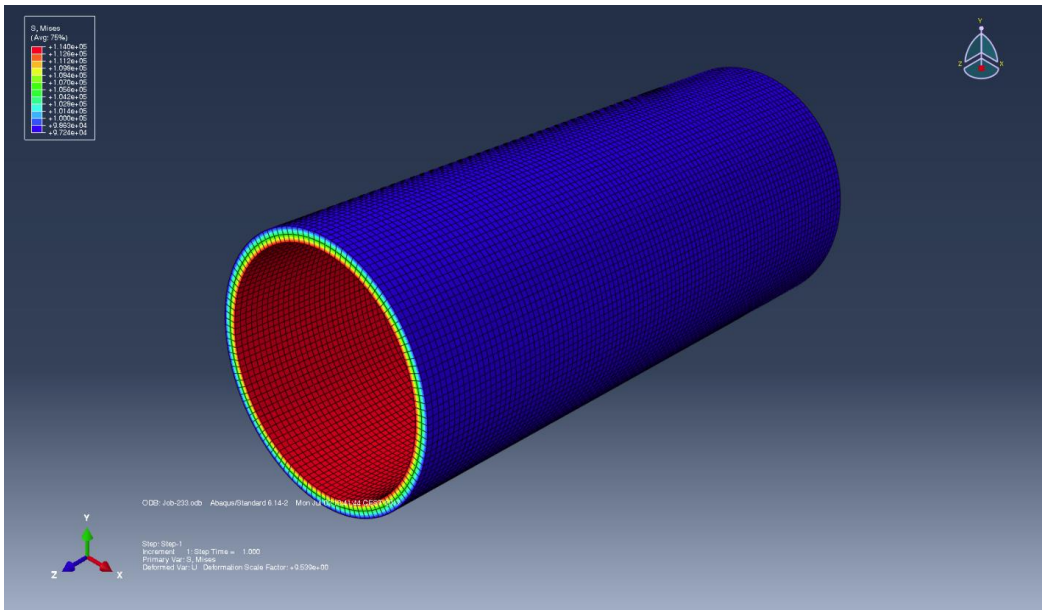

Figure D2: Stress distribution in unworn tubing for burst case (Po = 0) – uniform corrosion

Case 2 – Collapse (Pi ≠ 0)

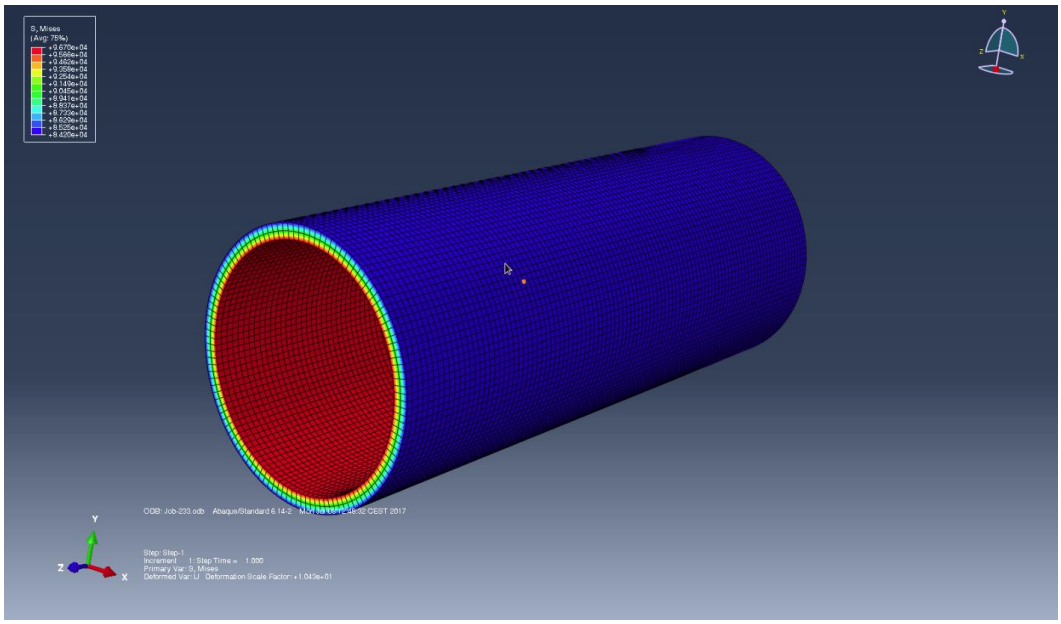

Figure D3: Stress distribution in unworn tubing for collapse case (Pi ≠ 0) – uniform corrosion

Case 2 – Collapse (Pi = 0)

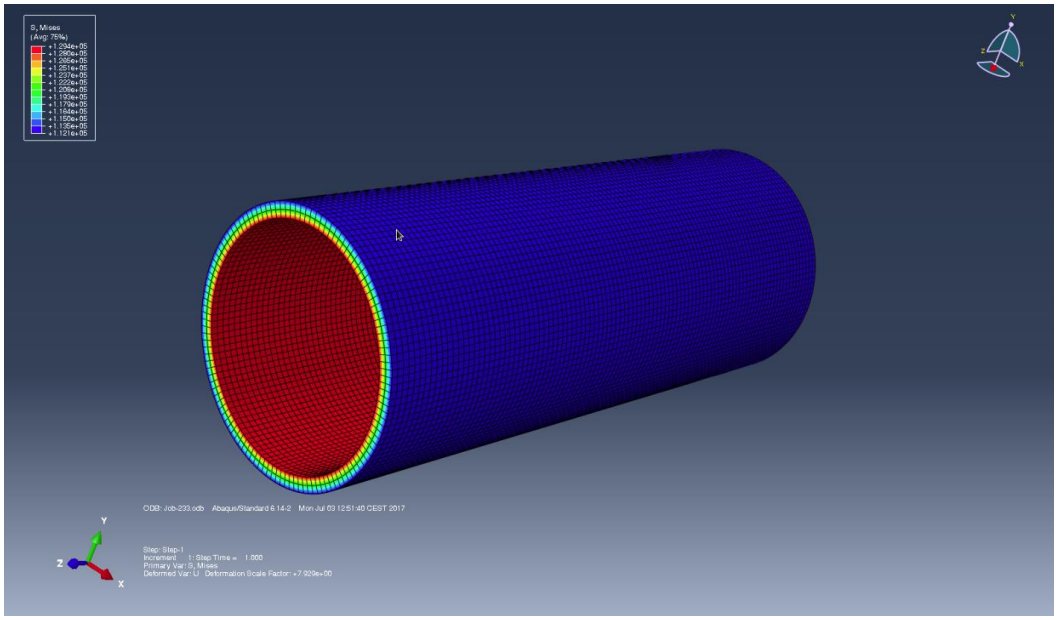

Figure D4: Stress distribution in unworn tubing for collapse case (Pi = 0) – uniform corrosion

Uniform Corrosion Cases (Tubing with 30% Wear depth)

Case 1 – Burst (Po ≠ 0)

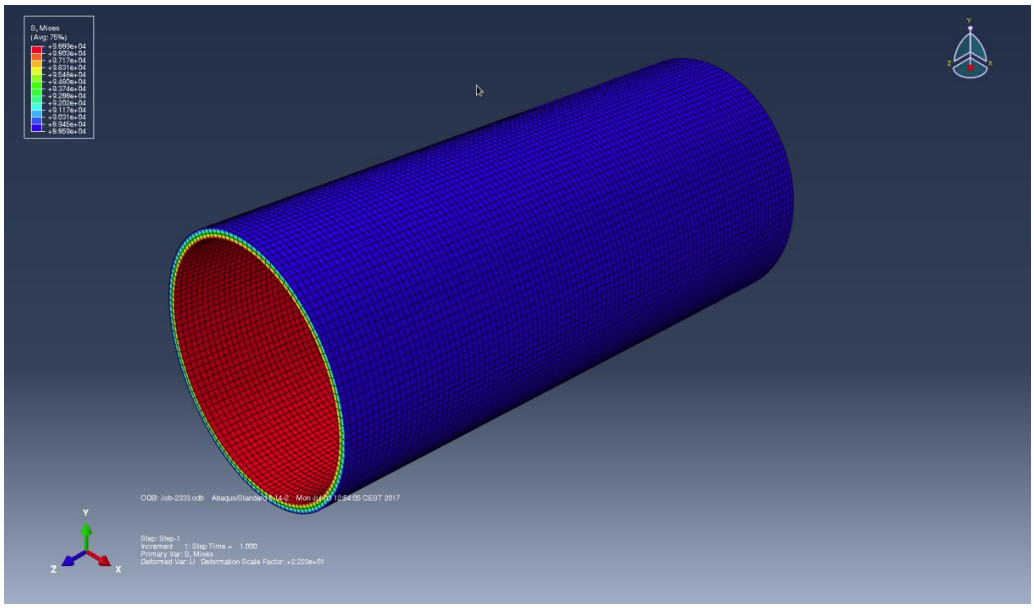

Figure D5: Stress distribution in tubing with 30% wear depth for burst case (Po ≠ 0) – uniform corrosion

Case 1 – Burst (Po = 0)

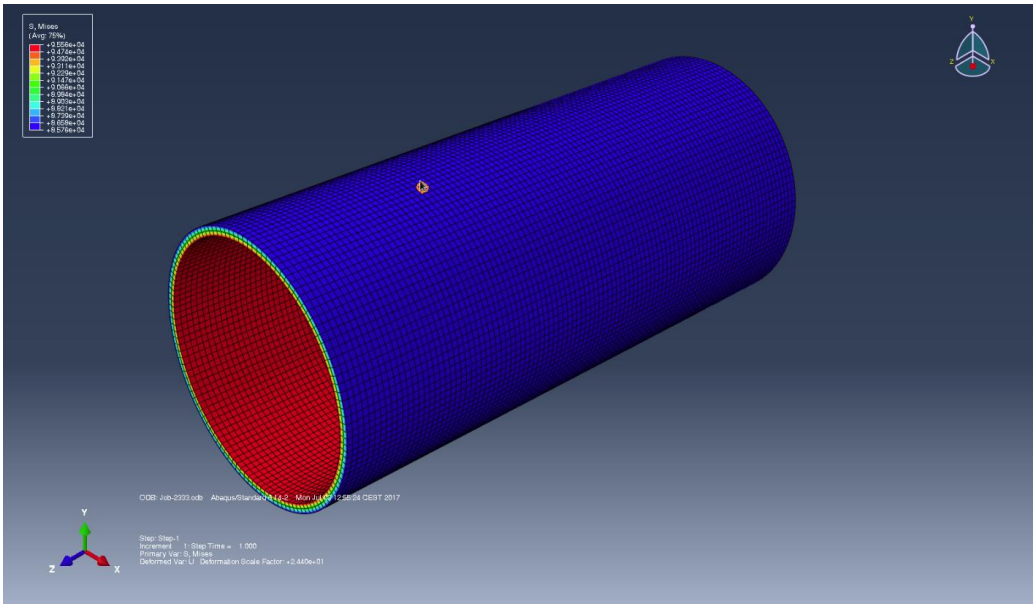

Figure D6: Stress distribution in tubing with 30% wear depth for burst case (Po = 0) – uniform corrosion

Case 2 – Collapse (Pi ≠ 0)

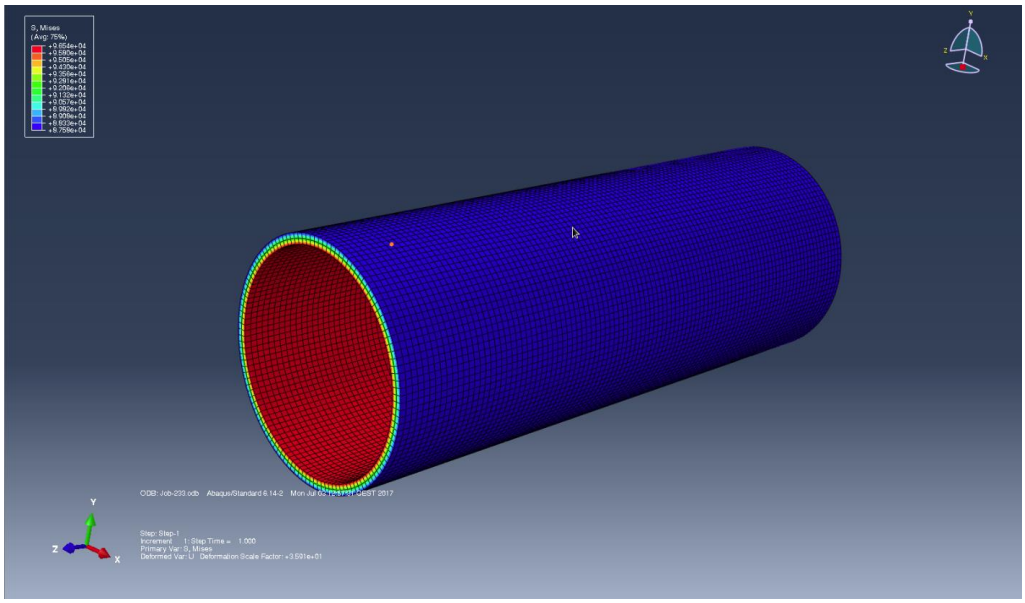

Figure D7: Stress distribution in tubing with 30% wear depth for collapse case (Pi ≠ 0) – uniform corrosion

Case 2 – Collapse (Pi = 0)

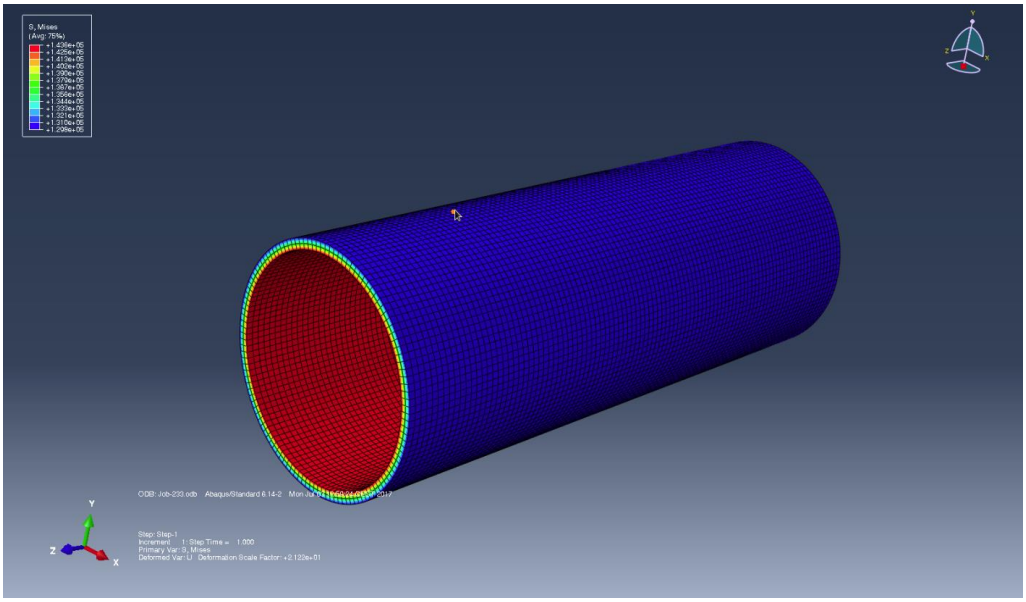

Figure D8: Stress distribution in tubing with 30% wear depth for collapse case (Pi = 0) – uniform corrosion

Pitting Corrosion Cases – 4 Points of Damage (Tubing with 30% Wear Depth)

Case 1 – Burst (Po ≠ 0)

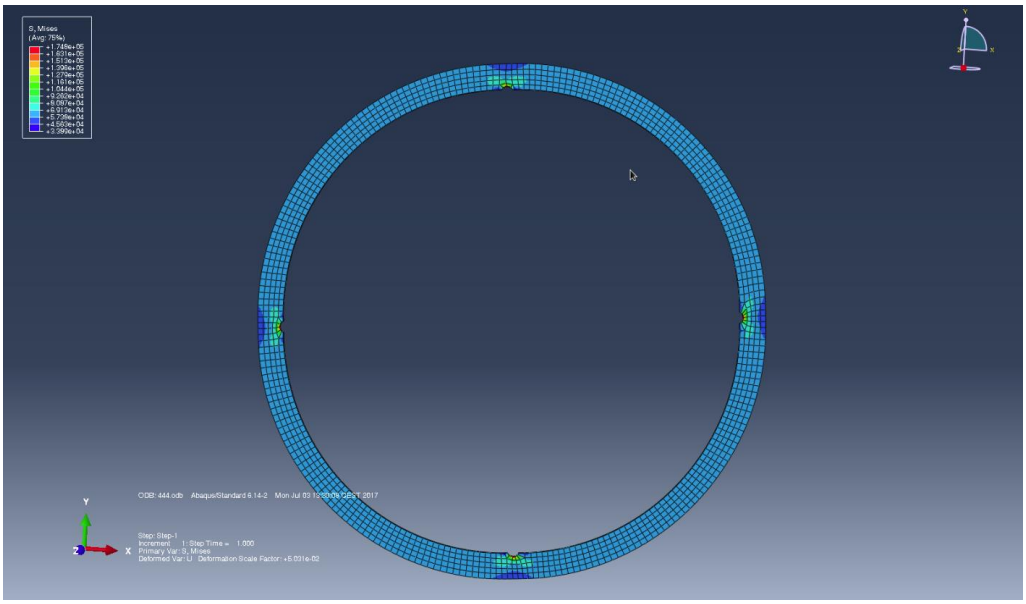

Figure D9: Stress distribution in unworn tubing for burst case (Po ≠ 0) – pitting corrosion with 4 points of damage

Case 1 – Burst (Po = 0)

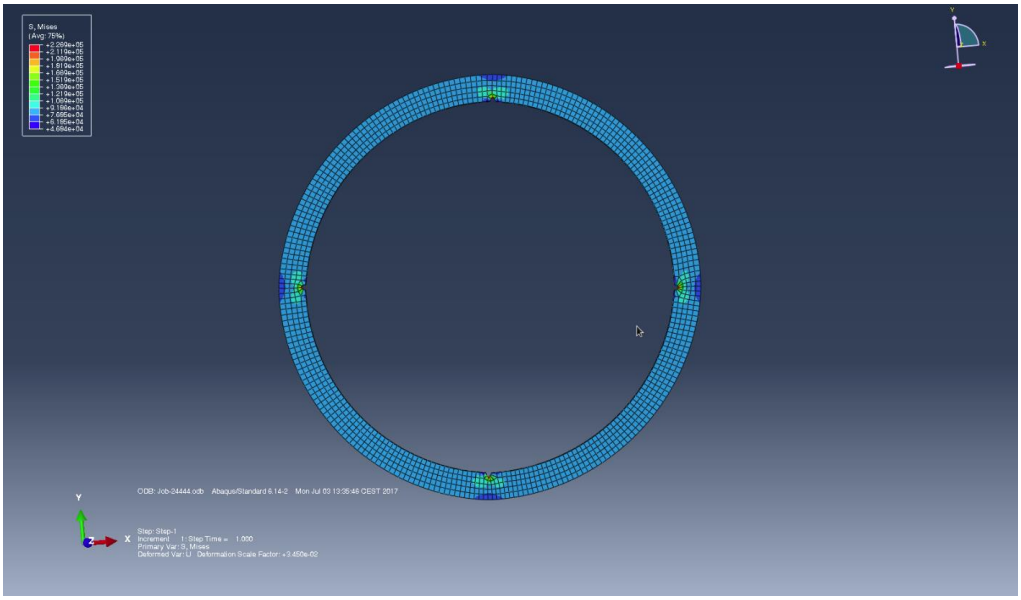

Figure D10: Stress distribution in unworn tubing for burst case (Po = 0) – pitting corrosion with 4 points of damage

Case 2 – Collapse (Pi ≠ 0)

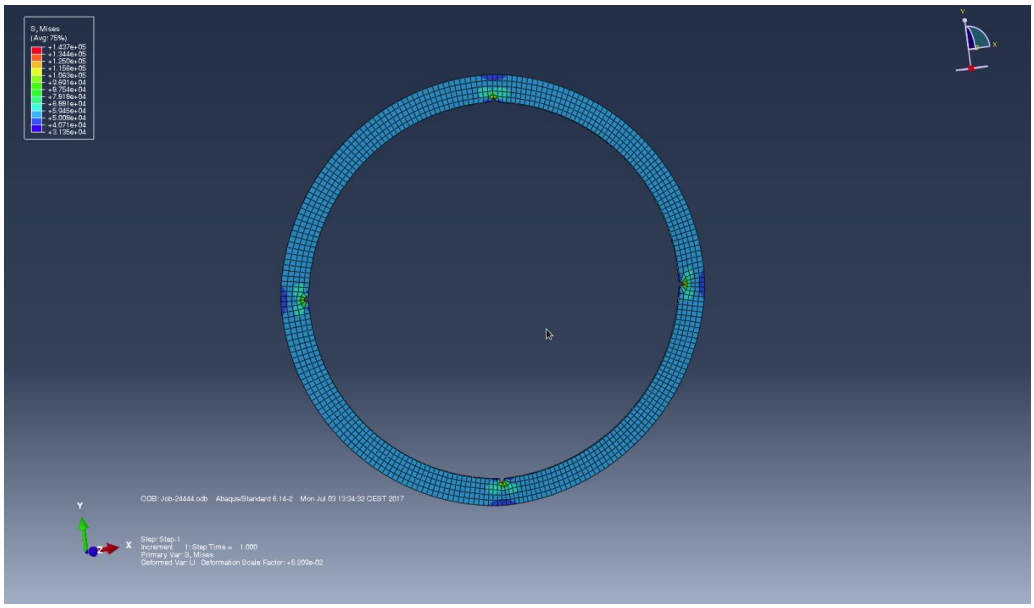

Figure D11: Stress distribution in unworn tubing for collapse case (Pi ≠ 0) – pitting corrosion with 4 points of damage

Case 2 – Collapse (Pi = 0)

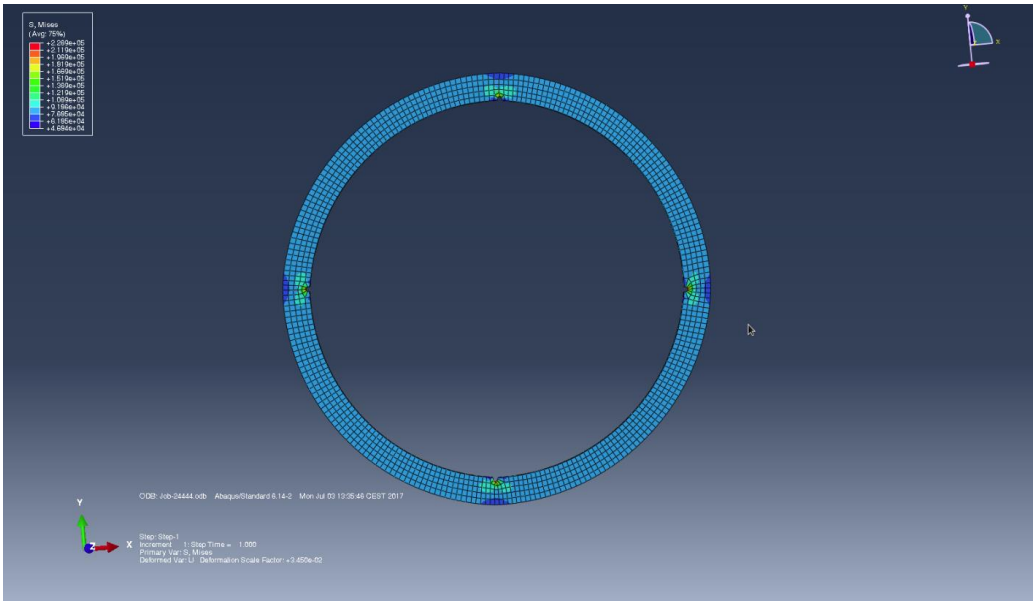

Figure D12: Stress distribution in unworn tubing for collapse case (Pi = 0) – pitting corrosion with 4 points of damage

Pitting Corrosion Cases – 8 Points of Damage (Tubing with 30% Wear Depth)

Case 1 – Burst (Po ≠ 0)

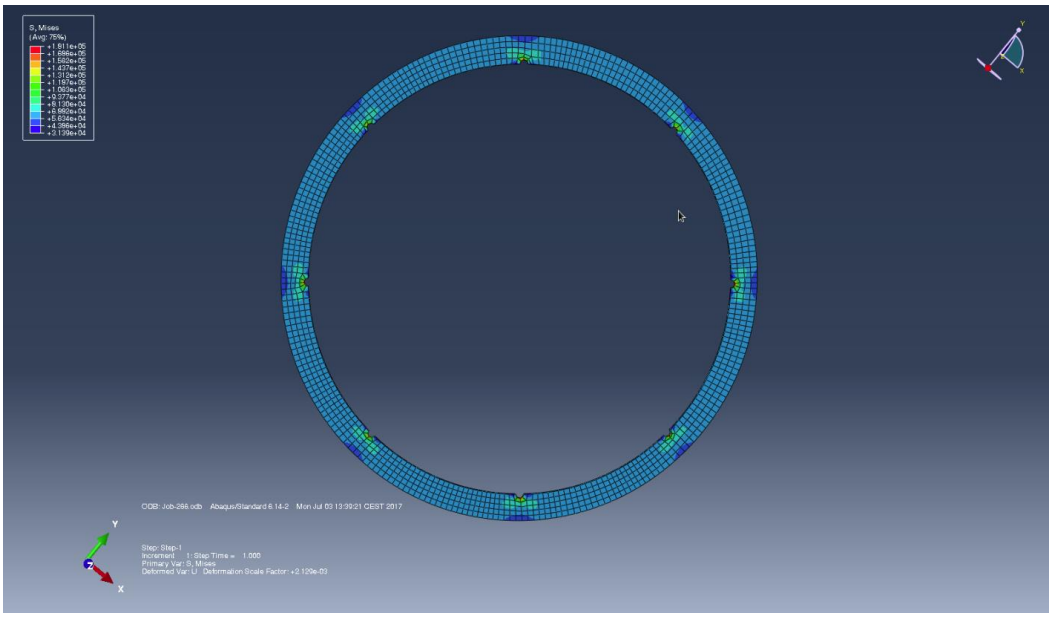

Figure D13: Stress distribution in tubing with 30% wear depth for burst case (Po ≠ 0) – pitting corrosion with 8 points of damage

Case 1 – Burst (Po = 0)

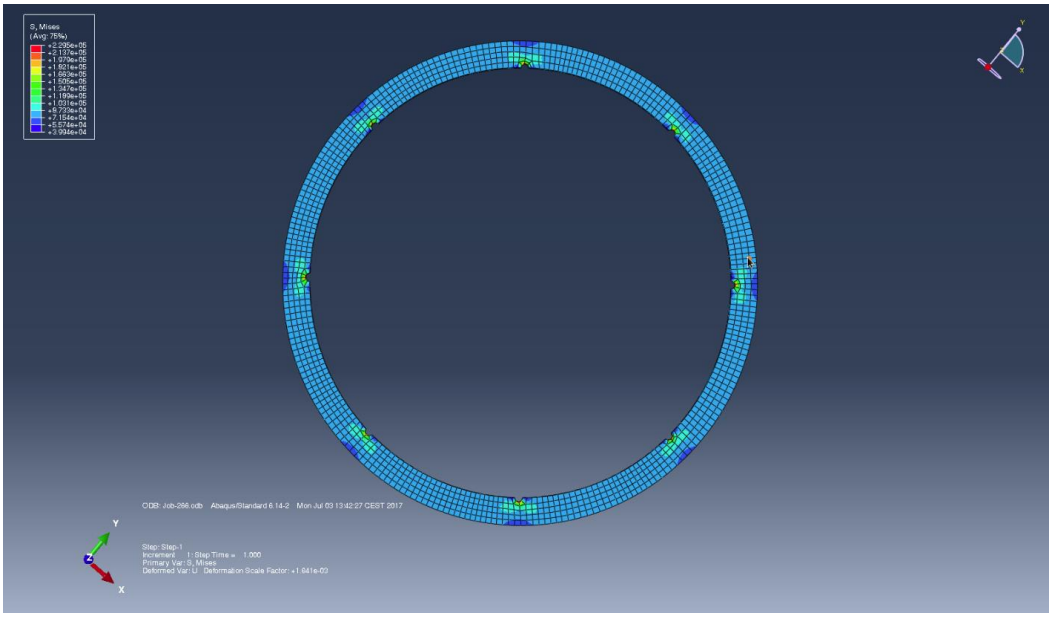

Figure D14: Stress distribution in tubing with 30% wear depth for burst case (Po = 0) – pitting corrosion with 8 points of damage

Case 2 – Collapse (Pi ≠ 0)

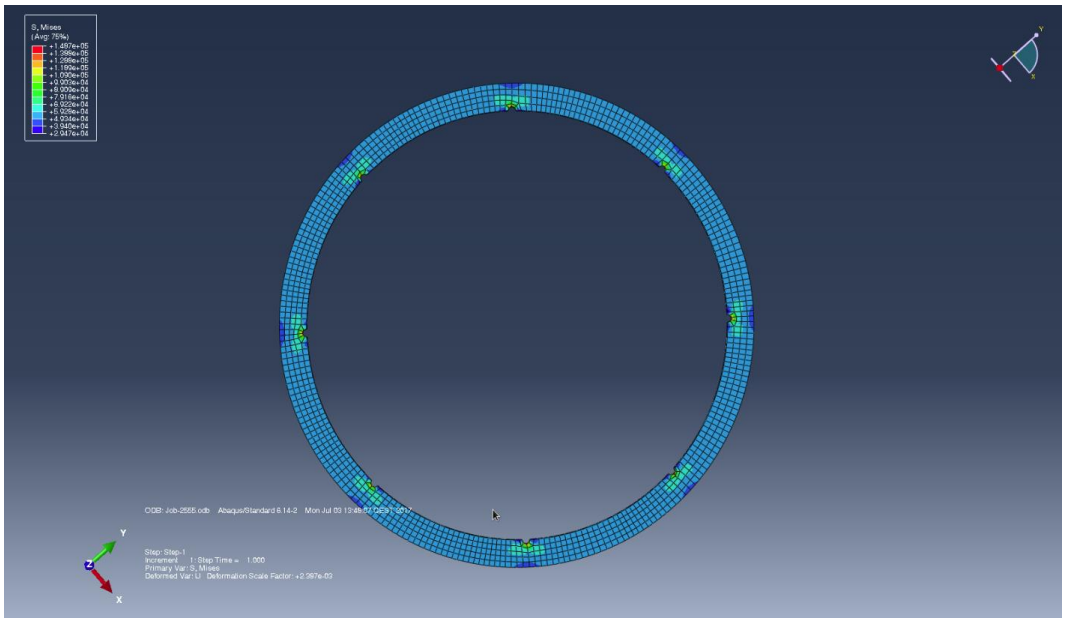

Figure D15: Stress distribution in tubing with 30% wear depth for collapse case (Pi ≠ 0) – pitting corrosion with 8 points of damage

Case 2 – Collapse (Pi = 0)

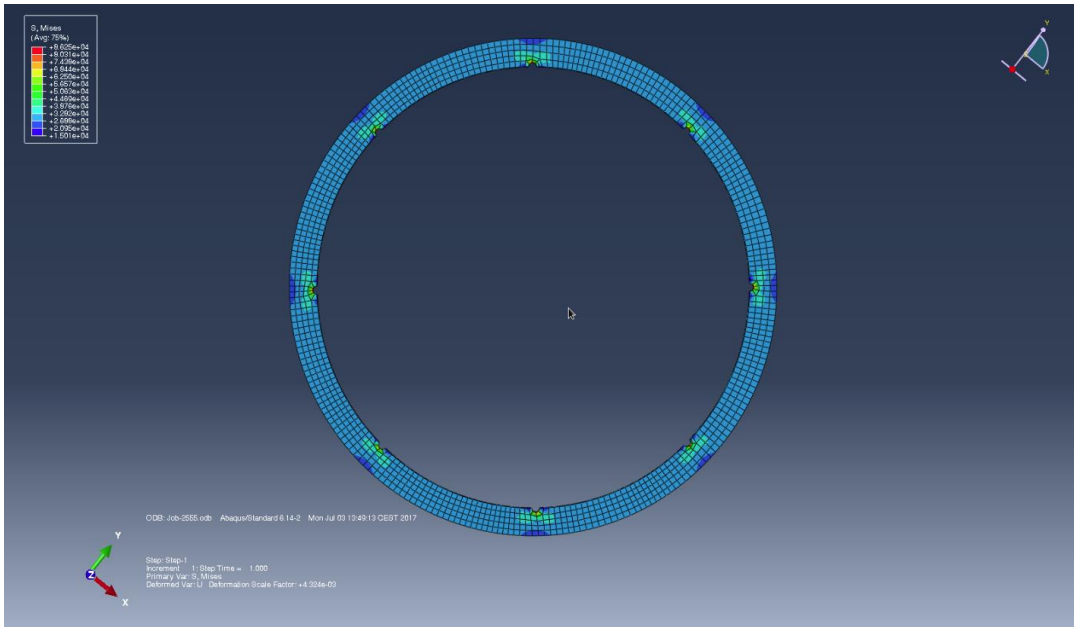

Figure D16: Stress distribution in tubing with 30% wear depth for collapse case (Pi = 0) – pitting corrosion with 8 points of damage